Vortices and solitons in microcavity exciton-polaritons

Hartley, Robin

Award date:
2012

Awarding institution:
University of Bath

Vortices and Solitons in Microcavity Exciton-Polaritons

submitted by

R.G.S. Hartley

for the degree of Doctor of Philosophy

of the

University of Bath

Department of Physics

February 24, 2012

Abstract

In this work, we discuss the stability of roll solutions for exciton-polariton condensates in wide aperture semiconductor microcavities operated in the strong coupling regime when pumped with a coherent beam. From which, we progress to study the behavior of vortices and solitons on a Gaussian background. Individually, all vortices with winding number $|m| > 1$ are found to be unstable and decay into the appropriate number of stable $m = 1$ vortices.

Using these stable vortices, we propose new classes of vortex lattices that are supported through the parametric conversion of polaritons. Both the honeycomb and square lattices are determined to be robust in practically relevant settings, for an appropriate angle of the probe beam, seeding in the signal region of momentum space. For other angles, we discuss the two possible melting scenarios.

Through the introduction of polarization into the system, it is seen that multiple bistability regions exist. By extending the study of honeycomb lattices to include these effects, we show that stable lattices can only exist for a circular or linearly polarized pump and probe. In the linearly polarized system, vector solitons are observed, where the existence of stable vector solitons, in one dimension and two dimensions, is demonstrated along all three branches. Under an elliptically polarized pump, it is seen that only the first of the two bistability regimes hosts a family of stable vector dark bright solitons, whilst the second higher energy branch is generally unstable.

In two dimensions, we observe that perpendicular to the pump axis, all forms of vector solitons will either contract or expand dependent upon the pump intensity, mirroring the dynamics of scalar solitons. Finally, we discuss the potential for coherent control of these solitons is then demonstrated the switching of the polarization state.

Acknowledgments

I would like to thank my supervisor, Dmitry for his guidance during my time in Bath, and Andrey for answering whatever questions I had.

Contents

CHAPTER 1

Introduction

At its heart, this body of work is concerned with the question of superfluidity in out of equilibrium polariton condensates, as arising through nonlinear interparticle interactions.

Superfluidity was first discovered in 1939 by Kapitsa *et al.* , with the earliest theory being developed in the 1940*s* by Landau[97]. As a phase of matter, it has a number of distinctive properties; in particular, it exhibits fluid flow without friction. This effect is especially visible when the fluid is in a rotating frame, where it is observed that the development of a rotating state, that consists of quantized vortices, occurs once the rotation is above a certain critical velocity. At low temperatures in ^4He[125] and in a number of interacting atomic Bose-Einstein condensates, superfluidity can be identified through a number of criteria[82]. These criteria are

- Local thermal equilibrium
- A Landau critical velocity
- Quantized vortices
- Solitary waves
- Two-fluid hydrodynamics
- Metastable persistent flow

Polariton condensates do not exist in equilibrium, yet d'Alembert's paradox, wherein the absence of drag is observed on a moving object has been realized experimentally by Amo *et al.* [6], but above a critical velocity, drag does not emerge from the shedding of vortices. As a result of this, the first two criteria are not satisfied for polaritons. Quantized vortices and solitons, however have been observed experimentally by Keeling *et al.* [81] and Adrados *et al.* amongst others[2, 161]. The behavior of these solitons and vortices is the main focus of this document.

These features emerge through nonlinear effects in the media that emerge through interparticle interactions in the microcavity. These interactions work to balance dispersive contributions and thereby allow for the existence of these features[128]. The strength of these interactions serves to produce a greater localization and a picosecond excitation time, which may provide significant benefits for information processing, particularly in the creation of individual optical switches or low power memory elements.

1.1 Semiconductor Microcavities

Microcavity are typically a few micrometers thick and are formed from an optical medium, bounded by a pair reflecting faces[190]. They originated in 1992, when the work of Weisbuch and associates [194, 39] lead to the realization of the first device capable of displaying a vacuum Rabi splitting. Since then, the microcavity has been highly significant in the study of exciton physics within semiconductors, as they allow for control of the properties of both the photonic and excitonic components. These properties have simulated a number of important studies into bleaching of the strong coupling[67], control of excitons and polaritons through external fields[50] and motional narrowing of the exciton spectrum[201] among numerous other results.

Microcavities can consist of a *Fabry-Pérot* cavity with an optical length that is equal to a half-integer multiple of the embedded photon wavelength, as illustrated in figure 1-1. In practice distributed Bragg Reflectors, typically replace the mirrors enclosing the quantum well which are formed from multiple layers of varying refractive index to produce a higher quality reflector. Within such cavities, photons are quantized along the direction of growth, while the in-plane directions are not. For excitons, one has an identical quantization, and since each in-plane exciton couples only to a single photon, quasi-stationary states ex-

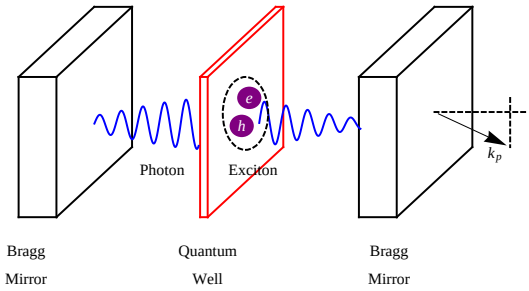

Figure 1-1: *Schematic of a Fabry-Pérot cavity.*

ist where the system oscillates between a pure photonic and pure excitonic state with a period in the subpicosecond range. The doping of the distributed Bragg reflectors with p and n materials allow an electric field to exist across the cavity. This lowers the exciton transition energy through the confined quantum stark effect[52], wherein the fields reduce the energy of the bound states and leads to modulation of the effective bandgap and a reduction in the recombination efficiency, which allows a tuning of the exciton resonance through the cavity mode. These transitions between levels gives rise to a spectral line in the electromagnetic emission spectrum. When at rest, this line will possess a non-zero decay width/linewidth as a consequence of the uncertainty principle, which is known as the natural linewidth.

1.1.1 Cavity Linewidth

For real mirrors, photons do not remain trapped within such a cavity indefinitely, and thus there is decrease in the lifetime of the photon and a corresponding increase in the linewidth from its natural value. In order to discuss this property, we initially examine the field profile of a cavity that has perfectly reflecting mirrors to discuss one of the characteristics of a microcavity. It is well known that the resonance condition requires that the phase change over a round trip is equal to $2\pi N$ where

$$\sqrt{\frac{\omega^2}{c^2}\eta_c^2 - k_{||}^2}L_c = k_z L_c = N\pi \tag{1.1}$$

where ω is the photon frequency, N is an integer, while L_c and η_c are the cavity length and refractive index respectively. The component of the wave-vector along

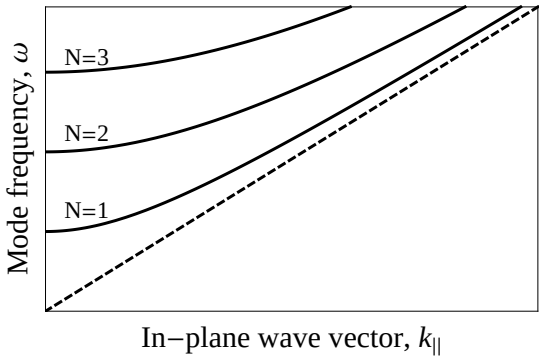

Figure 1-2: *The dispersion curves of a Fabry-Pérot resonator, where the modes, N = 1,2,3 are shown by the solid lines as determined through equation 1.1, whilst the dashed line corresponds to the free photon dispersion, $\omega = ck_{||}/\eta_c$.*

the growth direction, k_z is quantized as mentioned previously, while $k_{||}$ is a free quantum number due to the in-plane symmetry of the structure, which is plotted within figure 1-2. Through this relation, it is evident that no electromagnetic fields exist in the cavity below a minimum frequency.

When one considers the use of imperfect mirrors possessing a finite reflectivity $R = |r(\omega)|^2$, it is immediately evident that the E-field will be a superposition of two plane waves of the form

$$\begin{aligned} E(\omega, z) &= E_0 \left(I(\omega) e^{ik_z z} + J(\omega) e^{-ik_z z} \right) \\ I(\omega) &= \frac{\sqrt{1-r^2}}{1 - r^2 e^{ik_z L_c}} \\ J(\omega) &= r I(\omega) e^{ik_z L_c} \end{aligned} \tag{1.2}$$

and through this, it is readily observed that the field strength at the center of the cavity is given by

$$|E(\omega)|^2 = E_0^2 \frac{1-r^2}{(1-r^2) + 4r \sin^2(k_z L_c)} \tag{1.3}$$

performing a second order Taylor expansion yields $|E(\omega)|^2 \propto 1/((\omega - \omega_c)^2 + \gamma_c^2)$, where the cavity resonance frequency is $\omega_c = \pi c/\eta_c L_c$ and the linewidth for a Fabry-Pérot cavity is

$$\gamma_c = \frac{1-r}{2r}\frac{c}{\eta_c L_c} = \frac{1-r}{2r}\pi\omega_c \tag{1.4}$$

Microcavities are essentially a Fabry-Pérot cavity with an unusual mirror where this description requires that the reflectivity is approximately constant for Bragg reflectors possessing a large number of layers, N. The reflectivity is given through

$$R = |r(\omega)|^2 = 1 - 4\frac{\eta_{ext}}{\eta_c}\left(\frac{\eta_1}{\eta_2}\right)^{2N} \tag{1.5}$$

for η_1, η_2 are the refractive indices for the two materials used for the Bragg reflectors, where $\eta_1 > \eta_2$ and the phase dependency that is approximately linear

$$\Phi_r(\omega) = \frac{\eta_c L_{DBR}}{c}(\omega - \omega_m) \tag{1.6}$$

for a stop band centered on ω_m, and a penetration depth L_{DBR} as given by

$$L_{DBR} = \frac{\lambda}{2}\frac{\eta_1\eta_2}{\eta_c\,(\eta_1 - \eta_2)} \tag{1.7}$$

where λ is a wavelength and each layer of the distributed Bragg reflector has a thickness of $\lambda/4$.

For distributed Bragg reflectors, equation 1.3 remains valid under the replacement $r \to r(\omega)$ where the field intensity is given by

$$|E(\omega)|^2 = E_0^2\frac{1-|r(\omega)|^2}{(1-|r(\omega)|^2) + 4|r(\omega)|\sin^2(k_z L_c + \phi_r(\omega)/2)} \tag{1.8}$$

and the microcavity mode linewidth is given by

$$\gamma_c = \frac{1-\sqrt{(R)}}{2\sqrt{R}}\frac{c}{\eta_c\,(L_c + L_{DBR})} \tag{1.9}$$

From this one defines a cavity finesse

$$F = \frac{\pi\sqrt{R}}{1-\sqrt{R}} \tag{1.10}$$

as the ratio of the mode separation to the mode linewidth, where cavities typically possess a finesse that is comparable to that associated with metallic cavities [175]. The ability of the cavity to confine the field can be described by a quality factor, Q which is defined as the ratio of the resonance wavelength to the full-width half

maximum. This is related to the cavity finesse through

$$Q = \frac{n_{eff} L_{cav}}{\lambda} F \tag{1.11}$$

where n_{eff} is the effective refractive index and L_{cav} is the cavity length.

1.2 Excitons

The earliest models of semiconductors relied on free Bloch electrons to determine the absorption edge of semiconductor and insulators. This model assumes that valence electrons are completely detached from ions to form a free electron gas with a modification to the electron mass based on band structure calculations[13]. This model was reasonably successful at explaining numerous experimental phenomena, particularly the temperature dependence of heat capacity and electrical conductivities, it was less successful at providing a detailed description since it does not explicitly takes the crystal lattice into account. The translational invariance of the structure requires that excited species preserves the crystal symmetry, and thus Frenkel, Peierls and Wannier developed the concept of the exciton.

When an electron is excited from the valence to conduction band, typically through the absorption of a photon, a hole remains within the valence band. This hole can be treated as a positive charge carrier, and may interact with the electron through a screened Coulomb interaction to form bound states that are known as *excitons*. The presence of these bound states in semiconductors can be seen to manifest through the presence of resonance peaks within the absorption, reflection and luminescence spectra, which can be associated with transitions to and from the bound states[33]. In general, the structure of the valence and conduction bands in energy-momentum space results in an effective mass $m^* = \hbar^2 \left(d^2/dk^2 E\right)^{-1}$ that varies across the bands, such that light and heavy electrons and holes exist. As a first approximation, these differences can be neglected so that one can assume a two-band structure. In the effective mass approximation, the equation for excitons[88] is

$$\left[\frac{p_e^2}{2m_e} + \frac{p_h^2}{2m_h} - \frac{e^2}{\epsilon r} + E_G\right] \Phi(r_e,r_h) = E\Phi(r_e,r_h) \tag{1.12}$$

where ϵ is the static dielectric screening function, r is the electron-hole separation, E_G denotes the energy gap between the top of the valence band and the minimum of the conduction band. When the dielectric constant is small and the Coulomb

interaction is large, these bound states are known as Frenkel excitons that are typically the size of a unit cell, with a binding energy of $1eV$. For large dielectric constants, it is evident that the Coulomb interaction is greatly reduced, and the lattice potential can be incorporated into the smaller effective mass of the Wannier-Mott exciton. The binding energies for which are typically an order of magnitude smaller than for Frenkel excitons, and thus Wannier-Mott excitons exist over a larger region of space. From this equation, it is seen that excitons have discrete energy levels of the form

$$E_n = -\frac{\mu e^4}{2\hbar^2 \epsilon^2 n^2} \tag{1.13}$$

with reduced mass, $\mu = m_e m_h/(m_e + m_h)$ and principal quantum number, n, where it is seen that a free exciton possesses a hydrogenic spectrum. In bulk semiconductors, these excitons are observed to possess an effective Bohr radius of $10nm$. Thus, the total energy can be expressed through

$$E = E_G + E_n + K = E_G + E_n + \frac{\hbar^2 q^2}{2M} \tag{1.14}$$

where K is the center of mass kinetic energy, with a momentum, q for an exciton of mass, M.

Given that both electron and holes are elementary charge carriers, excitons couple strongly to photons. This may be described through a dielectric function for the semiconductor, combined with the Maxwell equations[61, 66]. Near the resonance, the dielectric function is given by a weighted sum of harmonic oscillator response functions

$$\epsilon(\omega) = \epsilon_\infty + \frac{\omega_p^2}{\omega_0^2 - \omega^2 - i\nu\omega} \tag{1.15}$$

where ϵ_∞ is the background dielectric constant that accounts for all other transitions at $|\omega| >> |\omega_0|$, while ω_p measures the transition strength, and ν is a phenomenological damping constant with the transition located at a frequency, ω_T through which one can re-express equation 1.14 as

$$\begin{aligned} E = \hbar\omega_0 &= \hbar\omega_T + \frac{\hbar^2 q^2}{2(m_e + m_h)} \\ \hbar\omega_T &= E_n + E_G \end{aligned} \tag{1.16}$$

where q is the exciton wave-vector and $\hbar\omega_T$ is the required energy for the creation

of a motionless exciton.

Many studies have been devoted to understanding the role of excitons within a variety of optical effects, wherein it has been noted that one expects excitonic effects to manifest primarily in a regime of low temperature, low density and a low impurity content[27, 46, 79, 186].

1.3 Exciton-Polaritons

The solutions of Maxwell's equations in a bulk homogeneous medium can be expressed as a superposition of plane waves[72]. For each plane wave in the absence of external sources, one has

$$\vec{q} \times \left(\vec{q} \times \vec{E}\right) - \frac{\omega^2}{c^2}\vec{D} = 0 \tag{1.17}$$

for $\vec{D}(\vec{q},\omega) = \epsilon(\vec{q},\omega)\vec{E}(\vec{q},\omega)$. This equation may be separated into components that are parallel, $||$ and perpendicular, $\perp$ to $\vec{q}$ when the system is isotropic to obtain

$$q^2\vec{E}^{\perp} - \tfrac{\omega^2}{c^2}\vec{D}^{\perp} = 0 \quad \tfrac{\omega^2}{c^2}\vec{D}^{||} = 0 \tag{1.18}$$

In nonlocal systems, $\vec{E}^{\perp}$ may only be nonzero provided that momentum $\vec{q}$ and frequency ω are related through the transverse dispersion relation

$$q^2 = \frac{\omega^2}{c^2}\epsilon(\vec{q},\omega) \tag{1.19}$$

whilst for the longitudinal field, one has

$$\epsilon(\vec{q},\omega) = 0 \tag{1.20}$$

for a non-vanishing solution. It is noted that the system's response depends upon the orientation of the field and wave-vector. Now, substituting equation 1.15 into the relations 1.19 and 1.20 demonstrates that two transverse modes exist for each frequency where

$$q^2 = \frac{1}{2}\left(\Gamma_0^2 + \epsilon_\infty\frac{\omega^2}{c^2}\right) \pm \frac{1}{2}\left[\left(\Gamma_0^2 - \epsilon_\infty\frac{\omega^2}{c^2}\right)^2 + \frac{4\omega^2\omega_p^2}{Dc^2}\right]^{1/2} \tag{1.21}$$

with

$$\Gamma_0^2 = \frac{\omega^2 + i\nu\omega - \omega_T^2}{D} \quad D = \frac{\hbar\omega_T}{m_e + m_h}$$

In contrast, there exists only a single longitudinal mode

$$q^2 = \Gamma_0^2 - \frac{\omega_p^2}{D\epsilon_\infty} \tag{1.22}$$

These relations yield solutions that resemble excitons for large wave vectors and electromagnetic waves in a local system otherwise. These modes consisting of excitons strongly coupled to photons are known as exciton-polaritons. These modes can exist in both bulk semiconductor and microcavities.

If one neglects the effects of disorder on the system, only photonic states possessing the same in-plane wave vector can couple to a chosen excitonic state[32, 33]. It is these coupled eigenstates that are referred to as *cavity polaritons*[10, 14, 65, 74, 93].

1.3.1 Microcavity Polaritons

These polaritons are known as quasi-particles, but they are not fundamentally different from other elementary particles, and correspondingly they can be treated as heavy photons with stronger interactions[36, 169].

There is a splitting between coupled modes of the cavity that is known as the Rabi splitting. When this is very much greater than either the cavity or exciton linewidths, the system is said to be the strong coupling regime[75, 39, 164], which can be expressed through the condition

$$\Omega_R > \frac{1}{2}|\gamma_e - \gamma_{ph}| \tag{1.23}$$

for exciton, γ_e and photon γ_{ph} damping terms, while the system is said to be in the *weak coupling regime* otherwise. Typically, this Rabi splitting is of the order of $5meV$ in inorganic microcavities[34, 39], so is observable at low temperatures. It is noted that organic or nanoscale microcavities[103, 191, 207] have significantly higher vacuum Rabi splittings of the order of $300meV$, so may allow observation of polaritons at room temperatures.

This coupling between excitons and photons can only occur between states possessing the same in-plane wave vector[11]. As the wave-vectors are quantized, it is evident that spatial dispersion along the growth axis is eliminated, thereby

allowing measurements of the dispersion curves to be obtained through reflectivity and luminescence experiments.

The photonic component of the polariton only remains coupled to the exciton for a limited time. This rate of spontaneous emission of these photons is dependent on the environment. This is known as the Purcell effect[130] where the enhancement factor is given through

$$F_P = \frac{3}{4\pi^2}\left(\frac{\lambda}{n}\right)^3\left(\frac{Q}{V}\right) \tag{1.24}$$

where (λ/n) is the wavelength inside the material, V is the cavity mode volume and Q is the quality factor. As a result, it is possible for a direct conversion to external photons to occur. These photons are confined between the Bragg mirrors within the microcavity and thus the photons acquire an effective mass, $m_{ph} \approx \hbar\widetilde{n}_c/cL_c$ where $\widetilde{n}_c$ is the effective refractive index of the cavity, determined through an averaging of the indexes of the cavity and mirror layers weighted by their overlap integrals with the electric field of the cavity mode.

1.3.2 Condensates

A Bose Einstein condensate is a macroscopic quantum state that exhibits a spontaneously formed long-range correlation. Free non-interacting Bose particles in thermal equilibrium at temperature T will possess the momentum space distribution[59]

$$n(k) = \frac{V}{8\pi^3}\frac{1}{e^{\frac{1}{k_BT}(\epsilon(k)-\mu)}-1} \tag{1.25}$$

for an energy-momentum dispersion $\epsilon(k)$ where the total number of particles can be accommodated in excited levels for $\mu < \epsilon_0$. If N is larger than a critical particle number, N_c then it is necessary for a large number of particles to occupy the ground state allowing the condition $\sum_k n(k) = N$ to be satisfied. For a fixed particle number, $N_c(T)$ is a continuous function of temperature. Below a critical temperature, T_c condensation occurs, which for an ideal gas is given through

$$k_BT_c = \frac{2\pi\hbar^2}{m}\left(\frac{n}{2.612}\right)^{2/3} \tag{1.26}$$

where k_B is the Boltzmann constant. Below this critical temperature, the momentum distribution is given by

$$n(k) = n_0\delta(k) + \frac{V}{8\pi^3}\frac{1}{e^{\frac{1}{k_BT}\epsilon(k)} - 1} \tag{1.27}$$

This implies that the two-point density matrix is non-vanishing, allowing one to conclude that a condensed system is characterized through a finite long range one body correlation where the off-diagonal long range order leads to a number of interesting effects[125], such as matter-wave interference where one can observe interference patterns between condensates.

At low temperatures, one of the most significant effects in an interacting Bose-gas is superfluidity[125] which has been extensively studied in liquid ^{4}He. In this familiar environment, the presence of superflows and quantized vortices[107, 127] have been well studied, whilst efforts have been made to observe condensation within solid-state systems. Recently, Bose-Einstein condensation of exciton-polaritons has been observed[14, 29, 197] in semiconductors, where in contrast to the situation in dilute gases, these polariton condensates do not exist in equilibrium as the quasi-particles possess a finite lifetime and thus are not a conserved quantity. Instead they exist in a steady state between pump and damping terms, where these condensates may possess significantly different dynamics to those of equilibrium condensates.

In a bulk semiconductor, one can characterize the polariton dispersion relation [150] through the equation

$$\left(\frac{\hbar ck}{\epsilon_B E_k}\right)^2 = 1 + \frac{4\pi\beta}{\left[1 + \frac{E_k}{\hbar\omega_k}\right]^2} \tag{1.28}$$

where β is the exciton polarization constant and $\hbar\omega_k$ is the exciton dispersion and k_B is the Boltzmann constant. In microcavities, this relation is modified and the quasi-particles possess a low mass close to zero momentum. It was suggested that such condensation could be used to enable the creation of an excitonic laser that operates without population inversion[71] which were observed shortly thereafter[14].

It is expected that polaritons will be able to Bose-condense at higher temperatures [16] than observed in systems such as rubidium atoms [74] in an optical trap, due to their light effective mass. Under high excitation, polariton-polariton scattering is sufficiently fast to allow production of a fully thermalized gas [55], and thus allow the existence of collective states to exist[124]. These states are not observed in bulk semiconductors, since there are no stable polariton ground state

within such structures, and bulk polaritons decay radiatively. In 2D microcavities however, a ground state is seen to exist that is associated with a photon-like dispersion, with an effective mass that is five orders of magnitude smaller than that of the bare exciton [68]. As in other quantum condensates [23], one can assign an order parameter, which displays correlations over large distances. In contrast to atomic condensates, this parameter is seen to fluctuate in mesoscopic systems. These fluctuations can be shown to be due to variations in the number of condensed particles brought about by the pumping process [25, 179, 200]. In contrast to condensates of excitons, exciton-polariton condensates maintain coherence as they relax towards their ground state and do not scatter into localized states.

In addition to the critical temperature, several other significant energy scales exist to characterize the interactions of these condensates. The strength of interactions within the system is of the order, nU for characteristic interaction energy per unit energy, U, and a particle density, n measured in m^{-1}. If this energy is small with respect to the thermal energy then the system is said to be weakly interacting. As composite bosons consist of fermions, the binding energy is approximately $\hbar^2/\mu a^2$ for a reduced polariton mass, $\mu \approx 10^{-4} meV$ with a pair correlation length, a. This small mass means that polaritons are rarely in contact since $na^2 << 1$, which is equivalent to stating that the binding energy is large with respect to the thermal energy and thus the composite bosons act as pure bosons[169].

These properties are important for all Bose-Einstein condensates, however for polaritons there are two additional energy scales. One of these is the Rabi frequency, where for a Rabi splitting that is significantly smaller than the thermal energy $\approx k_B T$, thermal excitations in the upper branch work to disrupt the coherent superposition of the excitons and photons that compose the polaritons. This disruption occurs because the upper branch polaritons are exactly out of phase with those on the lower branch. When the Rabi splitting is much larger than the thermal excitation energy, then the interparticle separation is much less than the de Broglie wavelength and one can use this to obtain a length scale for the spatial location of polaritons, if the interparticle distance is significantly larger than the exciton radius.

The remaining energy scale that plays a role in polariton interactions is the energy broadening that is associated with their finite lifetimes, which can be understood through the condition $\Delta E \approx \hbar/\Delta t$. For a microcavity that possesses a

high quality factor, this broadening is typically much less than the Rabi splitting.

The essential feature of polariton condensation is its non-equilibrium state, as it must be sustained by an external source, however under cw excitation working far above the threshold, the system can reach a quasi-thermal equilibrium, wherein the leakage of polaritons through the mirrors is balanced by the increase of polaritons from the incoherent pump. This condensate can then be described by an order parameter Ξ, that defines the direction and phase of the field component in the cavity plane[106].

Having discussed the basic principles of polariton condensation, we now proceed to cover some of the notable properties that influence the work in the following chapters. It is noted that numerous other interesting properties exist and these are discussed in the review by Deng *et al.* amongst others[36, 39, 149].

1.3.3 Photoluminescence

Angle resolved photoluminescence allows for the detection of most spectral properties, by allowing one to obtain the energy (momentum) resolved population of polariton states, in a defined emission cone. This is achieved through optically exciting the semiconductor to produce a polariton population through relaxation of electron-hole states, and allows for the experimental observation of a thermalized spectrum, which mirrors the absorption spectrum after modification by a Boltzmann factor[176]. At low to medium density, the polariton relaxation rate is influenced through three[39] possible mechanisms:

(i) Interplay between Coulomb scattering and phonon relaxation. In the strong coupling region, polaritons undergo Coulomb scattering, such that one polariton scatters to in a lower energy state, whilst the other scatters to the exciton-like higher energy state. Within this higher energy state, the excess energy relaxes through the emission of acoustic phonons, thereby allowing for the observed evolution into a smooth population distribution.

(ii) Scattering of free carriers, originating at charge defects. Polariton states are eigenstates of the crystal coupled to the light-field and thus an ideal polariton does not absorb light, and radiative decay can only occur through interactions with imperfections in the crystal lattice, which gives rise to Rayleigh scattering.

(iii) Structural Disorder may result in localization of polaritons, and thus a lifting of the momentum conservation requirement in the relaxation process.

It is competition between these processes that results in the bottleneck effect,

thereby allowing time for the polariton population to reach thermal equilibrium and yield the observed spectrum[184]. This bottleneck region is located at values of momentum, k close to the anticrossing region where the corresponding polariton energy is equal to the bare exciton energy. This has been observed in both type II-IV[118] and III-V systems[182], where it has been observed to be strongly dependent upon the excitation density.

1.3.4 Polarization

Polaritons possess an integer spin and thus can be treated as bosons at a sufficiently low density where the condition

$$2\pi a_B^2 n_X << 1 \tag{1.29}$$

is satisfied for Bohr radius a_B and exciton density, n_X. In bare quantum wells, the polarization of emitted light has been well-studied[70], where the polarization is directly linked to the spin, through mechanisms that are dependent on the width of the quantum well, temperature and excitation density[114].

In microcavities, these spin dynamics are seen to change substantially due to the mixed character of the polariton. Most notably, there is a finite delay before the polarization degree of the emitted beam reaches its maximum value, and that emission along the lower polariton branch is highly nonlinear. At the minimum of this branch (located at a pump momentum, $k_p = 0$), this nonlinearity arises from stimulated scattering as a result of the bosonic character of polariton states, while on the upper polariton branch at positive detuning above the cavity resonance, however this behavior may be reproduced by fermionic particles that undergo final state scattering.

Classically, the polarization of light can be described through the orientation of the electric field vector at a given spatial location over one period. For a single photon, the right and left-handed circular polarizations can be directly associated with the spin up and down photons. In direct analogy to massive particles, photons can exhibit many of the spin-dependent properties, such as spin-orbit splitting, that are commonly witnessed in those cases. As spin is a conserved quantity in the photo-absorption process, the spin orientation of the excitons are determined by the polarized light beams[115]. Similarly, the polarization of absorbed and emitted light emitted by the cavity is directly connected to the polariton pseudospin[156]. Analysis of these photoluminescence spectra from microcavities

provides a tool for experimental examination of the spin dynamics[21, 134, 171]. These experiments show that the polarization state of a given polariton condensate can be influenced by the effects of the spin dependent interaction between excitons and that of an external magnetic field, whereby the total number of spin up and spin down polaritons is matched in the presence of a linearly polarized pump and the absence of an external field. Furthermore, they show that the polarization of exciting light is not retained indefinitely by excitons due to spin relaxation processes. In the linear regime, the main relaxation mechanism is provided by Transverse Electric-Transverse Magnetic (TE-TM) splitting that leads to the appearance of a momentum dependent magnetic field. The structure of this field leads to numerous interesting effects, particularly an optical analogue of the spin Hall effect. In the nonlinear regime, a number of spin dependent polariton-polariton interactions come into effect, such as Larmor precession of the in-plane pseudospin vector[157] for an elliptically polarized polariton condensate and the inversion of linear polarization through polariton scattering[80, 91].

In the ground state, excitons have two projections along the structure axis, $\pm 1, \pm 2$, which split due to the electron-hole interaction, however the selection rules forbid the optical excitation of states with angular momentum, $J_z = \pm 2$, thus they cannot couple to the photonic mode. The presence of an effective magnetic field serves to mix the different polarization components, thereby allowing for the evolution of the pseudospin. The pseudospin [120, 7, 152, 56] vector, $\vec{P}$ is given by

$$\vec{P} = \begin{pmatrix} \frac{\psi_r^* \psi_l + \psi_r \psi_l^*}{|\psi_r|^2 + |\psi_l|^2} \\ i\frac{\psi_l^* \psi_r - \psi_l \psi_r^*}{|\psi_r|^2 + |\psi_l|^2} \\ \frac{|\psi_r|^2 - |\psi_l|^2}{|\psi_r|^2 + |\psi_l|^2} \end{pmatrix} = \begin{pmatrix} S_x \\ S_y \\ S_z \end{pmatrix} = \begin{pmatrix} \frac{|E_x|^2 - |E_y|^2}{|E_x|^2 + |E_y|^2} \\ \frac{|E_a|^2 - |E_b|^2}{|E_a|^2 + |E_b|^2} \\ \frac{|E_r|^2 - |E_l|^2}{|E_r|^2 + |E_l|^2} \end{pmatrix} = \begin{pmatrix} Q \\ U \\ V \end{pmatrix} \tag{1.30}$$

where $E_a = (E_x + E_y)/\sqrt{2}$ and $E_b = (E_x - E_y)/\sqrt{2}$, when the components of this vector have been re-expressed in terms of the intensities of the different measurable polarized components, and is somewhat analogous to the Stokes vector [19] for light. This effective magnetic field arises in the linear regime through TE-TM splitting, which increases with the value of the in-plane wave vector[183], and is typically of the order of a few μeV. This splitting causes the reorientation allows the generation and control of spin currents within a semiconductor microcavity, when the cavity is initially excited with a linear polarization.

The polarization of the exciting source cannot be preserved indefinitely by the excitons in the well. Whilst there are other mechanisms, spin relaxation occurs primarily through the Bir-Aronov-Pikus mechanism[158], which involves a spin-flip exchange between electrons and holes. This interaction is stronger within bulk semiconductor but is partially reduced inside quantum wells, since the degeneracy between light and heavy hole excitons is lifted. As a result, one can neglect dark states and thus treat the cavity as a two-level system. In reciprocal space, this enables one to describe polaritons through a pseudospin formalism through a 2×2 density matrix

$$\rho_k = N_k \left[\frac{I}{2} + \hat{s_k} \cdot \hat{\sigma_k} \right] \tag{1.31}$$

where $\hat{s_k}$ is the pseudospin vector with a momentum k, $\hat{\sigma_k}$ are the Pauli matrices and N_k is the polariton number. The pseudospin vector components correspond directly to the components of the Stokes vector for the emitted light. Polaritons with opposing spins may interact through virtual dark exciton states, which may lead to the formation of bi-polaritons or polariton condensation in real space. This long-range electron-hole interaction leads to the longitudinal-transverse splitting of exciton states.

Effects of external magnetic fields

In the presence of an external magnetic field, the system tends towards a circularly polarization, and the polariton-polariton interactions that favor the linear polarization. For small fields this results in the formation of an elliptically polarized condensate with the degree of circular polarization, where the Zeeman splitting is completely suppressed. At a critical value of the magnetic field, the polarization becomes fully circular and beyond which the normal Zeeman splitting reappears[158, 192].

It has been observed that the quantization of the exciton continuum into discrete Landau levels in a field results in the creation of resonant anticrossing of the cavity mode with quantized quantum well excitons[186]. In other studies conducted by Armitage *et al.* [12], wherein the excitonic Zeeman splitting was studied as a function of temperature in a magnetic field, $B = 14T$, it was seen that the lower polariton branch couples more strongly to the cavity mode with decreasing temperature, resulting in a decrease in the Zeeman splitting. Increasing the strength of the magnetic field has been observed[181] to increase the excitonic

oscillator strength and a corresponding increase in the vacuum Rabi splitting.

Momentum dependent splitting

As discussed earlier, photon modes possess a strong unquantized in-plane dispersion, where the energy of a photon is given as[149]

$$E(k_{||}) = E_0\sqrt{1 + \frac{h^2c^2k_{||}^2}{E_0^2 n_{eff}^2}} \tag{1.32}$$

for wave-vector, $k_z = 2\pi/L_c$ and in-plane vector $k_{||}$ with an effective index, n_{eff} and $E_0 = hc/n_{eff}L_c$ is the photon energy at $k_{||} = 0$. $k_{||}$ can be related to the external angle of incidence by

$$k_{||} = \frac{E(k)}{hc} sin\theta \tag{1.33}$$

The in-plane momentum can be adjusted by variation of the external angle of incidence. Through this, it is seen that

$$E(\theta) = E_0\left(1 - \frac{\sin\theta^2}{n_{eff}^2}\right)^{-1/2} \tag{1.34}$$

wherein it is evident that the cavity mode energy is strongly dependent upon the angle, and allows the polariton dispersion to be measured directly. One of the notable features in such measurements demonstrates the presence of a splitting between TE and TM modes, that partially arises from the presence of small phase shifts and varying penetration depths into the Bragg mirrors[15].

Spin-dependent Scattering

Polaritons can interact with acoustic phonons, free carriers and other polaritons, which results in the cavity dynamics becoming highly nonlinear. Many experimentally observed phenomena can be explained by polariton scattering acting as the dominant mechanism for relaxation between the bottleneck region and the ground state, where polariton relaxation through acoustic phonons is not efficient[184]. In the case of the optical parametric oscillator, studies of polariza-

tion sensitive events reveal a number of interesting features, such as the rotation of linear polarizations[94, 135] and polarization beats[173].

Polaritons experience an optical analogue of spin hall effect as discussed in reference [78] and demonstrated experimentally within reference [102]. It originates from the combined influence of the polarization splitting of transverse electric and magnetic optical cavity modes, and elastic scattering of polaritons excited by a pump. This dependence of the polariton energy on the angle between the polariton momentum, k_p and its dipole oscillation direction gives rise to a longitudinal transverse splitting. It occurs through the pseudospin precession wherein the effective magnetic field results in the precession of the pseudospin vector, in a manner analogous to the intrinsic spin Hall effect by the Rashba field[163], however the effective field has a different wave vector dependence

$$\Omega_{eff,x} = \frac{\Delta_{LT}(k)}{\hbar}\frac{k_x^2-k_y^2}{k_x^2+k_y^2} \qquad \Omega_{eff,y} = \frac{\Delta_{LT}(k)}{\hbar}\frac{2k_xk_y}{k_x^2+k_y^2} \tag{1.35}$$

where $\Delta_{LT}(k)$ defines the longitudinal-transverse splitting, thus linearly polarized polaritons that travel in different directions will evolve into different polarizations. The presence of disorder does not lead to a significant change in polarization, compared to that associated with Rayleigh scattering of light in a vacuum, while they scatter into an elastic circle within momentum space. When the momentum relaxation is sufficiently slow to allow the pseudospin to rotate through a macroscopic angle before a scattering event, a precession-dominated regime can be achieved, and the pseudospin can be directly observed[102].

Between this spin-dependent scattering and the momentum dependent splitting, we have covered the main mechanisms that give rise to the splitting of polariton polarization states in the microcavity.

Vortex Excitation

The TE-TM splitting can cause an initially circularly polarized distribution to form a phase vortex in the cross-circular polarization[104], characterized by a phase change of 4π. It was observed that polariton-polariton interactions have no significant effect on the polariton distribution, and thus they are not essential for the observation of such vortices, although in the non-linear regime, one can utilize parametric scattering of a Gaussian mode in a parametric oscillator configuration.

1.3.5 Structural Disorder

In real quantum wells, the presence of interface roughness localizes the center of mass exciton wave function[77, 206]. This results in an inhomogeneous broadening of the optical spectrum through a relaxation of the wave-vector conservation law, and the presence of Rayleigh scattering.

This Rayleigh scattering occurs through the presence of localized excitonic states within the quantum well, due to surface roughness that produces the disorder potential in the plane. The filtering of the bare exciton scattering spectrum by the optical response of the microcavity allows one to model the effects of resonant Rayleigh scattering[63, 198].

The effects of disorder on the polariton linewidth can be successfully modeled through the linear dispersion when the microscopic exciton response[198, 199] is taken into account. The observed asymmetry was initially believed to be explained through excitonic motional narrowing[201] however further work[79] suggests that this narrowing near to the anticrossing point is caused by inhomogeneous broadening of the exciton spectrum. Motional scattering however can manifest itself through Rayleigh scattering.

1.4 Optical Parametric Scattering

When two pump polaritons scatter into a lower energy signal and higher energy idler mode with conservation of momentum and energy through $2k_p \rightarrow k_s + k_i$, parametric scattering is said to occur[112].

In optical systems, a parametric nonlinearity with an instantaneous response can occur through a $\chi(2)$ or $\chi(3)$ nonlinearity of the medium[174]. This can lead to conversion of two pump photons into a signal and idler with momenta, k_s, k_i and frequencies δ_s, δ_i respectively, through an interaction with a nonlinear optical crystal, where the presence of an additional weak probe pulse can stimulate this effect. Similar effects have been reported for polariton condensates[35], up to temperatures of $220K$ in CdTe-based microcavities[146], where the breaking of the $U(1)/SO(2)$ symmetry and the subsequent emergence of a Goldstone boson acts to split pairs of pump polaritons into a signal and idler, (as illustrated for the lower polariton branch in figure 1-3) with momentum and energy conservation conditions.

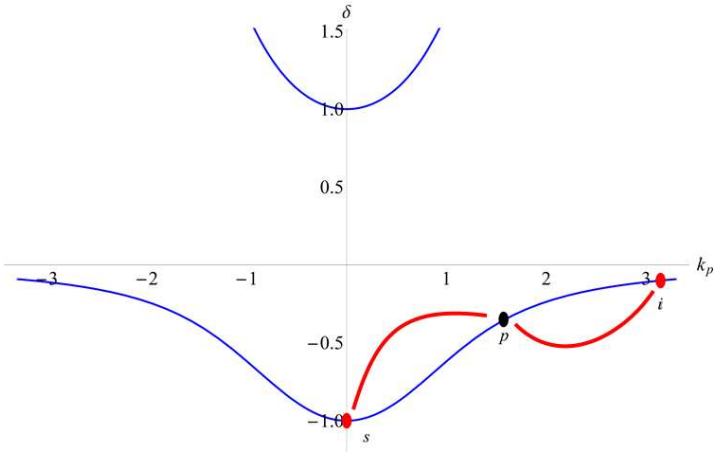

Figure 1-3: *Schematic of Parametric Splitting to signal and idler bands where* $k_s = 0$, $k_p = \pi/2$, *along the lower polariton dispersion branch.*

1.5 Solitons

Solitons are self-reinforcing wave-packets that travel at a constant speed, whilst maintaining their shape. They exist when the nonlinear contribution of the media works to cancel out dispersive effects, in physical systems that are governed by a class of weakly nonlinear dispersive partial differential equations. Solitons can be found in a wide class of equations, ranging from the Korteweg-de Vries equation[89]

$$\frac{d}{dt}\psi + \frac{d^3}{dx^3}\psi + 6\psi\frac{d}{dx}\psi = 0 \tag{1.36}$$

to the nonlinear Schröedinger equation

$$i\frac{d}{dt}\psi = -\nabla^2\psi + f(|\psi|)\psi \tag{1.37}$$

where $f(|\psi|)$ contains terms that are nonlinear in ψ. Solitons were first described by John Russell in 1834[145], and since then their study has proven to be particularly fruitful. They can be found in such diverse areas as particle theory, astronomy[177], oceanic rogue waves[41], Bose-Einstein condensates and optics. In general, there are two main forms of solitons, which are referred to as bright and dark solitons. Dark solitons are formed from a local reduction in the intensity

with respect to the homogeneous background, whilst a localized peak above this background characterizes bright solitons[3, 87].

Matter-wave solitons have been observed in Bose condensates where repulsive interactions balances the presence of an effective negative atomic mass[85, 178] as recently demonstrated within photonic crystals or optical lattices[45]. For polariton condensates, at large momentum above the inflection point, these effects favor the formation of bright solitons in the presence of a probe pulse.

Generally, solitons can be separated into two main types of soliton[5]. Temporal solitons exist when the electromagnetic field is already confined, and pulses do not change their shape due to a balance between nonlinear and dispersive effects. For spatial solitons, the nonlinear effects work to balance diffraction, whilst the electromagnetic field can change the refractive index of the medium to create a structure that resembles graded-index fiber, where the effective index decreases with increasing distance from the pulse center.

Since their initial observation, a number of families have been identified, ranging from gap solitons and breathers to topological solitons. We will only discuss a few of the families here, and direct the reader to the encyclopaedia by A C Scott[155] for a comprehensive overview.

Topological solitons emerge due to a topological constraint of the system. Two of the common forms of these solitons are skyrmions and domain walls, where the former emerges in nuclear models through constraints on the baryon number and the latter is found in condensed matter theories emerging as the interface between distinct ordered regions.

Gap solitons are found in finite gaps in the spectrum of continuous systems. These solitons can be readily studied through the nonlinear Schröedinger equation and are observable in Bose-Einstein condensates[24] and nonlinear optics.

Dissipative solitons are stable localized structures that are often studied in the context of nonlinear reaction-diffusion systems through self-organization. These systems can be modeled through a mean field description of a series of coupled equations that typically take the form[5]

$$\frac{d}{dt}x_i = D_i\nabla^2 x_i + v_i(x_j, \Lambda) \quad (i = 1, ..., n) \tag{1.38}$$

for mass terms, D_i and phenomenological parameters Λ where the interaction terms, v_i are nonlinear in the macroscopic variable, x_j.

1.5.1 Cavity Solitons

Cavity solitons[138, 20] are solitary waves that exist in nonlinear cavities and are a specific expression of dissipative solitons. They are spatially self-localized and possess an exponentially decaying tail that sit on a uniformly patterned background. They are not the fundamental mode of the cavity, rather cavity solitons are excitations that tend to be localized in the directions that are orthogonal to the propagation direction, whilst they are boundary-localized along this axis. In an ideal homogeneous system, stationary cavity solitons can exist at all positions due to translational symmetry. These solitons will move if this symmetry is perturbed until equilibrium is reached. Cavity solitons are lossy, thus need to be driven by an external pump and for a fixed parameter set, they act as an attractor possessing a fixed amplitude. Under these conditions, it is possible either for these solitons to be present or absent.

The behavior of exciton-polariton solitons in the presence of a flat pump in the polariton system has been extensively studied in the absence of spin and the reader is referred to the papers by Egorov *et al.* [42, 43, 44] for a comprehensive discussion.

In these papers, it is seen that moving stable one dimensional cavity polariton solitons exist beyond the inflection point of the lower polariton branch. In two dimensions, it is found that these solitons are sustained by two nonlinear mechanisms along the two orthogonal axes. Co-linear with the pump, this localization occurs due to dispersion from the negative effective mass being balanced by the repulsive polariton-polariton interactions, while orthogonal to the pump direction, the effective mass is positive and localization occurs due to parametric nonlinearities. In the presence of a saturation, these solitons can exist in the gap between upper and lower branches for non-negligible effective exciton masses.

These solitons exist in the bistability region of a system. This can be seen in figure 1-4, where the soliton branch emerges from the point where the homogeneous system becomes unstable [205]. In one dimension, it is simple to obtain the form of these solitons through Newton's method, where the profiles can be observed within figure 1-5. In panels (a) through (c), one can observe that the form of single-hump solitons is similar as one increases the momentum and frequency along the lower branch. In this work, we primarily focus upon single hump solitons but we provide an image of a double-hump soliton in panel (d).

In a two-dimensional space, solitons seeded through a writing beam are seen to be long-lived and through which one can observe that the form of the soliton

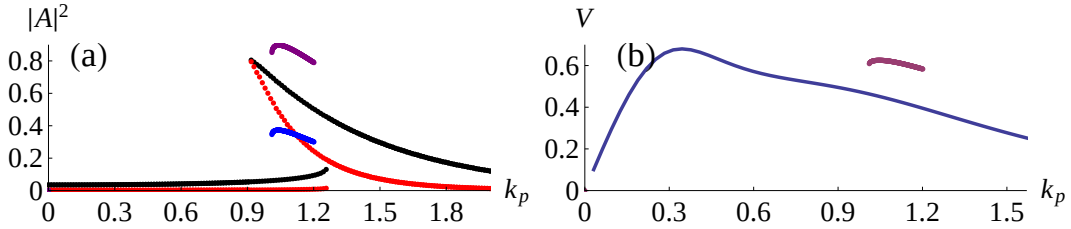

Figure 1-4: *(a) Plot of (red) $|E|^2$ and $|\psi|^2$ (black) against k_p with the corresponding soliton branch displayed in blue (purple).*
(b) Plot of velocity against k_p, where the soliton branch is displayed in purple and the blue curve indicates the velocity of the homogeneous solution. In each case, $\gamma_e = \gamma_{ph} = 0.05$, $\delta_p = -0.184$ and $E_p = 0.180$.

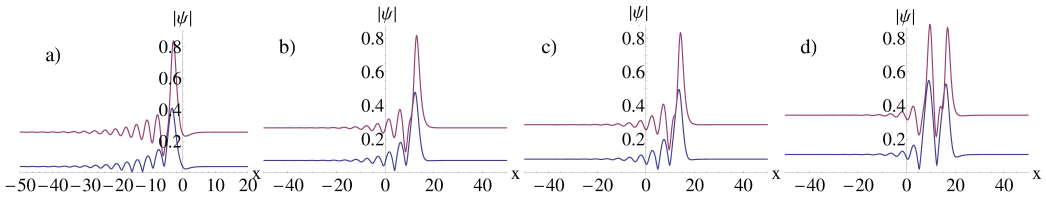

Figure 1-5: *Plots of typical one-dimensional solitons for the parameters: (a) $\delta_p = -0.05$, $E_p = 0.197$, $k_p = \pi/2$ and $\delta_p = -0.184$, $k_p = 1.25$, (b-d) $E_p = 0.1600,\ 0.1664,\ 0.1800$.*

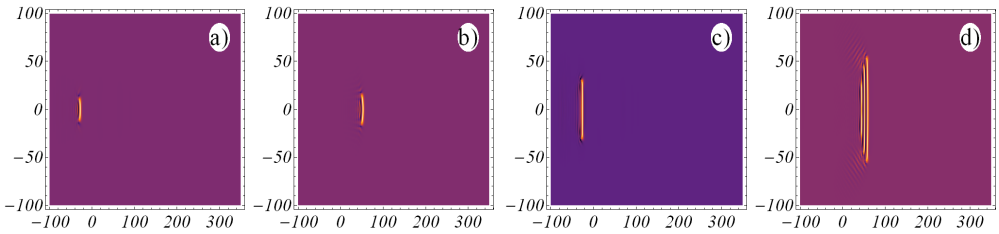

Figure 1-6: *Plots of typical solitons in two dimensions, for* $\delta_p = -0.184$, $k_p = 1.25$ *with (a, b)* $E_p = 0.1600$ *and (c, d)* $E_p = 0.1800$, *at (a, c)* $t = 50$ *and (b, d)* $t = 200$.

is strongly dependent upon the value of the pump momenta. This family of transient solitons exists within a two dimensional space is illustrated within figure 1-6, where the soliton is observed to be expanding along the y-axis. In general however on either side of the Maxwell point where $v_y = 0$, one can observed the shrinking and expansion of a soliton-like object, at lower and higher pump intensities respectively.

1.5.2 Vector Solitons

These solitons were first predicted by Christodoulides in 1988 for a birefringent dispersive media[28], where it is seen that the two polarization components propagate with the same group velocity. These optical vector solitons have been an area of active research, as they possess a wide range of applications, such as the generation of ultrafast pulses[86].

Vector solitons, like scalar solitons, maintain their shape as they propagate, however unlike scalar soliton, they possess multiple polarization components. These multiple components allow for the existence of several classes of vector solitons which are characterized by the presence or absence of a peak in each component, such that there are vector bright solitons, vector dark solitons and vector dark bright solitons. Vector bright and dark solitons are expressed through the presence of a peak or depression, respectively in both polarization components, whilst vector dark bright solitons express a bright soliton in one component and a dark soliton in the other.

1.6 Vortices

Symmetries are ubiquitous in nature, such that one can argue that symmetry breaking is one of the most important observable phenomena in physics. In general, a symmetry breaking transition results in the emergence of an ordered state from a disordered one. One is able to introduce a parameter to provide a measure of this emergent order. This order parameter[128] varies on macroscopic scales in a manner that knowledge of the underlying microscopic structure is negligible with regards to the averaged behavior of the system. In two dimensional wave propagation problems, such as the complex Ginzburg-Landau equation[128, 81] and in numerous other laser models[196, 195], this state of broken symmetry often gives rise to solutions that possess one or more phase singularities[17].

These solutions have been experimentally known for some time in lasers operating in a weak light-matter interaction regime[153], and recently observed with polaritons in the strong coupling regime and play significant roles within other regimes[167, 162, 58, 90]. Now to discuss the emergence of vortices within these regimes, one considers a state of broken symmetry[119, 116] governed by some Lagrangian, L that contains some potential that is invariant under a set of transformations in order parameter space. For which, the simplest state is the uniform stationary state that is a minimum of the potential, while failing to satisfy all the symmetries possessed by the Lagrangian.

This state is asymmetric and neutrally stable with respect to spatially uniform transformations, and as there is no instant communication between spatially separated locations, it will be non-uniform. In this state, separate regions will tend to towards equilibrium, and give rise to diffusional processes. However, if for some reason this cannot occur the solution will locally differ from the minimal manifold, leading to defects in the topology. These deviations from the minimal manifold incur an energetic penalty, raising the effective potential in a small-localized region, which is known as the defect (vortex) core.

In two dimensional space, these defects are known as vortices where a typical profile observed in figure 1-7. These vortices can characterized as a zero density node, possessing a width defined through a healing length, where in non-equilibrium systems, these defects may persist for long durations. The emergence of a defect results in the breaking of symmetry in the system and is accompanied by the appearance of a mode for which the frequency and instability spectrum decay to zero in the long wavelength $k \to 0$ limit. This Goldstone mode can

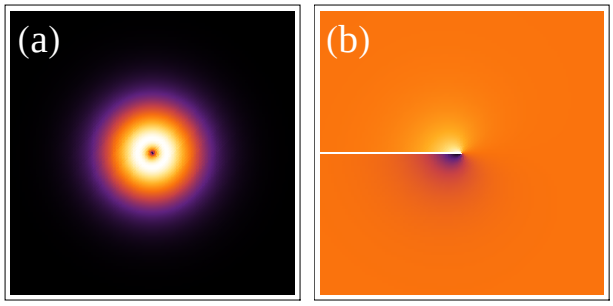

Figure 1-7: *A typical $m = 1$ vortex profile is shown in panel (a), while the associated phase variation is shown in panel (b).*

be defined through phase rotations and that the minimal orbit will be a unit circle[203]. In a polar co-ordinate system, the vortex wave function in the standard radial form, $\psi(r,t) = \sqrt{\eta(r,t)}e^{iS(r,t)}$ where $S(r,t)$ is a macroscopic phase and $\eta(r,t)$ is the fluid density profile and thus

$$\int_C \nabla S \cdot d\underline{l} = 2\pi m \tag{1.39}$$

where the phase change over a closed contours around the vortex must be equal to $2\pi m$ where the winding number, m is an integer. Given that the circulation must be a constant around all contours, the phase gradient must become large as the contour length tends to zero. From which, it is apparent that there must be a phase singularity possessing a topological charge, m. One can use this phase gradient to define a superfluid velocity

$$\underline{v}(\underline{r},t) = \frac{\hbar}{M}\nabla S(\underline{r},t) \tag{1.40}$$

from which one can define a circulation along a contour, C around a single vortex as

$$\Gamma = \int_C \underline{v} \cdot d\underline{l} = m\left(\frac{\hbar}{M}\right) \tag{1.41}$$

and thus, the fluid circulation is quantized in units of $\hbar/M$, with the fluid velocity about the vortex core defined through

$$\underline{v}(r,\theta) = \frac{m}{r}\left(\frac{\hbar}{M}\right)\widehat{\theta} \tag{1.42}$$

where r is the radial distance from the vortex core, M correspond to the condensate mass and $\widehat{\theta}$ is the azimuthal unit vector.

Singly charged vortices are robust as continuous transformations of the vortex profile are unable to eliminate the phase discontinuity, unless the density is close to zero. However higher order vortices ($m > 1$) tend to be energetically unstable within harmonic traps for atomic Bose-Einstein Condensates[202, 131, 109], they split into m singly charged vortices.

Experimentally, vortex generation is typically achieved through rotations, as any rotation of the fluid requires the presences of vortex lines, and thus vortices since the condensate is irrotational. Alternatively, one can imprint the condensate with a vortex lattice through the interference of multiple beams.

Quantized vortices have been extensively studied in the context of optics, condensed matter and coherent matter waves. In the latter case, vortices have been considered as important signatures of superfluidity. More recently, the physics of coherent half-light half-matter fields have attracted significant attention, which have been to a large extent stimulated by a series of successful superfluidity and condensation experiments on microcavity exciton-polaritons[100, 185, 62]. Formally, optical, pure matter and half-light half-matter fields are often described through similar Hamiltonian and dissipative mean field models, where under the latter, we assume the presence of some form of pump in addition to dissipation. Incoherent gain in lasers, specifically in polariton lasers, does not destroy the global phase symmetry ubiquitous in Hamiltonian problems. Therefore vortices in the underlying complex Ginzburg-Landau equation[168, 81], and in other laser models[196] are natural solutions.

In a microcavity pumped with a coherent beam, the global phase symmetry is destroyed and the intra-cavity phase is dictated by that of the pump. One of the more direct methods to generate a polariton vortex in a cavity is to utilize a vortex containing pump. This approach has been applied in recent modeling papers reporting polariton vortices[105] and vortex lattices[165]. After decay of the seed pulse, the symmetry in the global phase is restored and the vortex lifetime is essentially determined by the lifetime of polaritons. Aside from the global phase symmetry, which correlates with the conservation of the total number of particles, there are symmetries in the relative phases of the different harmonics. These are generated through the parametric conversion process and play a role in the intra-cavity dynamics of transverse structures. The relative phase allows the existence of vortices in coherently pumped cavities and it is used below to demonstrate vortex lattices.

In Hamiltonian settings, vortices emerging through symmetries in the relative

phase have been well studied in Raman media[151] and in nonlinear materials with a quadratic dependency. The existence of an optical parametric oscillator regime within wide aperture microcavities is a well-studied effect[69] for exciton-polaritons, wherein it is noted that this four-wave mixing will only occur when the cavity is pumped beyond a critical angle. When one works within this regime, the signal is emitted approximately perpendicular to the cavity plane, whilst emission of the idler occurs at some large angle. Vortices emerging from this four-wave mixing of polaritons have been recently observed experimentally[187].

The presence of optical vortices has been known for some time and their presence is expected to lead to numerous application, especially for optical data storage, processing, and the establishments of optical connections between various electronic components[153, 53, 189].

Nonlinear optical media can be described through their electromagnetic response which is dependent upon the strength of the propagating light, the polarization of which is given by $P = \chi^{(1)}E + \chi^{(2)}E^2 + \chi^{(3)}E^3$, for a field, E and $\chi^{(1)}$ represents the linear refractive index. The parameter, $\chi^{(2)}$ vanishes for symmetric media and as a result, $\chi^{(3)}$ provides the main contribution to the nonlinearity.

In self-focusing media ($\chi^{(3)}E > 0$), this is seen to result in a lensing effect. Laser beams with a topological charge possess a torus like structure. In self-focusing media, such beam profiles are unstable and the vortex beam will decay into a number of bright solitons, breaking the radial symmetry, whilst angular momentum conservation is preserved. However in self-defocusing media, there is no lensing effect and thus bright solitons are not supported, yet a decrease in refractive index can compensate for the spreading of light intensity to create a dark soliton. In such a media, this beam will create a self-trapped vortex soliton[38].

1.7 Patterns and Vortex Lattices

The formation of patterns is an important topic in many disciplines, covering topics as diverse as liquid crystal ordering in chemistry and spontaneous protein folding in biology to the spontaneous symmetry breaking associated with polariton condensation [14, 37]. This symmetry breaking can be treated as an establishment of a macroscopic phase ordering[111].

These patterns emerge through local interactions of the individual elements in a parallel and distributed manner such that a globally coherent form emerges

over time. In some cases, patterns can form spontaneously, while others require an initial seed to stimulate them. In discussing the emergence of these patterns, the concept of an order parameter is often used[60]. These parameters may be either internal to the system or external, such as the pump intensity in a driven microcavity. When this control reaches a critical value, the system will become unstable and adopt a different macroscopic state, often undergoing a non-equilibrium phase transition with symmetry breaking. The resulting patterns can frequently be separated into various classes. Some of these classes are periodic, quasiperiodic, cavity solitons or spirals. Rolls and vortex lattices are typical periodic patterns in the system[24], where the pattern repeats at a regular interval, while quasiperiodic patterns repeat themselves at irregular intervals.

Out of these patterns, we will mainly be concerned with cavity solitons and vortex lattices. Vortex lattices are often periodic arrangements of vortices. In atomic Bose-Einstein condensates, it has long been known that rotation of the condensate will give rise to a persistent Abrikosov lattices[1]. These lattices are triangular due to a minimization of the rotational energy[47]. However through the use of laser-illuminated masks[64], it is possible to form lattices of arbitrary shapes. Patterns generated in this manner can also be observed within nonlinear optical systems[40].

In optics, a set of two pairs of counter-propagating traveling waves will form an arrangement of vortices in a square lattice. These square lattices tend to form a local minimum in parameter space. These lattice are stable, when these pairs of waves are at 90° to one another, however as the orientation is varied the lattice tends towards a rhombic shape[174]. These rhombic lattices eventually become unstable and decay into domains separated by vortex rows.

1.8 Previous Publications

A shortened version of the discussion of honeycomb lattices from section 4.4 has featured within

Vortex Lattices in Coherently Pumped Polariton Microcavities
Physical Review Letters 104, 213903 (2010)
A.V.Gorbach, R.Hartley and D.V.Skryabin[57]

A selection of the topics discussed within chapter 5 have been discussed in the paper

Observation of bright polariton solitons in a semiconductor microcavity
Nature Photonics 6, 50-55 (2012)
M.Sich, D.N.Krizhanovskii, M.S.Skolnick, A.V.Gorbach, R.Hartley,
D.V.Skryabin, E.A.Cerda-Mendez, K.Biermann, R.Hey and P.V.Santos[161]

1.9 Overview

In this chapter, we have focused on providing a brief discussion of the existing literature on the subject of the behavior of polaritons within microcavities, where special attention has been paid to effects associated with Bose-Einstein condensation, specifically vortex dynamics and superfluid effects. The following chapter features a discussion of the theoretical model that we will be using to study the exciton-polariton system.

Beyond which in chapter 3, we discuss the existence and stability of homogeneous solutions in the strong coupling regime, wherein we note that parametric scattering and amplification exists. Following from which, we discuss the behavior of the system under a Gaussian-pumping regime. Under such a regime for a seed and pump of equal width, it is observed that vortex-antivortex pairs form towards the leading edge of the pulse. The form of the roll solution is derived and we proceed to discuss its stability.

Next, we discuss the formation and stability of vortex lattices within the parametric amplification regime, within chapter 4. Specifically, we focus on honeycomb and square lattices, through which we demonstrate that arbitrary lattices can be supported by the parametrically amplified system, close to a single signal momentum that varies with pump strength.

In chapter 5, we introduce the model for polarized condensates. Following which, we return to the honeycomb vortex lattice and discuss their dynamics, wherein it is observed that for each pump intensity, there exist multiple values about which one can observe stable vortex lattices, when the TE-TM splitting is negligible. As for the unpolarized case, these points are dependent upon the form of the lattice in question. In the case where the splitting cannot be ignored, it is seen that the left and right handed circularly polarized component swill possess a different velocity and stability. Each of these half-vortex lattices will evolve independently in the same manner as for the scalar case. Finally, we discuss solitons under different pump polarizations and study a means of controlling their properties.

At this point, we note that since the Rabi frequency can vary over two orders of magnitude depending on the composition of the microcavity all values and figures are presented in arbitrary units unless otherwise stated.

CHAPTER 2

The Theoretical Model

Following on for the previous chapter, where we provided a broad overview of the properties of polaritons, we now discuss the theoretical model that we be using for the majority of this work. Initially we provide a brief discussion of the microscopic derivation of the exciton-polariton system, which is followed by a macroscopic derivation. Beyond which, we discuss the form of the dispersion relation, the presence of the strong coupling regime and the existence domain of nonlinear solutions.

In this work, we are solely interested in the strong coupling regime and as experiments[98] have shown that the presence of incoherent excitons does not significantly affect the behavior of the system in this regime, so they can be safely be neglected.

2.1 The Microscopic Hamiltonian

In quantum well structures, one can adopt a two band description of the electronic system with energy dispersions $E_{1k},\ E_{2k}$ for the single state electron energies in conduction and valence bands respectively. We use the effective mass approximation: $E_{1k} = E_G + \frac{\hbar^2 k^2}{2m_e},\ E_{2k} = -\left(E_G + \frac{\hbar^2 k^2}{2m_h}\right)$, where E_G is half the energy gap while m_e and m_h are the effective masses for electrons in the conduction and valence bands respectively, where the zero of the energy distribution is located halfway between the conduction and valence bands. If one includes the Coulomb

interaction and neglects the effects of spin [31], the Hamiltonian for interacting electrons is

$$H_{el} = \sum_{j,\vec{k}} E_{j,\vec{k}} c^{\dagger}_{j,\vec{k}} c_{j,\vec{k}} + \frac{1}{2} \sum_{j,j',\vec{k},\vec{k'}} V_{\vec{q}} c^{\dagger}_{j,\vec{k}+\vec{q}} c^{\dagger}_{j',\vec{k'}-\vec{q}} c_{j',\vec{k'}} c_{j,\vec{k}} \tag{2.1}$$

where $V_{\vec{q}} = \frac{2\pi e^2}{\epsilon A \vec{q}}$ and $c_{j,\vec{k}}$ is the electron annihilation operator. The interaction term between electrons and cavity photons is given by

$$H_{int} = \sum_{j,\vec{k}} G(\vec{q}) a_{\vec{q}} c^{\dagger}_{\vec{k}+\vec{q}} c_{\vec{k}} + h.c. \tag{2.2}$$

where $G(\vec{q})$ is a Green's function and $a_{\vec{q}}$ is the photon annihilation operator. This is a difficult problem; however, an approximate solution can be achieved by considering excitons possessing the wave function

$$|\phi_{\vec{k}}\rangle = \sum_{q} A(\vec{k},\vec{q}) c^{\dagger}_{1,\vec{q}+\frac{m_e}{M}\vec{k}} c_{2,\vec{q}-\frac{m_h}{M}\vec{k}} |G\rangle \tag{2.3}$$

where $|G\rangle$ is the ground state of the system, $\vec{k}$ is the center of mass momentum wave-vector, and $A(\vec{k},\vec{q})$ is the Fourier transform of the envelope function for the exciton. As they are composed of pairs of fermions, there are no definite statistics yet at moderate densities, these quasi-particles can be treated as bosons, to obtain the effective Hamiltonian

$$\begin{aligned} H_{exc-exc} &= \frac{1}{2} \sum_{\vec{k},\ \vec{k'},\ \vec{q}} V_{\vec{q}} b^{\dagger}_{\vec{k}+\vec{q}} b^{\dagger}_{\vec{k'}-\vec{q}} b_{\vec{k}} b_{\vec{k'}} \\ V_{\vec{q}} &= V_0 = \frac{6e^2 a_{exc}}{\epsilon_0 A} \end{aligned} \tag{2.4}$$

where the effective interaction potential is approximated to a contact potential [73], such that $V^{XX}_{\vec{q}} \approx V^{XX}_0$, for $q << \lambda_X^{-1}$. a_{exc} is the 2D exciton radius, ϵ_0 is the dielectric constant for the confining quantum well, while A is the macroscopic quantization area. This term emerges through a Coulomb interaction between different excitons possessing momenta $\vec{k}$, $\vec{k'}$ respectively. As a prelude to our discussion of the mean field framework, we note that in that framework, the excitonic interaction term

$$H_{exc-exc} = \frac{1}{2}\sum_{\vec{k},\ \vec{k'},\ \vec{q}} V_{\vec{q}} B^{\dagger}_{\vec{k}+\vec{q}} b^{\dagger}_{\vec{k'}-\vec{q}} b_{\vec{k}} b_{\vec{k'}} \approx g\int |\psi|^4 dx \tag{2.5}$$

where g is the exciton interaction constant which is normalized to one in the defined system of units, as it is assumed it can be well described by a contact interaction. As the exciton is a composite boson that consists of a pair of fermions coupled to a photon, there is the interaction

$$H_{XC} = \sum_{\vec{k},\vec{k'},\vec{q}} \frac{\hbar\Omega_R}{\eta_{sat} A} a^{\dagger}_{\vec{k}+\vec{q}} b^{\dagger}_{\vec{k'}-\vec{q'}} b_{\vec{k}} b_{\vec{k'}} + h.c. \tag{2.6}$$

where $\eta_{sat} = 7/16\pi a^2_{exc}$ is the exciton saturation density [137]. The Rabi frequency, Ω_R is the oscillation frequency for a chosen transition in a light field. For a two level system with on resonance light[52], it is defined as

$$\Omega_R = \frac{\vec{d_{i,j}} \cdot \vec{E_0}}{\hbar} \tag{2.7}$$

where $\vec{d_{i,j}}$ is the transition dipole moment for a transition $i \rightarrow j$ and vector electric field amplitude, $\vec{E_0}$. In microcavities[164], this can be re-expressed to yield

$$\Omega_R \approx 2\sqrt{\frac{2\Gamma_0 c N_{qw}}{n_c L_{eff}}} \tag{2.8}$$

where N_{qw} is the number of quantum wells, L_{eff} is the effective length of the cavity, and the radiative linewidth of a free exciton is expressed as

$$\hbar\Gamma_0 = \frac{\pi}{n_c} e^2 4\pi\epsilon_0 \frac{\hbar}{m_e c} f_{ex} \tag{2.9}$$

for exciton oscillator strength per unit area,

$$f_{ex} = \frac{\sqrt{\epsilon_B}}{\pi} \frac{m_e c}{e^2} \omega_{LT} \tag{2.10}$$

and can be related to the exciton polarization, β.

Returning to the polariton system, the Hamiltonian is completed with the addition of the linear terms

$$H^0 = \sum_{\vec{k}} E_C a^\dagger_{\vec{k}} a_{\vec{k}} + \sum_{\vec{k}} E_X b^\dagger_{\vec{k}} b_{\vec{k}} + \sum_{\vec{k}} \hbar\Omega_R a^\dagger_{\vec{k}} b_{\vec{k}} + h.c. \tag{2.11}$$

where the photon energy is defined through $E_C = \hbar\nu\sqrt{k^2 + k_Z^2}$ and exciton energy, $E_X = E_X(0) + \frac{\hbar^2 k^2}{2M}$. By taking the Fourier transform of the full Hamiltonian, we obtain the system [26]

$$\begin{aligned} H &= \int dx \sum_{X,C} \Phi_i^\dagger [h^0_{ij} + V_{ij}\Delta_{ij}]\Phi_j + \frac{\hbar g_X}{2} \int dx \Phi_X^\dagger \Phi_X^\dagger \Phi_X \Phi_X \\ &+ \int dx \hbar F_p e^{i(kx-\omega t)} \Phi_C + h.c. \end{aligned} \tag{2.12}$$

where Φ_X and Φ_C are the annihilation operators for exciton and photon fields respectively. The resulting matrices are

$$\begin{aligned} h^0 &= \hbar \begin{pmatrix} \omega_c(-i\nabla) & \Omega_R \\ \Omega_R & \omega_x(-i\nabla) \end{pmatrix} \\ V &= \begin{pmatrix} U(x,y) & 0 \\ 0 & |\psi|^2 \end{pmatrix} \end{aligned} \tag{2.13}$$

and the terms $\omega_c(-i\nabla)$ and $\omega_x(-i\nabla)$ denote the dispersion relations for cavity photons and excitons respectively.

One can expand this Hamiltonian in terms of fluctuations about the mean of the fields. By consideration of the leading order, one can obtain a mean field theory, wherein there are no fluctuations about this mean, and one has effectively replaced many possible interactions with a single one. Following this through, one can obtain a mean-field model for cavity polaritons, as given in section 2.3.

2.2 The Macroscopic Cavity Polariton Model

In the previous section, we have discussed a microscopic approach to the derivation of the model for cavity polaritons; however, a macroscopic approach also exists to arrive at this system. We start from a pair of coupled equations

$$\frac{d^2}{dt^2}P_r + 2\gamma_e \frac{d}{dt}P_r + \omega_p^2(P_r - \alpha_3 P_r^3) = \epsilon_0 \chi_\infty^{(1)} \omega_c^2 E$$

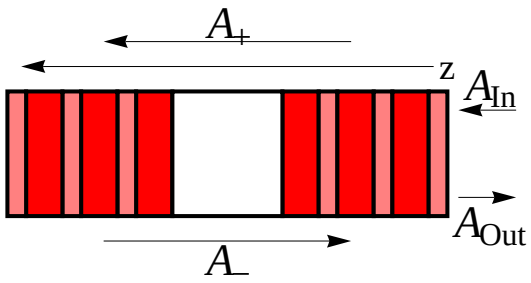

Figure 2-1: *Schematic of the cavity of reflectivity ρ, illustrating the alignment of the standing wave components, $A_{\pm}$, A_{in} and A_{out}.*

$$\frac{d^2}{dz^2}E \quad - \quad \frac{1}{c^2}\frac{d^2}{dt^2}E = \mu_0 \frac{d^2}{dt^2}(P_r + P_h) \tag{2.14}$$

where $\alpha_3 > 0$ so that one is working with a focusing nonlinearity, ϵ_0 denotes the absolute permittivity, μ_0 is the absolute permeability.

Now as illustrated within figure 2-1, we expand the fields as standing waves aligned perpendicular to the cavity-plane

$$\begin{aligned} E &= A_+ e^{ik_z z - i\omega t} + A_- e^{-ik_z z - i\omega t} + c.c. \\ P_r &= P_{r+} e^{ik_z z - i\omega t} + P_{r-} e^{-ik_z z - i\omega t} + c.c. \\ P_h &= P_{h+} e^{ik_z z - i\omega t} + P_{h-} e^{-ik_z z - i\omega t} + c.c. \end{aligned} \tag{2.15}$$

for a waves traveling along the z-axis, perpendicular to the cavity-plane with momentum, k_z and frequency, δ to obtain

$$\begin{aligned} -2i\omega_c \frac{d}{dt}P_{r+} \quad - \quad & 2i\gamma_e \omega P_{r+} + (\omega_p^2 - \omega_c^2)P_{r+} - 3\omega_p^2 \alpha_3 (|P_{r+}|^2 + 3|P_{r-}|^2)P_{r+} \\ = \quad & \epsilon_0 \chi_\infty^{(1)} \omega_c^2 A_+ \\ -2i\omega_c \frac{d}{dt}P_{r-} \quad - \quad & 2i\gamma_e \omega P_{r-} + (\omega_p^2 - \omega_c^2)P_{r-} - 3\omega_p^2 \alpha_3 (|P_{r-}|^2 + 3|P_{r+}|^2)P_{r-} \\ = \quad & \epsilon_0 \chi_\infty^{(1)} \omega_c^2 A_- \\ 2ik\frac{d}{dz}A_+ \quad + \quad & \frac{2i\omega}{c}\frac{d}{dt}A_+ - k_z^2 A_+ + \frac{d^2}{dx^2}A_+ - \frac{\omega^2}{c^2}A_+ \\ = \quad & -\mu_0 \omega^2 (P_{r+} + P_{h+}) \\ -2ik\frac{d}{dz}A_- \quad + \quad & \frac{2i\omega}{c}\frac{d}{dt}A_- - k_z^2 A_- + \frac{d^2}{dx^2}A_- - \frac{\omega^2}{c^2}A_- \\ = \quad & -\mu_0 \omega^2 (P_{r-} + P_{h-}) \end{aligned} \tag{2.16}$$

where γ_e represents the exciton damping, while ω_p and ω_c denote the resonance frequencies for the photon and cavity modes respectively. Now, we take the Fourier transform

$$A_{\pm} = \int \widetilde{A_{\pm}} e^{ik_x x - i\delta t} dk_x d\delta \tag{2.17}$$

and recalling that the microcavity consists of alternating layers which possess different refractive indexes, we make the substitution

$$\widetilde{P_h} = \epsilon_0 \chi^1_{\infty}(\omega)\widetilde{E} + 2\epsilon_0 n_h n_{2h} |\widetilde{E}|^2 \widetilde{E} \tag{2.18}$$

for refractive indexes, n_h and n_{2h} which are associated with the two media respectively to obtain

$$\begin{aligned} 2ik_z \quad & \frac{d}{dz}\widetilde{A_+} + \frac{2\omega_{\infty}}{c}\widetilde{A_+} - k^2\widetilde{A_+} - k_x^2\widetilde{A_+} - \frac{\omega^2}{c_z}\widetilde{A_+} = -\mu_0\omega_c^2(\widetilde{P_{r+}} + \widetilde{P_{h+}}) \\ = \quad & -\mu_0\omega_c^2(\widetilde{P_{r+}} + \epsilon_0\chi^1_{\infty}(\omega - \omega_c))\widetilde{A_+} + 2\epsilon_0 n_h n_{2h}(|A_+|^2 + 2|A_-|^2)\widetilde{A_+} \end{aligned} \tag{2.19}$$

and thus

$$2ik_z\frac{d}{dz}\widetilde{A_+} + \frac{2\omega_c\delta}{c}\widetilde{A_+} - k_x^2\widetilde{A_+} = -\mu_0\omega_c^2(\widetilde{P_{r+}} - \epsilon_0\chi^1_{\infty}\delta\widetilde{A_+} + \epsilon_0 n_{nl+}\widetilde{A_+}) \tag{2.20}$$

where we have defined a nonlinear refractive index through

$$n_{nl\pm} = 2n_h n_{2h}(|A_{\pm}|^2 + 2|A_{\mp}|^2) \tag{2.21}$$

through which, we have the system

$$i\frac{d}{dz}\widetilde{A_+} + \frac{1}{2k_z}(\frac{2\omega_c}{c} - \frac{\omega_c^2}{c^2}\chi^{(1)}_{\infty})\delta\widetilde{A_+} - \frac{k_x^2}{2k_z}\widetilde{A_+} + \frac{\omega_c^2}{2k_z c^2}n_{nl+}\widetilde{A_+} = -\frac{\mu_0\omega_c^2}{2k_z}\widetilde{P_{r+}} \tag{2.22}$$

and similarly for A_-. Now the difference between the group velocity, v_g and $c/n_{nl+} \approx c/n_{nl-}$ is negligible, so one has

$$i\frac{d}{dz}\widetilde{A_+} + \frac{1}{v_g}\delta\widetilde{A_+} - \frac{k_x^2}{2k_z}\widetilde{A_+} + \frac{k_z}{2h^2}\widetilde{A_+} = -\frac{\mu_0\omega_c^2 n_{nl+}}{2c}\widetilde{P_{r+}} \tag{2.23}$$

$$-i\frac{d}{dz}\widetilde{A_-}+\frac{1}{v_g}\delta\widetilde{A_-}-\frac{k_x^2}{2k_z}\widetilde{A_-}+\frac{k_z}{2h^2}\widetilde{A_-}=-\frac{\mu_0\omega_c^2}{2k_z}\widetilde{P_{r-}} \tag{2.24}$$

$$\begin{aligned}-i\frac{d}{dt}P_{r+} &- i\gamma_e P_{r+}+\frac{\omega_p^2-\omega_c^2}{2\omega_c}P_{r+}-\frac{3}{2}\omega_p\alpha_3(|P_{r+}|^2+2|P_{r-}|^2)P_{r+}\\ &= \epsilon_0\chi_\infty^{(1)}\omega_c^2A_+\end{aligned} \tag{2.25}$$

Now, we re-express this to arrive at

$$i\frac{d}{dz}\widetilde{A_+}+m_+\widetilde{A_+}=-\alpha\widetilde{P_-} \tag{2.26}$$

$$-i\frac{d}{dz}\widetilde{A_-}+m_-\widetilde{A_-}=-\alpha\widetilde{P_+} \tag{2.27}$$

where

$$\begin{aligned}\alpha &= \frac{\mu_0\omega_c^2}{2k_z}\\ m_\pm &= \frac{i}{v_g}(-i\delta)+\frac{(\pm ik_x)^2}{2k_z}+\frac{k_z}{2h^2}n_{nl\pm}\end{aligned}$$

Now, we enforce the boundary conditions for a cavity possessed of a reflectivity, ρ and length d. These conditions are given by

$$\begin{aligned}\widetilde{A_+} &= \tau\widetilde{A_{in}}+\rho\widetilde{A_-}^2|_{z=0}\\ \widetilde{A_-} &= \rho\widetilde{A_+}|_{z=d}\\ \tau\widetilde{A_-} &= \widetilde{A_{out}}|_{z=0}\end{aligned}$$

and make the substitutions

$$\begin{aligned}\widetilde{A_+} &= a_+e^{im_+z}+i\alpha e^{im_+z}\int_\alpha^z e^{-im_+z}\widetilde{P_{r+}}dz=(a_++F_+(z))e^{im_+z}\\ \widetilde{A_-} &= a_-e^{-im_+z}-i\alpha e^{im_-z}\int_\alpha^z e^{-im_-z}\widetilde{P_{r-}}dz=(a_--F_-(z))e^{im_-z}\end{aligned} \tag{2.28}$$

where

$$\begin{aligned} F_{\pm}(z) &= i\alpha \int_{\alpha}^{z} e^{\mp i m_{\pm} z} \widetilde{P_{r\pm}} dz \\ F_{\pm}(d) &= 0 \end{aligned}$$

At the $z = d$ boundary where $\widetilde{A_{-}} = \rho \widetilde{A_{+}}$, we have

$$\begin{aligned} \rho a_{+} e^{i m_{+} d} &= a_{-} e^{-i m_{-} d} \\ a_{+} &= a e^{-i m_{+} d} \\ a_{-} &= \rho a e^{+i m_{-} d} \end{aligned} \tag{2.29}$$

whilst at along the $z = 0$ boundary

$$a(e^{-i m_{+} d} - \rho^2 e^{i m_{-} d}) = \tau - F_{+}(0) - \rho F_{-}(0) \tag{2.30}$$

and thus

$$\begin{aligned} \tau \rho a e^{i m_{-} d} &= \widetilde{A_{out}} \\ \frac{\widetilde{A_{out}}}{\tau \rho}(e^{-i d(m_{+}+m_{-})} - \rho_2) &= \tau \widetilde{A_{in}} - F_{+}(0) - \rho F_{-}(0) \end{aligned} \tag{2.31}$$

making a Taylor expansion up to $O(\epsilon^2)$ in the transmission coefficient, τ to find that at the boundaries, one has the solution

$$(1 - \rho^2 - i d(m_{+} + m_{-}))\widetilde{A_{out}} = \tau^2 \rho \widetilde{A_{in}} - \tau \rho (F_{+}(0) + \rho F_{-}(0)) \tag{2.32}$$

where

$$\begin{aligned} F_{\pm}(0) &= i\alpha \int_{d}^{0} e^{\mp i m_{\pm} z} \widetilde{P_{r\pm}} dz \\ &\approx i\alpha \int_{d}^{0} \widetilde{P_{r\pm}} dz \approx -i\alpha d \widetilde{P_{r\pm}}(z = z_0) \end{aligned} \tag{2.33}$$

with $A_{out}, A_{in}, \tau^2, d, \epsilon$ are small. Thus, one has

$$\widetilde{A_{\pm}}(z = z_0) = a_{\pm} e^{\pm i m_{\pm} z_0} + O(\epsilon) = a_{\pm} + O(\epsilon) \tag{2.34}$$

which provides

$$\widetilde{A_{+}}(z = z_0) = a + O(\epsilon) \approx \frac{1}{\rho\tau}(\widetilde{A_{out}} + O(\epsilon)) \tag{2.35}$$

$$\widetilde{A_{-}}(z = z_0) = \rho a + O(\epsilon) \approx \frac{1}{\tau}(\widetilde{A_{out}} + O(\epsilon)) \tag{2.36}$$

where it is assumed that the mirrors are perfect such that $\rho \approx 1$. Using this, it follows that

$$(\tau^2 - id(m_+ + m_-))\widetilde{A_{out}} = \tau^2 \widetilde{A_{in}} + 2i\alpha\tau d(\widetilde{P_{r+}}|_{z=z_0} + \widetilde{P_{r-}}|_{z=z_0}) \tag{2.37}$$

Now, we assume

$$\widetilde{P_{r+}}|_{z=z_0} = \widetilde{P_{r-}}|_{z=z_0} = \widetilde{P_r}|_{z=z_0} = \widetilde{\psi} \tag{2.38}$$

and let $\tau \to 0$, while recalling

$$\widetilde{A_{+}} = a + ... = \frac{\widetilde{A_{out}}}{2\rho} \tag{2.39}$$

$$\widetilde{A_{-}} = \rho a + ... = \frac{\widetilde{A_{out}}}{2} \tag{2.40}$$

which after transforming back to real space, where ψ is related to $\widetilde{\psi}$ through equation 2.17 to obtain

$$\begin{aligned} (\tau^2 \quad - \quad & 2id(\frac{i}{v_g}\frac{d}{dt} + \frac{1}{2k_z}\frac{d^2}{dx^2}))A_{out} - 6id\frac{k_z}{\tau^2}\frac{n_{2h}}{n_h}|A_{out}|^2 A_{out} \\ = \quad & \tau^2 A_{in} e^{i\omega_c t} + 2i\alpha\tau d\psi \end{aligned} \tag{2.41}$$

$$-i\frac{d}{dt}\psi - i\gamma_e\psi + \frac{\omega_p^2 - \omega_c^2}{2\omega_c}\psi - \frac{g}{2}\omega_p\alpha_3|\psi|^2\psi = \epsilon_0\chi_\infty^{(1)}\frac{\omega_c^2}{\tau}A_{out} \tag{2.42}$$

We let $E = A_{out}$ and reformulate the system to obtain

$$\frac{2d}{v_g}\frac{d}{dt}E - \frac{id}{k_z}\frac{d^2}{dx^2}E + \tau^2 E - 6i\frac{dk_z n_{2h}}{n_h \tau^2}|E|^2 E = \tau^2 A_{in} e^{i(\omega_c - \omega_p)t} + 2i\alpha\tau d\psi \quad (2.43)$$

and

$$\frac{d}{dt}\psi \quad + \quad \gamma_e\psi + i(\omega_p - \omega_c)\psi - i\frac{g}{2}\omega_p\alpha_3|\psi|^2\psi = i\epsilon_0\chi_\infty^{(1)}\frac{\omega_c^2}{\tau}E \quad (2.44)$$

Finally, we rescale the system to obtain

$$\begin{aligned}\frac{d}{dt}E - i\nabla^2 E + \gamma_{ph}E - i\mu|E|^2E &= i\Omega_R\psi + E_p e^{i\vec{k}\cdot\vec{x} + i(\omega_c - \omega_p)t} \\ \frac{d}{dt}\psi + \gamma_e\psi - i\epsilon|\psi|^2\psi &= i\Omega_R E \end{aligned} \quad (2.45)$$

where it has been assumed that the resonances of the cavity, ω_c and the photon modes, ω_p coincide. We assume that the photon self-interaction term is negligible and make the substitution

$$E(\underline{x}, t) = E(\underline{x}, t)e^{-i\delta_p t}, \quad \psi(\underline{x}, t) = \psi(\underline{x}, t)e^{-i\delta_e t}$$

so that the frequency dependence is explicit and thus we arrive at the mean field model for microcavity exciton-polaritons as desired.

2.3 The Mean-Field Model

From the previous two sections, we have seen that the mean-field model for cavity polaritons [32, 44, 30, 43] has the form

$$\frac{d}{dt}E - i\nabla^2 E + (\gamma_{ph} - i\delta_p - iU(x,y))E = i\Omega_R\psi + E_p e^{ik_p\cdot x} \quad (2.46)$$

$$\frac{d}{dt}\psi + \left(\gamma_e - i\delta_e + i|\psi|^2\right)\psi = i\Omega_R E \quad (2.47)$$

when consider through either a microscopic or a macroscopic approach. E and ψ can be taken as the average of creation or annihilation operators for cavity photons and excitons, respectively and thus are related to the numbers of particles

present in the fields.

For such a system of weakly interacting bosons, there will only be weak fluctuations about the mean field solution when the system is dynamically stable. In which case, the mean field will accurately model the coherent aspect of the polariton field, and thus the coherent emission from the microcavity [25].

The exciton as a Coulomb correlated electron hole pair is understood to be the elementary excitation within a solid that carries no net charge and possesses an energy that is slightly less than that of its constituent parts. In the low density limit, they are seen to obey Bose statistics. $U(x,y)$ is a potential felt only by the photons. Ω_R is the Rabi frequency, while γ_{ph} and γ_e are damping parameters for the exciton and cavity photon respectively. Finally, E_p is the amplitude of the pumping laser which impart a momentum, k_p, and is related to the pump intensity through[25]

$$I_p = \frac{c}{2\pi}|E_p|^2 \tag{2.48}$$

In this form, it can be clearly seen that nonlinearity arises solely through interactions between the excitonic components.

These equations are normalized[205] such that $\Omega_R|E|^2$ and $\Omega_R|\psi|^2$ are the photon and exciton numbers per unit area. Co-ordinates are chosen so that each unit along a given axes represents $x = \sqrt{c/2kn\Omega_R}$, where c is the speed of light in a vacuum, n is the refractive index, whilst the wavenumber $k = n\omega/c$, with a single time unit corresponding to $1/\Omega_R$. The pump amplitude, $|E_p|^2 = \gamma_c I_{inc}/\hbar\omega\Omega_R^2$, where I_{inc} is the incident intensity. The detuning parameter for the photonic and excitonic components are represented by δ_p and δ_e respectively.

In a microcavity, one can create exciton-polaritons through any method that is capable of creating electrons and holes within a quantum well, which is typically achieved by illumination of the cavity with a laser. The absence of a kinetic term within the exciton equation, arises because the effective mass of the exciton is very much greater than the effective mass of the photon, which can be determined through the dispersion relation, as displayed through the red line as shown in figure 2-2, and thus terms proportional to $1/M$ may be neglected.

Through varying the angle of incidence of the pump beam with respect to the cavity, one is able to vary the momentum of the photons within the cavity, through variation of either the angle of incidence, θ or the momentum of the pump, k_z through the scheme illustrated in figure 2-3.

The damping term, γ_{ph} is determined by the lifetime of the cavity photons.

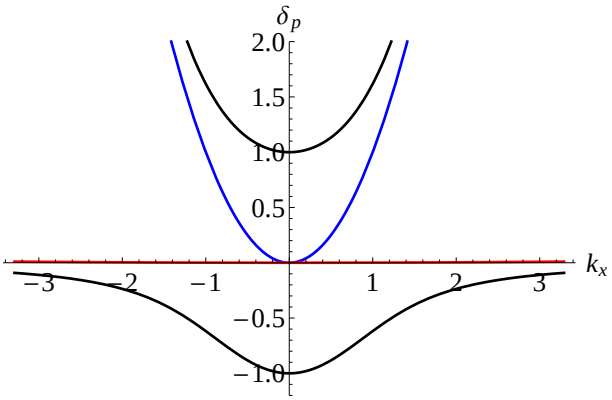

Figure 2-2: *Dispersion relation for polaritons, where the red and blue lines show the dispersion relation for excitons and photons respectively, where it is highlighted that in the vicinity of $k = 0$, the excitonic dispersion relation is almost flat. The black lines display the upper and lower branches of the polariton dispersion relation.*

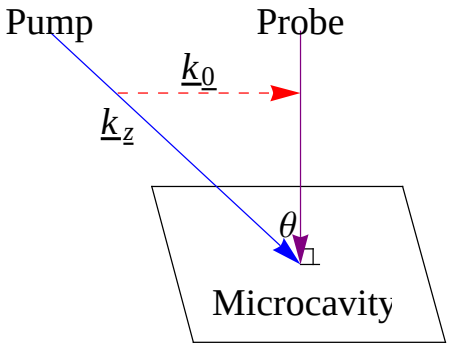

Figure 2-3: *Schematic illustrating the typical arrangement of pump, probe and cavity.*

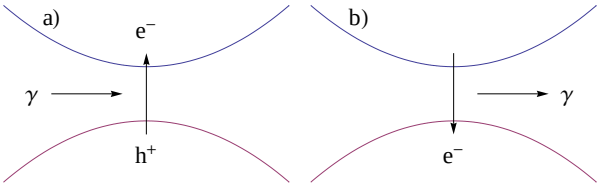

Figure 2-4: *(a) Schematic illustrating excitation of an electron, e^- from the valence band to the conduction band, leaving a hole, h^+, in the valence band. Panel (b) illustrates the decay of an electron from the conduction band through the emission of a photon.*

Within the microcavity for photon-exciton interactions, only the in plane momentum in conserved and excitons with momentum $k_{||}$ will only interact with photons possessing the same in-plane momentum and arbitrary momentum along the growth direction of the cavity. As the photon momentum perpendicular to the plane is not conserved, photons are able to escape the cavity through this direction. The lifetime of excitons within the cavity provides the magnitude of the term, γ_e. As excitons are formed from a conduction band electron coupled to a hole in the valence band, it is evident that after a period of time the electron will emit a photon, decaying back to the lower energy level, filling the hole and thus removing the exciton from the system, as illustrated in figure 2-4.

The term $U(x, y)$ acts as an effective potential for light, that is brought about through the imposition of a spatially varying shift of the cavity resonance. Experimentally, one can induce spatially varying shifts of this form through the variation of the thickness of the epitaxial layers, such that the intrinsic detuning from the resonance varies. This variation results within the creation of this potential. When electrons transition between energy levels, photons are emitted. These emissions serve to excite the medium and are subsequently re-emitted in a cascade, which gives rise to oscillations at the Rabi frequency, Ω_R as the excitons are generated through a dipole allowed electronic interband transition. This coupling between photons and excitons can become saturated when the normalized exciton saturation density ($n_s = \eta_{sat} g/\Omega_R$) is small. This saturation can be approximated for moderate saturation as $\Omega_R \to \Omega_R(1 + |\psi|^2/n_s)^{-1/2}$, however a rigorous account requires a treatment of excitons as bound fermions[39], which will not be covered here.

The detuning parameter, $\delta_p = (\omega - \omega_p)/\Omega_R$ is defined through the separation of the pump frequency, ω from the resonance of the excitonic transition within a quantum well that occurs at the frequency, ω_c. A microcavity typically consists of

a planar Fabry-Perot resonator with two Bragg mirrors [74] at resonance with the excitons in quantum wells, where a quantum well serves to confine particles within a planar region. This confinement typically occurs when the thickness of the well is comparable to the de Broglie wavelength of the carriers at approximately $7nm$ [136, 124].

2.4 The Dispersion Relation

In the strong coupling regime, the polariton dispersion relation possesses two branches. As we will demonstrate, upon the lower branch, the dispersion is strongly non-parabolic around the anticrossing point, which has a number of significant consequences that contribute to the achievement or non-achievement of a quasi-equilibrium polariton distribution.

Having discussed the origins of the mean field model, we begin our discussion of the dispersion relation by determining the eigenvalues of the system through the substitution of wave solutions of the form $E = E_0 e^{-i\mu t + ik_p x}$ and $\psi = \psi_0 e^{-i\mu t + ik_p x}$. In the absence of nonlinear terms, this yields the eigenvalue equation

$$i\mu_{\pm}(k_p) \begin{pmatrix} E_{k_p} \\ \psi_{k_p} \end{pmatrix} = \begin{pmatrix} ik_p^2 + \gamma_{ph} - i\delta_p & -i\Omega_R \\ -i\Omega_R & \gamma_e - i\delta_e \end{pmatrix} \cdot \begin{pmatrix} E_{k_p} \\ \psi_{k_p} \end{pmatrix} \tag{2.49}$$

where $\mu_{\pm}$ are the eigenvalues. From this, one can determine that the eigenvalues are

$$\begin{aligned} \mu_{\pm} &= \frac{1}{2}\left(i(k_p^2 - (\delta_p + \delta_e)) + (\gamma_{ph} + \gamma_e)\right) \\ &\pm \frac{1}{2}\sqrt{-(k_p^2 + i(\gamma_{ph} - \gamma_e))^2 - 4\Omega_R^2} \end{aligned} \tag{2.50}$$

Now, we consider the resonance conditions for the upper and lower branches as expressed through

$$Re[\mu_+] = 0 \quad Re[\mu_-] = 0 \tag{2.51}$$

respectively yields the dispersion relations

$$\delta_p = \frac{1}{2}(k_p^2 - \Delta \pm \sqrt{k_p^4 + 4\Omega_R^2}) \tag{2.52}$$

where $\Delta = \delta_e - \delta_p$, as has been displayed previously in figure 2-2, for the case of $\Delta = 0$.

The Strong Coupling Condition

At this point, we take a brief detour to derive the condition for strong coupling. Close to the exciton transition resonance, the strong coupling regime is characterized by the presence of an anticrossing such that two distinct branches are manifest. We start by taking the difference between the eigenvalues, $\mu_\pm$ shown in equation 2.50. When the photon and exciton resonances coincide ($\delta_e = \delta_p$), the boundary between the weak and strong regimes can be characterized by

$$\mu_+ - \mu_- = \sqrt{-(k_p^2 - i(\gamma_e - \gamma_{ph}))^2 - 4\Omega_R^2} = 0 \tag{2.53}$$

through which it is seen that the upper and lower branch will touch when

$$\Omega_R = \frac{|\gamma_e - \gamma_p|}{2} \tag{2.54}$$

and thus the system is strongly coupled when $\Omega_R > |\gamma_e - \gamma_{ph}|/2$ is satisfied, and there is an anticrossing in the system. When this condition is false, the branches cross and the system is only weakly coupled. We insert this condition into the dispersion relation to obtain

$$\delta_p = \frac{1}{2}\left(k_p^2 \pm \sqrt{k_p^4 + \gamma_e^2 - 6\gamma_e\gamma_{ph} + \gamma_{ph}^2}\right)$$

so that the differences between these regimes are evident, as can be observed in figure 2-5.

Existence Domain of Nonlinear Polaritons

Now, we proceed to determine the domain of existence for nonlinear polaritons. Again, we return to the core system of equations 2.47 and initially consider only the time independent form of the second of the pair in the absence of damping to find

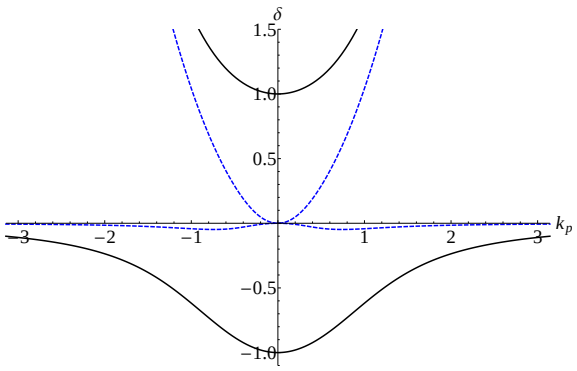

Figure 2-5: *Plot of frequency $\delta = \delta_e = \delta_p$ against momentum, k_p, displaying the dispersion relations for the weak ($\Omega_R = 0.24$) (blue, dashed) and strong ($\Omega_R = 1$) (black) coupling regimes, where $\gamma_e = 0.6$ and $\gamma_{ph} = 0.1$.*

$$E = \frac{|\psi|^2 - \delta_e}{\Omega_R}\psi \tag{2.55}$$

Now, we require that $\psi = Be^{ik_p x}$ and substitute into the remaining equation in the absence of a potential to obtain the equations

$$B\left(-\Omega_R^2 + (|B|^2 - \delta_e)(k_p^2 - \delta_p)\right) = 0 \tag{2.56}$$

which one solves for $|B|^2$, while neglecting the trivial solution to yield

$$|B|^2 = \delta_e - \frac{\Omega_R^2}{-k_p^2 + \delta_p} \tag{2.57}$$

Given that $|B|^2 \geq 0$, one is able to place conditions on the possible values of the detuning parameter to obtain the conditions

$$\delta_p + \delta_e \geq k_p^2 \pm \sqrt{k_p^4 + 4\Omega_R^2} \tag{2.58}$$

These conditions are associated with the upper $(+)$ and lower $(-)$ polariton branches, respectively, while it is evident that the minimum of each branch is located at $k_x = 0$. At which, it is observed that one has the identical condition $\frac{1}{4}(\delta_p + \delta_e)^2 - \Omega_R^2 \geq 0$ and through which one determines that the lower branch extends from $(\delta_p + \delta_e) = -2\Omega_R$ to the cavity and exciton resonance while on the upper branch, nonlinear polaritons may exist at all values of the detuning parameter where $(\delta_p + \delta_e) \geq 2\Omega_R$.

For the remainder of this work, we operate within the strong coupling regime and focus on the lower branch of the dispersion relation where the excitonic component of the quasiparticles is significant to allow for strong interactions.

2.5 Summary

We began this section with a review of the microscopic deviation of exciton-polariton system, using the creation and annihilation operators. Following which, we have provided the equivalent macroscopic derivation of this system. Through which, it is apparent that under a mean field approximation, it is seen that the systems are equivalent. Beyond which, we discuss the existence domain of nonlinear solutions was then discussed and we provide the derivation of the dispersion relation within the strong coupling regime.

CHAPTER 3

Modulation Instability for Exciton-Polaritons

Modulation instability occurs where deviations from a waveform are reinforced by the action of nonlinear components within the system that results in the generation of spectral sidebands[4]. It is typically highly sensitive to the frequency of the perturbation, such that only certain frequencies will result in an exponential growth, while perturbations at different frequencies will have decay exponentially.

The control of polariton interactions has significant fundamental and practical interest due to potential uses in various photonic applications. Recently, this interest has given rise to numerous studies by van Vugt *et al.* [191] amongst others[103, 133, 164, 193] that focus on increasing the magnitude of the Rabi Splitting to allow the fabrication of better quality microcavities to aid in the design of room temperature polariton lasers as seen in the work of Kena-Cohen *et al.* [84] amongst other applications[110].

As many potential applications of polaritons rely upon this regime, we begin this chapter with an examination of the system in the strongly coupled regime to determine the stability of the homogeneous system. When parametric instabilities are present, modulation instability results in the formation of various patterns[18, 111]. These works illustrate that these experimentally observed self-organization phenomenon can be described through a mean-field Gross-Pitaevskii equation. This pattern formation can be taken as a consequence of condensation into a single energy state. When the system is driven in the unstable parametric scattering regimes, the system will break into a large number of signal-idler pairs and result

in the amplification of many unstable harmonics. Self-organization leads to the elimination of most of these, such that only one macroscopically occupied state remains. The interactions of this signal-idler pair with the pump in the strongly coupled regime will result in the formation of a roll.

In this chapter we derive an analytical expression for this solution and examine its stability, but first we discuss the homogeneous solution and examine its stability for a flat and Gaussian pumping regime. In these discussion, it is assumed that $\delta_p = \delta_e$ to simplify certain equations, however this assumption does not significantly impact the generality of the results.

3.1 The Strong Coupling Regime

In this section, we consider the dynamics in the strong coupling regime, where we note [48, 75, 108] that the condition $\Omega_R > (\gamma_e - \gamma_{ph})/2$ must be satisfied. When one is working outside this regime, the system is only weakly coupled.

To begin the discussion of the strong coupling regime, we start from the time independent form of equations 2.46 and 2.47 and substitute $E = Ae^{ik_p x}$ and $\psi = Be^{ik_p x}$ to obtain

$$\begin{aligned} \left(ik_p^2 + \gamma_{ph} - i\delta_p\right) A &= i\Omega_R B + E_p \\ \left(\gamma_e - i\delta_p + i|B|^2\right) B &= i\Omega_R A \end{aligned} \tag{3.1}$$

We solve the first equation for A and substitute the solution into the second equation to yield

$$\left(\gamma_e - i\delta_p + i|B|^2\right) B + \frac{\Omega_R E_p + i\Omega_R^2 B}{\delta_p - k_p^2 + i\gamma_{ph}} = 0 \tag{3.2}$$

which we solve for E_p and multiply by the complex conjugate to find

$$\begin{aligned} |E_p|^2 &= a_1|B|^2 + a_2|B|^4 + |B|^6 \\ a_1 &= 2\left(\gamma_e\gamma_{ph} + \delta_p k_p^2 - \delta_p^2\right) + \Omega_R^2 + \frac{1}{\Omega_R}\left(\delta_p^2 + \gamma_e^2\right)\left((k_p^2 - \delta_p)^2 + \gamma_e^2\right) \\ a_2 &= 2(\delta_p - k_p^2) - 2\delta_p\left((k_p^2 - \delta_p)^2 + \gamma_{ph}^2\right) \end{aligned} \tag{3.3}$$

Plotting E_p allows one to observe that a regime exists where multiple solutions for $|B|^2$ are present, as can be seen in figure 3-1. Now, we differentiate this

equation and set the derivative equal to zero and thereby determine the bistability condition

$$|B_{\pm}|^2 = \frac{1}{6}\left(-2a_2 \pm \sqrt{4a_2^2 - 12a_1}\right) \tag{3.4}$$

for the upper $(+)$ and lower $(-)$ branches respectively and through which it is seen that the bistability domains are determined by the relations

$$a_2 < 0 \ , \quad a_1 > 0 \ , \quad 4a_2^2 > 12a_1 \tag{3.5}$$

which in the limit $\gamma_e = \gamma_{ph} = 0$ at $k_p = 0$, this condition becomes

$$\delta_p^2 < \Omega_R^2 \tag{3.6}$$

Through this condition, it is seen that bistability occurs away from the boundary of the existence domain along the lower branch, as determined by the dispersion relation, whilst the system is pumped at a momentum and detuning above the inflection point.

We now consider perturbing the solution by a small quantity possessed of a variable momentum in order to determine the stability of the homogeneous solution. Our expressions for E and ψ become $E = (A + \epsilon_1)e^{ik_p x}$ and $\psi = (B + \epsilon_2)e^{ik_p x}$ [167] where

$$\begin{aligned} \epsilon_1 &= a_+ e^{i\vec{\kappa}\cdot\vec{x}+\lambda t} + a_-^* e^{-i\vec{\kappa}\cdot\vec{x}+\lambda^* t} \\ \epsilon_2 &= b_+ e^{i\vec{\kappa}\cdot\vec{x}+\lambda t} + b_-^* e^{-i\vec{\kappa}\cdot\vec{x}+\lambda^* t} \end{aligned} \tag{3.7}$$

which we substitute into the initial system of equations 2.47, and neglect terms that are nonlinear in $a,\ b$ in the reference frame connected with the pump to arrive at an eigenvalue problem which can be expressed as

$$(\lambda)\vec{a} = (\hat{M} - \hat{P})\vec{a} \tag{3.8}$$

with

$$\begin{aligned}
\hat{M} &= \begin{pmatrix} |\vec{k}_i|^2 - \delta_p & -\Omega_R & 0 & 0 \\ -\Omega_R & -\delta_p & 0 & 0 \\ 0 & 0 & -|\vec{k}_s|^2 + \delta_p & \Omega_R \\ 0 & 0 & \Omega_R & \delta_p \end{pmatrix} \\
\hat{P} &= \begin{pmatrix} i\gamma_{ph} & 0 & 0 & 0 \\ 0 & i\gamma_e - 2|\Psi_0|^2 & 0 & -\Psi_0^2 \\ 0 & 0 & i\gamma_{ph} & 0 \\ 0 & (\Psi_0^2)^* & 0 & i\gamma_e + 2|\Psi_0|^2 \end{pmatrix}
\end{aligned} \tag{3.9}$$

where we let $k_p - k_x = \vec{k}_s = \vec{k}_p - \vec{\kappa}$ and $k_p + k_x = \vec{k}_i = \vec{k}_p + \vec{\kappa}$. Now, we initially solve the system where damping and nonlinearity are negligible, where we obtain the eigenvectors

$$\begin{aligned}
\vec{\alpha}^{(\pm)} &= \begin{pmatrix} -\omega_i^{(\pm)} & 1 & 0 & 0 \end{pmatrix}^T \\
\vec{\beta}^{(\pm)} &= \begin{pmatrix} 0 & 0 & -\omega_s^{(\pm)} & 1 \end{pmatrix}^T
\end{aligned} \tag{3.10}$$

with the corresponding eigenvalues

$$\lambda_\alpha = -\delta_p + \omega_i^{(\pm)}, \quad \lambda_\beta = \delta_p - \omega_s^{(\pm)} \tag{3.11}$$

for

$$\omega_{i,s}^{(\pm)} = \omega^{(\pm)}(\vec{k}_{s,i}) \tag{3.12}$$

where $\omega^{(\pm)}$ is the spectrum of linear polaritons for the upper and lower branches. From the structure of the matrix $\hat{M}$, it is evident that there exists a symmetry relation between the eigenvalues

$$\lambda_\beta(\vec{\kappa}) = -\lambda_\alpha(-\vec{\kappa}) \tag{3.13}$$

which re-expresses the energy conservation condition as $2\delta_p = \delta_s + \delta_i$. Now working in the basis of matrix $\hat{M}$ where we can express the solution

$$\vec{a}_B = \sum_{i=\alpha,\beta} \left[c_i^{(+)}(t)\vec{j}^{(+)} + c_i^{(-)}(t)\vec{j}^{(-)} \right] \tag{3.14}$$

We use this to expand the solution of the full nonlinear system in terms of the coefficients $c_i^{\pm}$

$$\begin{aligned} i\partial_t c_\alpha^{(\pm)} &= c_\alpha^{(\pm)} \left\{ -\delta_p + \omega_i^{(\pm)} + \frac{2|\Psi_0|^2}{|\vec{\alpha}^{(\pm)}|^2} - i\left[\bar{\gamma} + \gamma_d \epsilon_\alpha^{(\pm)}\right] \right\} \\ &+ c_\alpha^{(\mp)} \left\{ \frac{2|\Psi_0|^2}{|\vec{\alpha}^{(\pm)}|^2} - i\gamma_d \frac{\alpha_1^{(\pm)}\alpha_1^{(\mp)} - 1}{|\vec{\alpha}^{(\pm)}|^2} \right\} + \Psi_0^2 \frac{c_\beta^{(\pm)} + c_\beta^{(\mp)}}{|\vec{\alpha}^{(\pm)}|^2} \end{aligned}$$

$$\begin{aligned} i\partial_t c_\beta^{(\pm)} &= c_\beta^{(\pm)} \left\{ \delta_p - \Omega_s^{(\pm)} - \frac{2|\Psi_0|^2}{|\vec{\beta}^{(\pm)}|^2} - i\left[\bar{\gamma} + \gamma_d \epsilon_\beta^{(\pm)}\right] \right\} \\ &+ c_\beta^{(\mp)} \left\{ -\frac{2|\Psi_0|^2}{|\vec{\beta}^{(\pm)}|^2} - i\gamma_d \frac{\beta_3^{(\pm)}\beta_3^{(\mp)} - 1}{|\vec{\beta}^{(\pm)}|^2} \right\} - (\Psi_0^*)^2 \frac{c_\alpha^{(\pm)} + c_\alpha^{(\mp)}}{|\vec{\beta}^{(\pm)}|^2} \end{aligned} \tag{3.15}$$

where

$$\begin{array}{cc} \bar{\gamma} = \frac{\gamma_{ph}+\gamma_e}{2} & \gamma_d = \frac{\gamma_{ph}-\gamma_e}{2} \\ \epsilon_\alpha^{(\pm)} = [(\alpha_1^{(\pm)})^2 - 1]/|\vec{\alpha}^{(\pm)}|^2 & \epsilon_\beta^{(\pm)} = [(\beta_3^{(\pm)})^2 - 1]/|\vec{\beta}^{(\pm)}|^2 \end{array} \tag{3.16}$$

with $\alpha_k,\ \beta_k$ expressing the corresponding components of the (real) vectors $\vec{\alpha}$ and $\vec{\beta}$. When the pump frequency is in resonance with the lower polariton branch, we can neglect couplings between $c_{\alpha,\beta}^{(+)}$ and $c_{\alpha,\beta}^{(-)}$ provided that the separation between the upper and lower branches is large in the signal and idler regions as expressed through

$$\begin{aligned} |\Omega_i^{(+)} - \Omega_i^{(-)}| &\gg |\Psi_0|^2/|\vec{\alpha}^{(\pm)}|^2, |\Psi_0|^2/|\vec{\beta}^{(\pm)}|^2 \\ |\Omega_s^{(+)} - \Omega_s^{(-)}| &\gg |\Psi_0|^2/|\vec{\alpha}^{(\pm)}|^2, |\Psi_0|^2/|\vec{\beta}^{(\pm)}|^2 \end{aligned} \tag{3.17}$$

Now, one makes the assumption that $c_i(t) \sim e^{-i\lambda t}$ to obtain the spectrum

$$\lambda = \frac{\tilde{\Omega}_i - \tilde{\Omega}_s - i\left[2\bar{\gamma} + \gamma_d(\epsilon_\alpha + \epsilon_\beta)\right]}{2}$$

$$\pm \sqrt{\frac{\left[\tilde{\Omega}_i + \tilde{\Omega}_s - 2\delta_p + i\gamma_d(\epsilon_\beta - \epsilon_\alpha)\right]^2}{4} - \frac{|\Psi_0|^4}{\alpha^2\beta^2}} \tag{3.18}$$

with

$$\begin{array}{ccc} \bar{\gamma} = \frac{\gamma_{ph}+\gamma_e}{2} & \gamma_d = \frac{\gamma_{ph}-\gamma_e}{2} & \epsilon_\alpha = (\Omega_i^2 - 1)/\alpha^2 \\ \epsilon_\beta = (\Omega_s^2 - 1)/\beta^2 & \tilde{\Omega}_i = \Omega_i + 2|\Psi_0|^2/\alpha^2 & \tilde{\Omega}_s = \Omega_s + 2|\Psi_0|^2/\beta^2 \\ & \alpha^2 = 1 + \Omega_i^2 & \beta^2 = 1 + \Omega_s^2 \\ & \Omega_i(\vec{\kappa}) = \Omega(\vec{k}_p + \vec{\kappa}) & \Omega_s(\vec{\kappa}) = \Omega(\vec{k}_p - \vec{\kappa}) \end{array} \tag{3.19}$$

and for convenience, we have dropped the superscripts $(\pm)$. In the case where $\gamma_e = \gamma_{ph}$, the domain of unstable perturbations is given by

$$\frac{\left[\tilde{\Omega}_i + \tilde{\Omega}_s - 2\delta_p\right]^2}{4} - \frac{|\Psi_0|^4}{\alpha^2\beta^2} + \bar{\gamma}^2 < 0 \tag{3.20}$$

Any eigenvalue with $\gamma_l = Im(\lambda) > 0$ will correspond to an unstable exponentially growing perturbation. Additionally, we note that the real part of these eigenvalues corresponds to the frequency of a perturbation with momentum (κ_x, κ_y). We will utilize this fact within later chapters to calculate the associated velocity. Now, by plotting the imaginary component on the $\kappa_x - \kappa_y$ plane, it is observed that in the momentum space distribution of the evolving system, signal and idler bands exist around $\kappa_x = 0$ and $\kappa_x = 2k_p$ respectively, as can be seen in figure 3-1. In this figure, we highlight that these spots are only approximately circular, such that there is no axis of symmetry about the maximum of either instability growth rates. This asymmetry plays an important role in the dynamics of vortex lattices within the system, as we will observe in chapter 4.

Scanning across the $\delta_p - k$ plane provides details of the instability over the lower polariton branch, by charting the maximal growth rate within the $k_x - k_y$ plane, and shows that as one moves towards the resonance at zero momentum, the region of instability on the lower bistability branch is seen to increase, while far from the first inflection point on the bistability branch, whilst approaching from below, it is observed that the solutions are stable. This line serves to display the onset of a parametric stability regime. Above which, the signal and idler sidebands are observed to grow, as displayed in figure 3-1 for the lower and upper bistability branches.

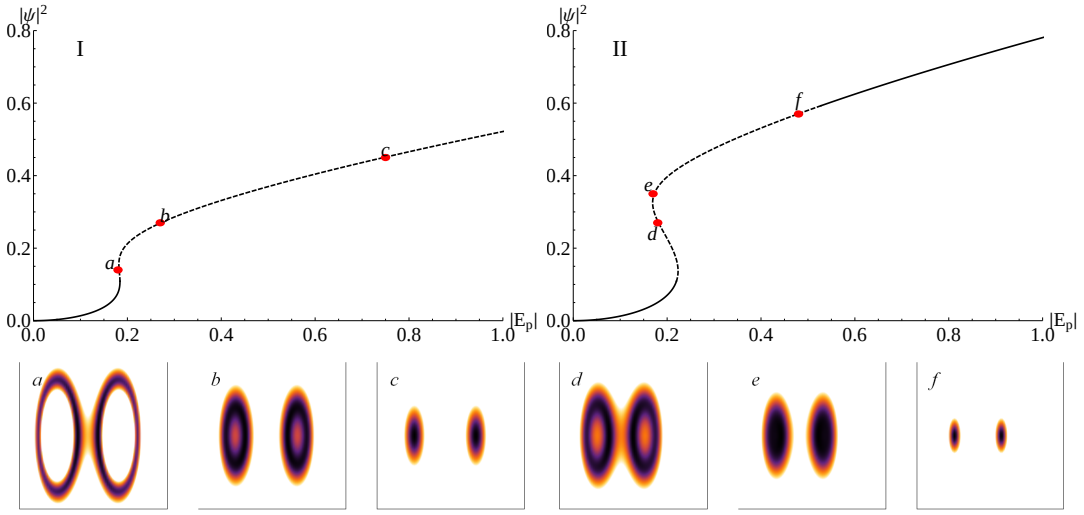

Figure 3-1: *Plot of $|\psi_p|^2$, as a function of $|E_p|$, displaying the bistability domain where the dashed line denotes the unstable regimes at $\delta_p = -0.05$ for $k_p = 2$ (I) and $k_p = \pi/2$(II). The panels (a-f) display the form of the instability domains across the (k_x, k_y) plane, where only regions with $Im(\lambda) > 0$ are displayed.*

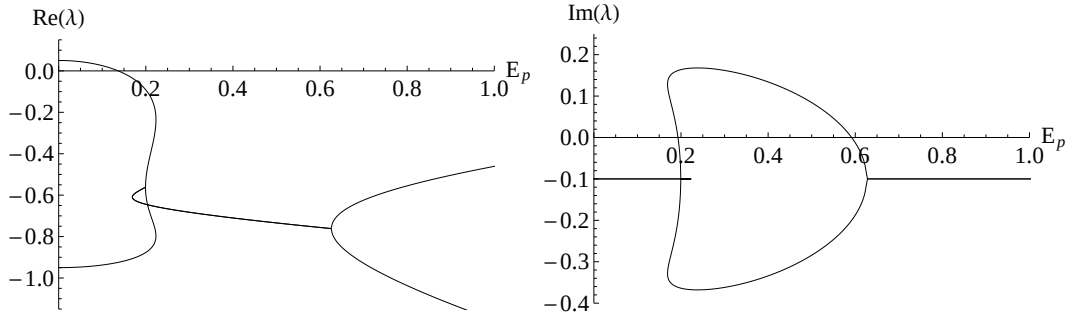

Figure 3-2: *(Left) Plot of frequency, $Re(\lambda)$ against $|E_p|$. (Right) Plot of Instability growth rate, $Im(\lambda)$ against $|E_p|$ at $\gamma_{ph} = \gamma_e = 0.1$, and $\delta_p = -0.05$ with a pump momentum, $k_p = \pi/2$ and a signal momentum, $k_s = 0$.*

Upon the lower branch, it is observed that the emergent instability initially possesses a "figure of eight form", which separates into two open circles centered at approximately $k_p \pm k_p$. On the upper branch, one can see that parametric instability is present, taking the form of closed circles centered upon the same locations in the $k_x - k_y$ plane. This is seen in the lower panels of figure 3-1, where it is seen to agree with previous work in the area [166, 91, 25]. When instability is present, it is observed that the frequency of the signal component decreases with increasing pump intensity, as illustrated in figure 3-2 for a signal momentum, $k_s = 0$ while there is a corresponding shift in the idler frequency to satisfy energy conservation. At this point, it is important to note that these curves are associated with only two of the eigenvalues of equation 3.8 that correspond to the lower branch, whilst the remaining eigenvalues are associated with upper branch of the homogeneous solution. Specifically in the bistable region, there exist three solutions associated with each of the lower branch eigenvalues. When the solution is unstable, the real components of these will coincide, whilst the imaginary components will separate. At this point we also noted that $d\delta/\dot{\mathrm{k}}_x \neq 0$ and $d\delta/\dot{\mathrm{k}}_y \neq 0$ in the instability regions such that there will be a drift of perturbations within these regions in the direction of the pump. This will play a significant role in the later sections, as will the points where the imaginary values diverge. These will be determined later in our discussion of the roll solutions in a later section, while we will discuss the effects of the non-flat dispersion when we examine the drift velocity of vortex lattices.

In momentum space, there exist two distinct stability regimes, which take the form of closed and open circles, centered at $\kappa = 0$, $\kappa = 2k_p$, where agreement between the analytical plots and numerical evaluations is observed over the entire range of $\delta_p - k_p$ values. The existence of these two forms strongly depends upon the momentum of the pump. When the solution is bistable, the open circle growth regions exist solely between the upper and lower bistability curves and are inaccessible, whilst closer to the linear regime whilst the system is monostable, one can access this additional regime. At high pump intensities, there exists an upper boundary to the unstable region, which is approached through "spot-like instabilities" within momentum space. These spots are asymmetric about their maximum instability growth rates. These maxima which are seen to move along the κ_x axis as one varies either the pump strength or the position on the $\delta_p - k_p$ plane. Initially, increasing the pump strength is seen to result in growth of the spot size, far above the bistable region, the effect is seen to reverse. This variation

of spot radius serves to provide an indication of the maximum noise allowable on the probe, or similarly the maximum angle permitted on the probe beam possessing a known momentum distribution.

By recording the maximum instability growth rate over the entire $k_p - \delta_p$ plane across the entire energy spectrum, it is observed that there exist two regions of instability upon the lower polariton branch. Only the region that is located above the inflection point is parametrically unstable, whilst the remaining instability region takes the form of an open or closed circle centered about the pump momentum.

3.2 Strong coupling in the presence of a Gaussian pump

Now we return to the initial system, but the pump has a Gaussian profile rather than a uniform one, such that the system is

$$\begin{aligned} \frac{d}{dt}E - i\nabla^2 E + (\gamma_{ph} - i\delta_p)E &= i\Omega_R\psi + E_p e^{ik_p\cdot x - \frac{(x^2+y^2)}{2W^2}} \\ \frac{d}{dt}\psi + \left(\gamma_e - i\delta_p + i|\psi|^2\right)\psi &= i\Omega_R E \end{aligned} \tag{3.21}$$

for a pump with standard deviation, W. Now, we determine the form of the solution through a Newton method (see appendix A.1), which allows one to determine that the maximum value of the fields corresponds to that for the homogeneous system at the chosen pump strength, as noted in the main panel of figure 3-4. In the absence of bistability or along the lower bistability branch, it is seen that the solutions have a similar form as that of the pump, but are significantly narrower and no longer Gaussian as can be observed in figure 3-3. The form of solutions along the upper bistability branch are significantly different, however as denoted through the dotted line, wherein it is seen that they are largely contained within a width of approximately one standard deviation of the pump $W = W_{pump}$, where the pump intensity is close to that at the turning point of upper branch in the homogeneous solution.

As in the case of a flat pump, one can determine the stability of the one dimensional system in the same manner as discussed previously through the solution to the eigenvalue equation

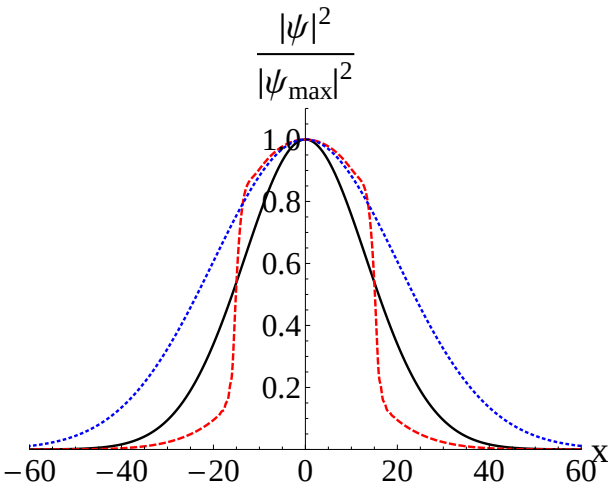

Figure 3-3: *Plot of a normalized $|\psi_p|^2$, along the x-axis, where $k_p = 2$, $\delta_p = -0.05$, $\gamma_{ph} = \gamma_e = 0.1$ and $W = 20$ for $E_p = 0.10$ (black) and $E_p = 0.20$ (red, dashed), lying on either side of the bistable region. The blue, dotted line illustrates the form of the Gaussian pump.*

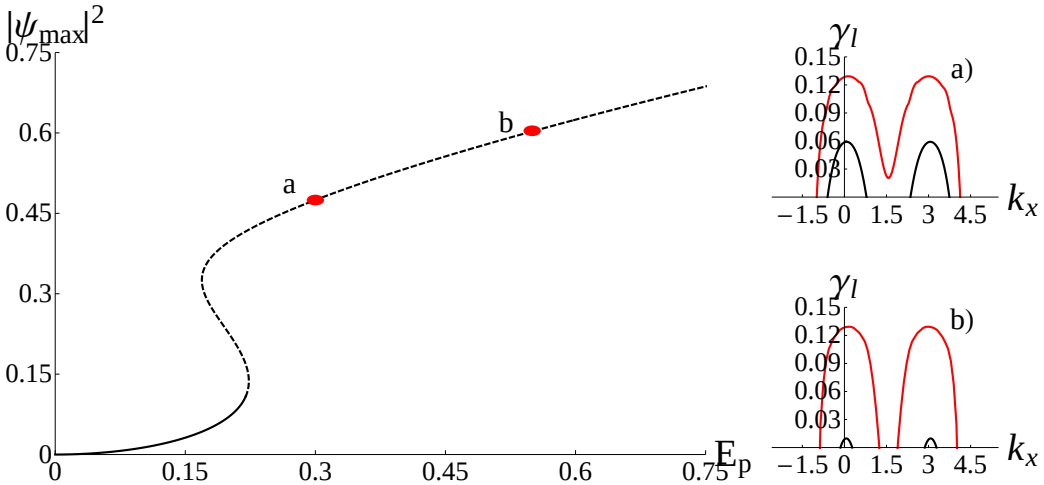

Figure 3-4: *Plot of $|\psi_p|^2$, against pump strength, E_p for $k_p = \pi/2$, $\delta_p = -0.05$ and $\gamma_{ph} = \gamma_e = 0.1$ displaying the maximum amplitude of the system. The solid (dashed) line corresponds to a Gaussian pump of width $W = 50$, for the stable (unstable) solution. The pump strength in panel (a) $E_p = 0.30$, and (b) $E_p = 0.55$, wherein one can see the associated momentum space plots.*

$$\lambda \begin{pmatrix} a_+ \\ a_- \\ b_+ \\ b_- \end{pmatrix} = \begin{pmatrix} -L_+ & 0 & -\Omega_R & 0 \\ 0 & L_-^* & 0 & \Omega_R \\ -\Omega_R & 0 & -Q & BB \\ 0 & \Omega_R & -B^*B^* & Q^* \end{pmatrix} \cdot \begin{pmatrix} a_+ \\ a_- \\ b_+ \\ b_- \end{pmatrix} \tag{3.22}$$

where

$$\begin{aligned} L_\pm &= -\frac{d^2}{dx^2} + 2i(k_p \pm \kappa_x)\frac{d}{dx} - (k_p \pm \kappa_x)^2 + \delta_p + i\gamma_{ph} \\ Q &= \delta_p - 2|B|^2 + i\gamma_e \end{aligned} \tag{3.23}$$

When bistability is absent, the system is always stable, as is also the case for solutions along the lower bistability branch, just as for the homogeneous solutions.

Whilst it is unstable, a roll with a period equal to the pump momentum modulates the solution. This roll emerges from the leading edge of the stationary pattern. As one observes the initially Gaussian pattern evolve, the leading edge of this pattern is seen to shift to increasingly longer wavelengths, whilst the trailing edge becomes increasingly red-shifted.

3.3 Roll solutions in the strong coupling regime

In section 3.1, we determined that well separated signal, pump and idler regions exist within momentum space for strong coupled solutions. This allows us to determine the existence domain and character of roll solutions within this regime. We begin by expanding the E and ψ-fields about the momenta $k = k_s$, k_p and k_i to yield

$$E = A_p e^{ik_p x - i\delta_p t} + A_s e^{ik_s x - i\delta_s t} + A_i e^{ik_i x - i\delta_i t} \tag{3.24}$$

$$\psi = \psi_p e^{ik_p x - i\delta_p t} + \psi_s e^{ik_s x - i\delta_s t} + \psi_i e^{ik_i x - i\delta_i t} \tag{3.25}$$

which we substitute into the initial system as reproduced below

$$\begin{aligned} \frac{d}{dt}E &- i\nabla^2 E + (\gamma_{ph} - i\delta_p)\, E = i\Omega_R \psi + E_p e^{ik_p x} \\ \frac{d}{dt}\psi &+ \left(\gamma_e - i\delta_p + i|\psi|^2\right)\psi = i\Omega_R E \end{aligned} \tag{3.26}$$

Using the exciton equation and neglecting the terms with momentum $k_x \neq k_s$, $k_x \neq k_p$ or $k_x \neq k_i$, thus we have

$$0 = (\alpha_s + |\psi_s|^2 + 2|\psi_p|^2 + 2|\psi_i|^2)\psi_s + \psi_p^2\psi_i^* \tag{3.27}$$

$$0 = (\alpha_i + |\psi_i|^2 + 2|\psi_p|^2 + 2|\psi_s|^2)\psi_i + \psi_p^2\psi_s^* \tag{3.28}$$

$$0 = (\alpha_p + |\psi_p|^2 + 2|\psi_s|^2 + 2|\psi_i|^2)\psi_p + 2\psi_s\psi_i\psi_p^* - \beta E_p \tag{3.29}$$

where we let

$$\begin{aligned} \beta &\equiv \frac{\Omega_R}{k_p^2 - \delta_p - i\gamma_{ph}} \\ \alpha_{s,p,i} &\equiv -\delta_{s,p,i} - i\gamma_e - \frac{\Omega_R^2}{k_{s,p,i}^2 - \delta_{s,p,i} - i\gamma_{ph}} \end{aligned} \tag{3.30}$$

We assume that signal and idler fields are small, such that terms which are nonlinear in these fields are negligible and thus

$$\begin{aligned} 0 &= (\alpha_s + 2|\psi_p|^2)\psi_s + \psi_p^2\psi_i^* \\ 0 &= (\alpha_i + 2|\psi_p|^2)\psi_i + \psi_p^2\psi_s^* \end{aligned} \tag{3.31}$$

The above equations have to be satisfied at the boundary of the parametric instability, where the spontaneously generated signal and idler polaritons are neither amplified nor damped, and we note that the equations are symmetric under the transformation $\psi_s, \psi_i \to \psi_s e^{-i\phi}, \psi_i e^{i\phi}$. Now, the solvability conditions for these two equations is

$$\begin{aligned} f + 3|\psi_p|^4 + 2g|\psi_p|^2 &= 0 \\ f \equiv \alpha_s\alpha_i^*, \quad g &\equiv \alpha_s + \alpha_i^* \end{aligned} \tag{3.32}$$

We separate the real and imaginary parts to arrive at

$$|\psi_p|^2 = -\frac{f_i}{2g_i}, \; f = f_i + if_r, \; g = g_i + ig_r$$

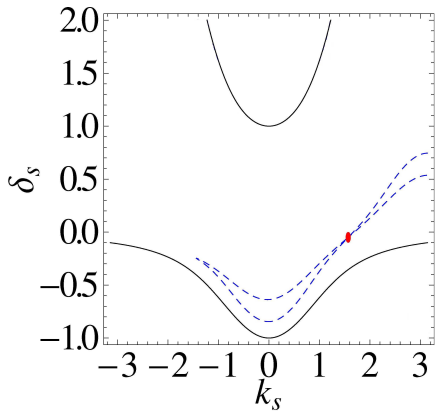

Figure 3-5: *Plot of signal frequency, δ_s, against signal momentum, k_s for $\delta_p = -0.05$, $k_p = \pi/2$ and $\gamma_{ph} = \gamma_e = 0.1$, displaying the boundaries of the instability region (dashed line).*

$$0 \quad = \quad D(k_s, \delta_s) \equiv 4g_i^2 f_r + 3f_i^2 - 4g_i f_i g_r \tag{3.33}$$

We require that the solution is neutrally stable and thus $D = 0$ and utilize the energy and momentum conservation through the relations $2\delta_p = \delta_s + \delta_i$ and $2k_p = k_s + k_i$ at a given pump momentum and detuning. These requirements provides existence domains for roll solutions over the $(k_s,\ \delta_s)$ plane, where one can see these curves of neutral stability in figure 3-5. These curves show that for each value of k_s, a range of possible signal frequencies are supported at a currently undetermined intensity for a pump with momentum and frequency on the lower polariton branch. At a given signal momentum, the uppermost curve corresponds to the pump intensity where the system first becomes unstable, whilst the lower curve is associated with the pump intensity where the system returns to stability, as noted earlier in figure 3-2.

Now, we need to account for all the neglected nonlinear terms to allow one to find stationary amplitudes of the signal and idler waves that emerge from neutrally stable points. To achieve this, we utilize the structure of parametric interactions which allows one to make the symmetry transformation, $\psi_{s,i,p} = |\psi_{s,i,p}|e^{i\phi_{s,i,p}}$. Next, we separate their real and imaginary parts through the equations for signal and idler to yield four real equations for three unknowns $|\psi_s|$, $|\psi_i|$ and $\Delta = 2\phi_p - \phi_s - \phi_i$. These equations are

$$\begin{aligned}
|\psi_i||\psi_p|^2 + \cos\Delta|\psi_s|\left(|\psi_s|^2 + 2|\psi_p|^2 + 2|\psi_i|^2 + \Re[\alpha_s]\right) &= 0 \\
|\psi_s||\psi_p|^2 + \cos\Delta|\psi_i|\left(2|\psi_s|^2 + 2|\psi_p|^2 + |\psi_i|^2 + \Re[\alpha_i]\right) &= 0 \\
-\sin\Delta|\psi_s|\Im[\alpha_s] + |\psi_p|^2|\psi_i| &= 0 \\
\sin\Delta|\psi_i|\Im[\alpha_i] + |\psi_p|^2|\psi_s| &= 0
\end{aligned} \tag{3.34}$$

which retain the symmetry of equation 3.31 under the transformation $\psi_s, \psi_i \to \psi_s e^{-i\phi}, \psi_i e^{i\phi}$. From these, it follows that the densities of excitons in the signal and idler components can be expressed as

$$\begin{aligned}
|\psi_i|^2 &= \frac{\Im(\alpha_s)}{\Im(\alpha_i)}|\psi_s|^2 = \kappa|\psi_s|^2 \\
|\psi_s|^2 &= \frac{\Re(\alpha_s) - \Re(\alpha_i)\kappa + 2|\psi_p|^2(1-\kappa)}{\kappa^2 - 1}
\end{aligned} \tag{3.35}$$

Whilst the equation for ψ_p is arrived at by multiplying equation 3.29 by its conjugate to provide

$$\begin{aligned}
|\beta|^2|E_p|^2 &= |\psi_p|^2|\alpha_p + |\psi_p|^2 + 2|\psi_s|^2 + 2|\psi_i|^2 \\
&- \frac{2|\psi_s|^2|\psi_p|^2}{\alpha_i + |\psi_i|^2 + 2|\psi_s|^2 + 2|\psi_p|^2}|^2
\end{aligned} \tag{3.36}$$

Now, we solve the system 3.34 for $\cos\Delta$ and $\sin\Delta$ providing

$$\begin{aligned}
\cos^2\Delta &= \frac{\kappa(\Re(\alpha_s) - \Re(\alpha_i) + |\psi_s|^2(\kappa-1))^2}{|\psi_p|^4(1-\kappa)^2} \\
\sin^2\Delta &= \frac{\Im(\alpha_s)\Im(\alpha_i)}{|\psi_p|^4}
\end{aligned} \tag{3.37}$$

where $\Delta = 2\arg(\psi_p) - \arg(\psi_s) - \arg(\psi_i)$. From the relation $\sin^2\Delta + \cos^2\Delta = 1$, one obtains a quadratic equation in $|\psi_p|^2$,

$$\begin{aligned}
0 &= a|\psi_p|^4 + b|\psi_p|^2 + c \\
a &= -(1-\kappa)^4 \\
b &= 4\kappa(1-\kappa)[2(\Re(\alpha_s) - \Re(\alpha_i)\kappa) + \Re(\alpha_s)\kappa - \Re(\alpha_i)] \\
c &= \kappa[2(\Re(\alpha_s) - \kappa\Re(\alpha_i)) + \Re(\alpha_s)\kappa - \Re(\alpha_i)]^2 + \Im(\alpha_s)\Im(\alpha_i)(1-\kappa^2)^2
\end{aligned} \tag{3.38}$$

We fix k_p and δ_p and scan over δ_s to obtain the solution set $|\psi_p|(\delta_s, k_s)$ and substitute this solution set back into equation 3.36 to obtain $E_p(\delta_s, k_s)$. From these two solution sets, it is simple to obtain $E_p(|\psi_p|)$ and arrive at the three amplitudes, $|\psi_{s,p,i}|$. From the phase symmetry previously discussed, one can assume $\arg(\psi_s) = 0$, and thus $\arg(\psi_i) = 2\arg(\psi_p) - \omega$, which we use in conjunction with equation 3.29 to obtain the equation for $\arg(\psi_p)$

$$\frac{1}{|\psi_p|}\frac{iE_p e^{-i\arg(\psi_p)}}{\delta_p + i\gamma_{ph} - k_p^2} = \alpha_p + |\psi_p|^2 + 2|\psi_s|^2 + 2|\psi_i|^2 + 2|\psi_s||\psi_i|e^{-i\omega} \tag{3.39}$$

Through which, we have determined the range of pump intensities associated with the neutral stability curves governed by equation 3.33. This allows us to determine the curve associated with the roll which can be observed in figure 3-6 for different values of the signal momentum. It is seen that as one varies k_s both the start and end points of the roll branch move. As the signal and idler momentum are moved towards the position of maximum instability, the extent of the roll branch is seen to increase and it is self-evident that when the excitation at k_s is outside the instability regime of the homogeneous solution, there will be no excitation of a roll.

These equations also provide the phase of the pump, signal and idler components, which are vital in the determination of the stability, which we now proceed to examine. For this, we return to the initial system

$$\begin{aligned} \frac{d}{dt}E &- i\nabla^2 E + (\gamma_{ph} - i\delta_p)\, E = i\Omega_R\psi + E_p e^{ik_p x} \\ \frac{d}{dt}\psi &+ \left(\gamma_e - i\delta_p + i|\psi|^2\right)\psi = i\Omega_R E \end{aligned} \tag{3.40}$$

and take the ansatz

$$\begin{aligned} E &= A_p(x,y)e^{ik_p x - i\delta_p t} + A_s(x,y)e^{ik_s x - i\delta_s t} + A_i(x,y)e^{ik_i x - i\delta_i t} \\ \psi &= \psi_p(x,y)e^{ik_p x - i\delta_p t} + \psi_s(x,y)e^{ik_s x - i\delta_s t} + \psi_i(x,y)e^{ik_i x - i\delta_i t} \end{aligned} \tag{3.41}$$

where

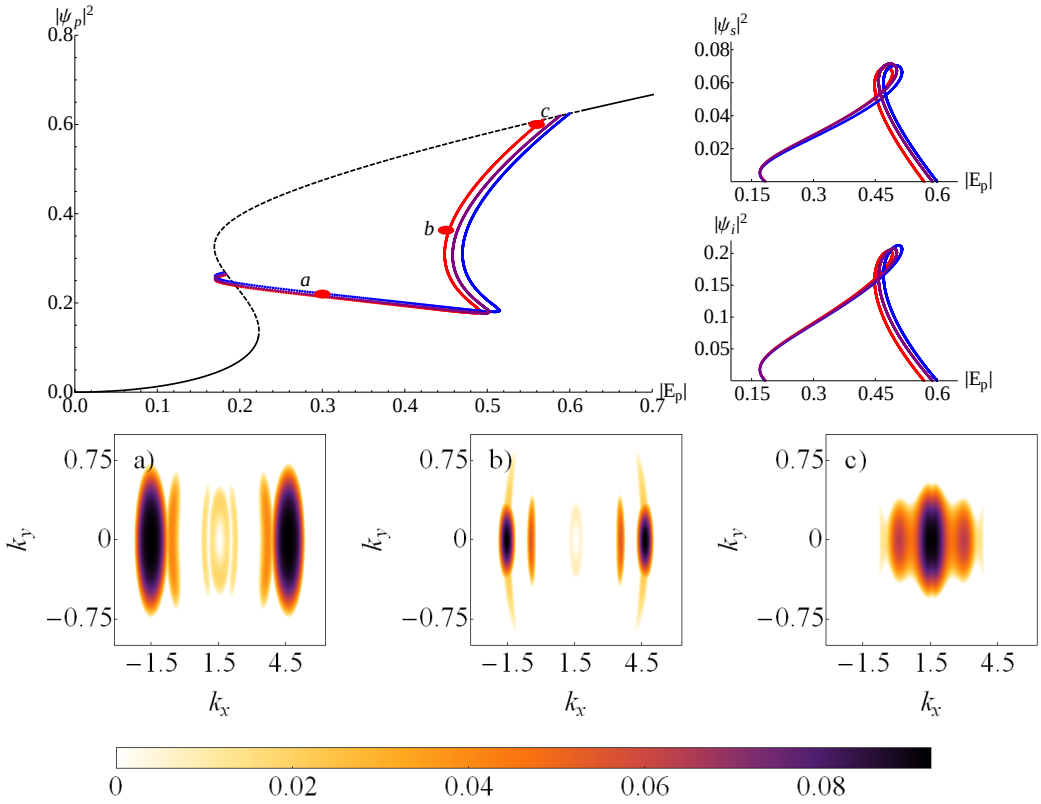

Figure 3-6: *Plot of the exciton number against pump strength for* $k_p = \pi/2$, $\delta_p = -0.05$ *and* $\gamma_e = \gamma_{ph} = 0.1$ *for the pump, signal and idler. The homogeneous solutions are shown in black. Roll solutions are seen at* $k_s = 0.0$*(red),* $k_s = -0.14$*(blue) and* $k_s = 0.21$*(purple) where one can see the momentum space instability domains at (a)* $E_p = 0.30$*, (b)* $E_p = 0.45$ *and (c)* $E_p = 0.56$*, for* $k_s = 0.0$*.*

$$\begin{aligned} A_{p,s,i}(x,y) \to A_{p,s,i}(x,y) &+ \epsilon_{p,s,i+} e^{i\vec{\kappa}\cdot\vec{x}+\lambda t} + \epsilon_{p,s,i-} e^{-i\vec{\kappa}\cdot\vec{x}+\lambda^* t} \\ \psi_{p,s,i}(x,y) \to \psi_{p,s,i}(x,y) &+ \epsilon_{p,s,i+} e^{i\vec{\kappa}\cdot\vec{x}+\lambda t} + \epsilon_{p,s,i-} e^{-i\vec{\kappa}\cdot\vec{x}+\lambda^* t} \end{aligned} \tag{3.42}$$

Additionally, we assume that the perturbation is sufficiently small to allow one to neglect terms of order $O(\epsilon^2)$. This provides the eigenvalue equation

$$\lambda|\epsilon\rangle = -\begin{pmatrix} T_1 & T_2 \\ T_2 & T_3 \end{pmatrix}|\epsilon\rangle \tag{3.43}$$

where

$$\hat{T}_1 = \begin{pmatrix} i\left(k_s+\kappa_x\right)^2 + i\kappa_y^2 + \gamma_{ph} - i\delta_s \\ i\left(k_p+\kappa_x\right)^2 + i\kappa_y^2 + \gamma_{ph} - i\delta_p \\ i\left(k_i+\kappa_x\right)^2 + i\kappa_y^2 + \gamma_{ph} - i\delta_i \\ -i\left(k_s-\kappa_x\right)^2 - i\kappa_y^2 + \gamma_{ph} + i\delta_s \\ -i\left(k_p-\kappa_x\right)^2 - i\kappa_y^2 + \gamma_{ph} + i\delta_p \\ -i\left(k_i-\kappa_x\right)^2 - i\kappa_y^2 + \gamma_{ph} + i\delta_i \end{pmatrix}^T \cdot I_6$$

$$\hat{T}_2 = i\Omega_R \begin{pmatrix} -1 & -1 & -1 & 1 & 1 & 1 \end{pmatrix} \cdot I_6$$

$$\hat{T}_3 = \begin{pmatrix} Q_s^- & 2iP & 2i\psi_i^*\psi_s & i\psi_s^2 & 2i\psi_p\psi_s & iR \\ iP^* & Q_p^- & iP & 2i\psi_p\psi_s & iR & 2i\psi_i\psi_p \\ 2i\psi_i\psi_s^* & 2iP^* & Q_i^- & iR & 2i\psi_i\psi_p & i\psi_i^2 \\ -i\psi_s^*\psi_s^* & -2i\psi_p^*\psi_s^* & -iR^* & Q_s^+ & -2iP^* & 2i\psi_i\psi_s^* \\ -2i\psi_p^*\psi_s^* & -iR^* & -2i\psi_i^*\psi_p^* & -iP & Q_p^+ & -iP^* \\ -iR^* & -2i\psi_i^*\psi_p^* & -i\psi_i^*\psi_i^* & -2i\psi_i^*\psi_s & -2iP & Q_i^+ \end{pmatrix}$$

where

$$\begin{aligned} Q_s^\pm &= \gamma_e \pm i\left(\delta_s - 2|\psi_i|^2 - 2|\psi_p|^2 - |\psi_s|^2\right) \\ Q_p^\pm &= \gamma_e \pm i\left(\delta_p - 2\left(|\psi_i|^2 + |\psi_p|^2 + |\psi_s|^2\right)\right) \\ Q_i^\pm &= \gamma_e \pm i\left(\delta_i - |\psi_i|^2 - 2|\psi_p|^2 - 2|\psi_s|^2\right) \\ P &= \psi_i^*\psi_p + \psi_p^*\psi_s \\ R &= \psi_p^2 + 2\psi_i\psi_s \end{aligned} \tag{3.44}$$

Through this, one can determine the stability of the roll solution, and thus obtain the instability domain over the (κ_x, κ_y) plane which can be seen in figure 3-6 for $\delta_p = -0.05$ and $k_p = \pi/2$, where the solution is weakly unstable over the entire range of existence for the roll solution.

One can solve the eigenvalue equation to determine the eigenvector, ϵ which one can observe in figure 3-7(b), where it is seen that this instability is dominated by a wave with a period that is one third of that for the roll solution, and thus is associated with the regions about $k = k_p \pm 2k_p$. Since the maxima of the instabilities for roll solutions remain located along the pump axis, it is clear that these instabilities will develop in a similar manner as those associated with the homogenoeus solution that gave rise to the roll.

In figure 3-7(d), one observes the equivalent numerical plot, wherein it is seen that agreement exists between these two approaches. It is noted that in the signal and idler regions of momentum space, there exists only a single maximum position. It is about this growth rate that instability increases most rapidly, and the resultant pattern is dominated by the pattern associated with these values thus there can be no spontaneous generation of vortex lattices from the roll pattern is the absence of external contributions.

Additionally, we have noted earlier that the dispersion is not flat in the instability domains. This results in a drift of the roll with respect to the homogeneous solution with the pump axis.

3.4 Summary

In this chapter, we have discussed the strongly coupled system, wherein we illustrated the presence of parametric amplification for a homogeneous pumping region, through a study of the stability of the system along the lower polariton branch. From this, we examined the stability of the system under a Gaussian regime. For Gaussian pumping, it was seen that all the salient features associated with the homogeneous regime are preserved, however motion within the pump region serves to produce a roll pattern.

Finally, we derived analytical expressions for roll solutions and studied their stability. Through this, it was seen that instability in the roll solution results in the generation of a weak standing wave with momentum, $\vec{k} \approx 3\vec{k_p}$.

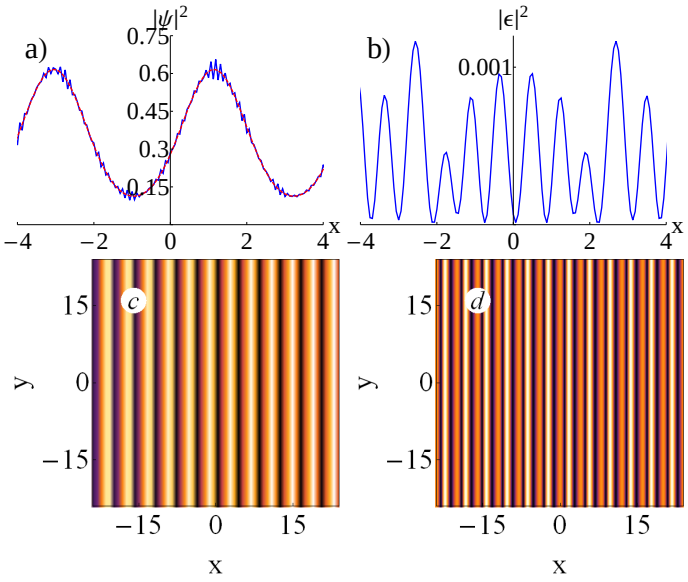

Figure 3-7: *Panel (a) shows a plot of the total ψ-field (blue) and the unperturbed roll solution (purple) along the x-axis. Panel (b) displays the form of the perturbation ϵ in the one dimensional system, wherein one can observe the period of perturbation is $3k_p$, for the parameters in figure 3-6(b), whilst panels (c) and (d) display initial roll and the resultant instability pattern in the two dimensional system, at $t = 90$.*

CHAPTER 4

Parametric Amplification of Vortices and Vortex Lattices

The presence of phase singularities, in the form of vortex solitons and vortex lattices[83], in exciton-polariton condensates has attracted significant experimental attention by Lagoudakis *et al.* [93] amongst others[104, 141, 148]. These experiments act as a means to clarify the behavior of an out of equilibrium condensate, although their observation alone is not sufficient to confirm a superfluid nature of out of equilibrium polariton condensates. These observations present an unambiguous phase shift of 2π, accompanied by a clear reduction in the polariton density about the vortex core, illustrating that vortex formation is observable in multiple regimes through the use of an external seed or in the presence of defects in the cavity, among other means. The associated theoretical models show that spontaneously arising vortices emerge as a result of the interplay between disorder and the out of equilibrium nature of the polariton condensate. Experimental observations by Sanvitto *et al.* [147] have illustrated that it is possible to form a signal vortex and idler antivortex in the optical parametric oscillator regime. Above this threshold, $m = 1$ vortices are observed to be long lived, whilst $m = 2$ vortices are observed to split.

In this chapter, we focus upon the dynamics of these polariton vortices and vortex lattice existing within a microcavity, through the model discussed in section 2.3. First, we examine the stationary system through perturbative and variational approaches to determine the expected behavior of the stationary system. Next, we investigate the dynamics of honeycomb and square vortex lattices

by deriving approximate analytical expressions for their behavior. The discussion of honeycomb vortex lattices has been published in reference [57]. As in the previous chapter, it is assumed that $\delta_p = \delta_e$ to simplify the equations.

4.1 Analytic Behavior of Conservative Systems

Generally, the profiles of vortices can only be determined numerically, however there are various analytical approaches that can provide some useful information about the conservative system. To begin, we consider the behavior in the limits $r \to 0$ and $r \to \infty$ to determine whether there exists an additional constraint upon the existence domain. Following this, we consider perturbative and variational approaches to obtain approximate solutions to the system.

In these approaches, we neglect the damping and pump terms and assume a radial parabolic potential of the form $U = -\alpha r^2$, so that the model becomes

$$-i\nabla^2 E(r,\theta) - i(\delta_p - \alpha r^2)E(r,\theta) = i\Omega_R \psi(r,\theta) \tag{4.1}$$

$$-i\delta_p \psi(r,\theta) + i|\psi(r,\theta)|^2 \psi(r,\theta) = i\Omega_R E(r,\theta) \tag{4.2}$$

where as previously, Ω_R is the Rabi frequency, δ_p denotes the detuning parameter, $E(r,\theta)$ is the photon field and $\psi(r,\theta)$ is recognized as the exciton field.

4.1.1 Tail Analysis

Initially, we consider the limiting behavior for small nonlinearities in the one dimensional case. For the stationary case in the absence of a potential and at a large distance from the origin, one has

$$\begin{aligned} -\nabla^2 E - \delta_p E &= \Omega_R \psi \\ -\delta_p \psi + |\psi|^2 \psi &= \Omega_R E \end{aligned} \tag{4.3}$$

We let $\psi = \psi_\infty + \epsilon_\psi$, $E = E_\infty + \epsilon_E$, where $\epsilon_{E,\psi}$ is small. Recalling that E_∞ and ψ_∞ must themselves satisfy the system, and thus it is possible to separate these equations and obtain

$$-\delta_p E_\infty = \Omega_R \psi_\infty$$

$$(-\delta_p + |\psi_\infty|^2)\psi_\infty = \Omega_R E_\infty \tag{4.4}$$

and

$$\begin{aligned} -\nabla^2\epsilon_E - \delta_p\epsilon_E &= \epsilon_\psi \\ \epsilon_\psi^3 + 3\sqrt{\delta_p - \frac{\Omega_R^2}{\delta_p}}\epsilon_\psi^2 + \left(2\delta_p - 3\frac{\Omega_R^2}{\delta_p}\right)\epsilon_\psi &= \Omega_R\epsilon_E \end{aligned} \tag{4.5}$$

Neglecting the trivial solution, one finds

$$\psi_\infty = \pm\sqrt{\tfrac{\delta_p^2-\Omega_R^2}{\delta_p}} \quad E_\infty = -\tfrac{\Omega_R}{\delta_p}\psi_\infty \tag{4.6}$$

While the second pair allows one to obtain an expression for ϵ_ψ by neglecting quadratic and cubic terms. Substituting back into the initial system, we obtain

$$\epsilon_\psi = \frac{\Omega_R}{3|\psi_\infty|^2 - \delta_p}\epsilon_E \tag{4.7}$$

$$\epsilon_E = B_1 e^{i\sqrt{\frac{2\left(\delta_p^2-\Omega_R^2\right)}{3|\psi_\infty|^2-\delta_p}}r} + B_2 e^{-i\sqrt{\frac{2\left(\delta_p^2-\Omega_R^2\right)}{3|\psi_\infty|^2-\delta_p}}r} \tag{4.8}$$

Now as E and ψ are real, the full solutions are given as

$$E(r) = \mp\frac{\Omega_R}{\delta_p}\psi_\infty + B_1\left(e^{i\beta r} + e^{-i\beta r}\right) \tag{4.9}$$

$$\psi(r) = \pm\psi_\infty + \frac{\Omega_R}{3|\psi_\infty|^2 - \delta_p}B_1\left(e^{i\beta r} + e^{-i\beta r}\right) \tag{4.10}$$

$$\beta = \sqrt{\tfrac{2[\delta_p^2-\Omega_R^2]}{3|\psi_\infty|^2-\delta_p}} \quad \psi_\infty = \pm\sqrt{\tfrac{\delta_p^2-\Omega_R^2}{\delta_p}} \tag{4.11}$$

As $\beta \geq 0$, one has a condition on the existence of real vortex solutions that may be expressed as

$$\frac{2[\delta_p^2 - \Omega_R^2]}{3|\psi_\infty|^2 - \delta_p} \geq 0 \tag{4.12}$$

$$-\Omega_R < \delta_p < 0, \quad \sqrt{2}\delta_p > \sqrt{3}\Omega_R \tag{4.13}$$

Upon the lower polariton branch, the minimum for vortex solutions coincides with the minimum of the nonlinear domain when no potential is present, as discussed in section 2.3.

4.1.2 Perturbative Approach

Having determined that there are no restrictions placed upon the solution in the absence of a potential, we proceed with a perturbative approach following the standard technique[96], and expand the field as a function of the nonlinearity to first order

$$\begin{aligned} E &= (E_0(r) + \epsilon E_1(r,\theta))e^{im\theta} \\ \psi &= (\psi_0(r) + \epsilon\psi_1(r,\theta))e^{im\theta} \\ \delta_p &= \delta_{p,0} + \epsilon\delta_{p,1} \end{aligned} \tag{4.14}$$

where ϵ is small. We substitute these back into the system, neglecting terms of order $O(\epsilon^2)$ and separate to find

$$L \cdot |\phi_0\rangle = \begin{pmatrix} \nabla^2 + \delta_p - \alpha r^2 & \Omega_R \\ \Omega_R & \delta_p \end{pmatrix} \cdot \begin{pmatrix} E_0 \\ \psi_0 \end{pmatrix} = 0 \tag{4.15}$$

and

$$L \cdot |\phi_1\rangle = \begin{pmatrix} \delta_{p,1} & 0 \\ 0 & \delta_{p,1} - |\psi_0|^2 \end{pmatrix} \cdot |\phi_0\rangle = R \cdot |\phi_0\rangle \tag{4.16}$$

where $|\phi_1\rangle = \begin{pmatrix} E_1 & \psi_1 \end{pmatrix}^T$. We solve this system to obtain

$$\begin{aligned} E_0 &= 2^{\frac{1+m}{2}} r^m e^{-\frac{\sqrt{\alpha}r^2}{2}} L_n^m(\sqrt{\alpha}r^2) \\ L_n^m(z) &= \frac{1}{n!}\Gamma(m+n+1)\sum k \frac{(-n)_k z^k}{\Gamma(m+k+1)k!} \\ n &= -2(m+1) + \frac{\chi}{\sqrt{\alpha}} \\ \psi_0 &= -\frac{\Omega_R}{\delta_{p,0}} E_0 \end{aligned} \tag{4.17}$$

for a linearized energy $\chi = \delta_{p,0} - \frac{\Omega_R^2}{\delta_{p,0}}$, and Gamma function $\Gamma(m+n+1)$, where $m+n+1$ is an integer. This requires that n must be an integer, and thus it can be seen that energy levels exist with fixed values of $\delta_{p,0}$, that are determined through the relation

$$\delta_{p,0} = \frac{\sqrt{\alpha}(n+2m+2)}{2} \pm \frac{\sqrt{4\Omega_R^2 + \alpha n^2 + 4\alpha n(m+1) + 4\alpha m^2 + 8\alpha m + 4\alpha^2}}{2} \tag{4.18}$$

For the $m = 0$ and $m = 1$ states on the lower polariton branch, one has

$$\begin{aligned} E_{0,m=0} &= \sqrt{2}Ae^{-\frac{\sqrt{\alpha}r^2}{2}} \\ \delta_{p,0,m=0,n} &= \frac{\sqrt{\alpha}(n+2)}{2} - \frac{\sqrt{4\Omega_R^2 + \alpha n^2 + 4\alpha n + 4\alpha^2}}{2} \\ E_{0,m=1} &= 2Are^{-\frac{\sqrt{\alpha}r^2}{2}} \\ \delta_{p,0,m=1,n} &= \frac{\sqrt{\alpha}(n+4)}{2} - \frac{\sqrt{4\Omega_R^2 + \alpha n(n+8) + 12\alpha + 4\alpha^2}}{2} \end{aligned} \tag{4.19}$$

Through which, it is seen that for small values of the quantum number, n there is an approximately linear spacing in the $\delta_{p,0}$, while as $\delta_{p,0} \to 0$, the separation becomes vanishingly small, which one can see in figure 4-1. It is noted that this unperturbed solution is a harmonic oscillator and thus is readily associated with energies of $\alpha(n+1)/2$ such that it is observed that in the presence of a potential the minimum of the lower branch is shifted towards a more positive detuning.

Now we take the inner product of the equation 4.16, with $(E_0\ \psi_0)$ to eliminate the unknown functions $E_1,\ \psi_1$ yielding

$$0 = \delta_{p,1}\int_0^\infty drr|E_0|^2 + |\psi_0|^2 + \int_0^\infty drr|\psi_0|^4$$

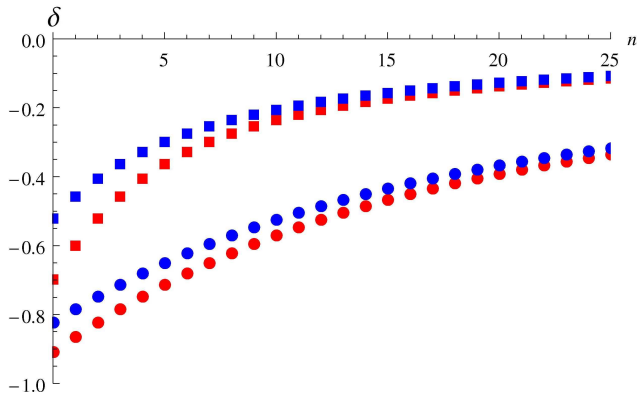

Figure 4-1: *Plot of $\delta_{p,0}$ against quantum number, n for $\alpha = 0.01$ (dot), $\alpha = 0.1$ (square) with $m = 0$ (red) and $m = 1$ (blue).*

$$0 = \delta_{p,1}\int_0^\infty drr(1+\left(\frac{\Omega_R}{\delta_p}\right)^2)|E_0|^2 + \left(\frac{\Omega_R}{\delta_p}\right)^4\int_0^\infty drr|E_0|^4 \tag{4.20}$$

from the equation in E_1, where E_{0mn} is defined as previously. For the ground state, it follows that

$$\begin{aligned}\delta_{p,1m=0n=0} &= \frac{2A^2\Omega_R^4}{\delta_{p,000}^2(\delta_{p,000}^2+\Omega_R^2)}\\ \delta_{p,1m=1n=0} &= \frac{A^2\Omega_R^4}{\sqrt{\alpha}\delta_{p,010}^2(\delta_{p,010}^2+\Omega_R^2)}\end{aligned} \tag{4.21}$$

Solving for A yields

$$\begin{aligned}A_{m=0n=0} &= \pm\frac{\sqrt{\delta_p-\delta_{p,000}}\delta_{p,000}\sqrt{\delta_{p,000}^2+\Omega_R^2}}{\sqrt{2}\Omega_R^2}\\ A_{m=1n=0} &= \pm\frac{\alpha^{1/4}\sqrt{\delta_p-\delta_{p,010}}\delta_{p,010}\sqrt{\delta_{p,010}^2+\Omega_R^2}}{\Omega_R^2}\end{aligned} \tag{4.22}$$

which we substitute back into the equation for E_0 and expressing $\delta_{p,1} = \delta_p - \delta_{p,0}$. This allows one to calculate a perturbative expression for the integral $\int d\theta \int_0^\infty dr|E|^2 r$ and thus obtain a curve for the number of photons as a function of the detuning, which is displayed in figure 4-2(b), wherein it is unsurprising to note that the particle number increases as the detuning of the pump tends to

zero from below.

4.1.3 Variational Approach

Given that perturbative localized vortex solutions exist, we now proceed to investigate whether a variational approach is able to adequately model the solution to the system of equations 4.1 and 4.2. Using the standard approach, we assume the trial functions

$$E_{tr,m} = A_m e^{-\beta_m r^2}, \quad \psi_{tr,m} = B_m e^{-\beta_m r^2} \tag{4.23}$$

Now, we consider small variations in the action, $S = \int_{t_1}^{t_2} dt \int dV L_d$, where the Lagrangian density is defined through

$$L_d = i\left(E^* \frac{\delta}{\delta t} E + \psi^* \frac{\delta}{\delta t}\psi - E\frac{\delta}{\delta t}E^* - \psi\frac{\delta}{\delta t}\psi^*\right) - H_d \tag{4.24}$$

where the Hamiltonian density is given through the relation, $H = \int dV H_d$ and the Hamiltonian, H is given through the relation

$$i\frac{\delta}{\delta t}\phi_i = \frac{\delta}{\delta \phi_i^*} H$$

thus

$$\begin{aligned} i\frac{\delta}{\delta t}E &= \nabla^2 E + (\delta_p + U)E + \Omega_R \psi \\ -i\frac{\delta}{\delta t}E^* &= \nabla^2 E^* + (\delta_p + U)E^* + \Omega_R \psi^* \\ i\frac{\delta}{\delta t}\psi &= (\delta_p - |\psi|^2)\psi + \Omega_R E \\ -i\frac{\delta}{\delta t}\psi^* &= (\delta_p - |\psi|^2)\psi^* + \Omega_R E^* \end{aligned} \tag{4.25}$$

through which the Hamiltonian is seen to be

$$H = |\nabla E|^2 + E^*(\delta_p + U)E + \Omega_R(E^*\psi + E\psi^*) + \psi^*(\delta_p - \frac{1}{2}|\psi|^2)\psi \tag{4.26}$$

It readily follows that the action is given by

$$\begin{aligned} S &= i\left(\langle E|\frac{d}{dt}E\rangle - \langle E|\frac{d}{dt}E\rangle^* + \langle\psi|\frac{d}{dt}\psi\rangle - \langle\psi|\frac{d}{dt}\psi\rangle^*\right) \\ &- \int_0^\infty |\nabla E|^2 + E^*(\delta_p + U)E + \Omega_R(E^*\psi + E\psi^*) \\ &+ \psi^*(\delta_p - \frac{1}{2}|\psi|^2)\psi \end{aligned} \tag{4.27}$$

And thus one obtains a triplet of equations to minimize for $m = 0$

$$\begin{aligned} -A_0\left(\alpha + 4\beta_0\left(3\beta_0 - \delta_p\right)\right) + 4B_0\beta_0\Omega_R &= 0 \\ -4B_0^2\beta_0\delta_p + A^2\left(3\alpha - 4\beta_0\left(3\beta_0 + \delta_p\right)\right) - 8A_0B_0\beta_0\Omega_R + 2B_0^4\beta_0 &= 0 \\ -B_0^3 + \sqrt{2}B_0\delta_p + \sqrt{2}A_0\Omega_R &= 0 \end{aligned} \tag{4.28}$$

and a similar set for $m = 1$

$$\begin{aligned} A_1\left(-3\alpha + 4\beta_1\left(-5\beta_1 + \delta_p\right)\right) + 4B_1\beta_1\Omega_R &= 0 \\ 8\sqrt{2}A_1^2\left(15\alpha + 4\beta_1\left(5\beta_1 - 3\delta_p\right)\right) & \\ +3B_1\left(5B_1^3 - 32\sqrt{2}B_1\beta_1\delta_p - 64\sqrt{2}A_1\beta_1\Omega_R\right) &= 0 \\ -3B_1^3 + 16\sqrt{2}B_1\beta_1\delta_p + 16\sqrt{2}A_1\beta_1\Omega_R &= 0 \end{aligned} \tag{4.29}$$

Solving these equations numerically, it is found that a minimum potential-dependent value of the detuning parameter exists, above which solutions can be found as in the perturbative case. Close to this cut-off, there is good agreement between the perturbative and variational forms of E and ψ, while the solutions separate as the system is tuned towards resonance. A comparison of the form of the photon field illustrates that the magnitude of the perturbative solution is always less than that associated with the variational solution, while in figure 4-2(a), one can see that there is good agreement between perturbative and variational methods in the limit of weak potentials for both $m = 0$ and $m = 1$, however as the potential strength increases the difference increases with perturbative solution is always at a lower detuning than that for the variational solution. Given that such a cut-off exists in both models, we now examine the agreement between the particle numbers determined in each model. This can be observed within figure 4-2(b) wherein it is observed that they are also agree.

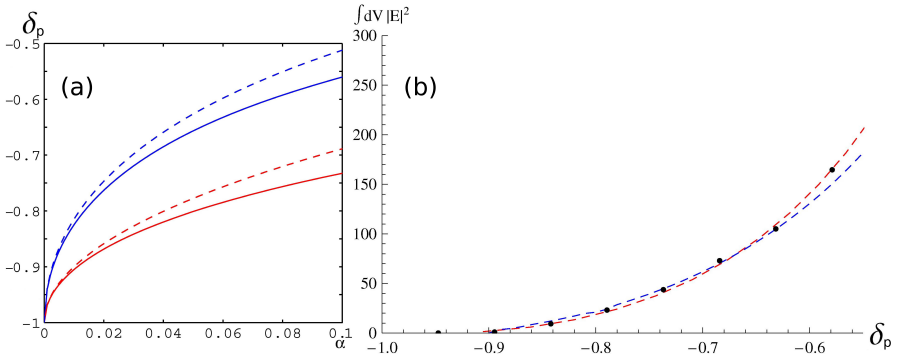

Figure 4-2: *(a) Plot of the detuning parameter, δ_p against potential strength, α for $m = 0$ (red) and $m = 1$ (blue) where the solid line denotes the solution cut-off associated with the variational approach, and the dashed line shows equivalent curve associated with the perturbative solutions.*
(b) Plot of $\int d\theta \int drr|E|^2$ against δ_p for $m = 1$ and $\alpha = 0.01$, focused on the region about the cut-off, where numerical results are marked in black. The red dashed line represents the perturbative approach whilst the blue dashed line displays the variational approach.

4.2 Stationary Solutions

Having obtained analytic approximations to the solutions and determined that a potential dependent cut-off exists; we proceed to solve the stationary system, which is displayed through

$$\begin{aligned} -i\nabla^2 E(r,\theta) - i(\delta_p - \alpha r^2)E(r,\theta) &= i\Omega_R \psi(r,\theta) \\ -i\delta_p \psi(r,\theta) + i|\psi(r,\theta)|^2\psi(r,\theta) &= i\Omega_R E(r,\theta) \end{aligned} \tag{4.30}$$

First, we make the substitutions

$$E(r,\theta) = E_a(r)e^{im\theta} \ , \quad \psi(r,\theta) = \psi_a(r)e^{im\theta} \tag{4.31}$$

to obtain the system

$$\begin{aligned} \frac{d^2}{dr^2}E_a + \frac{1}{r}\frac{d}{dr}E_a - \frac{|m|^2}{r^2}E_a + (\delta_p - \alpha r^2)E_a &= -\Omega_R \psi_a \\ \delta_p \psi_a - |\psi_a|^2\psi_a &= -\Omega_R E_a \end{aligned} \tag{4.32}$$

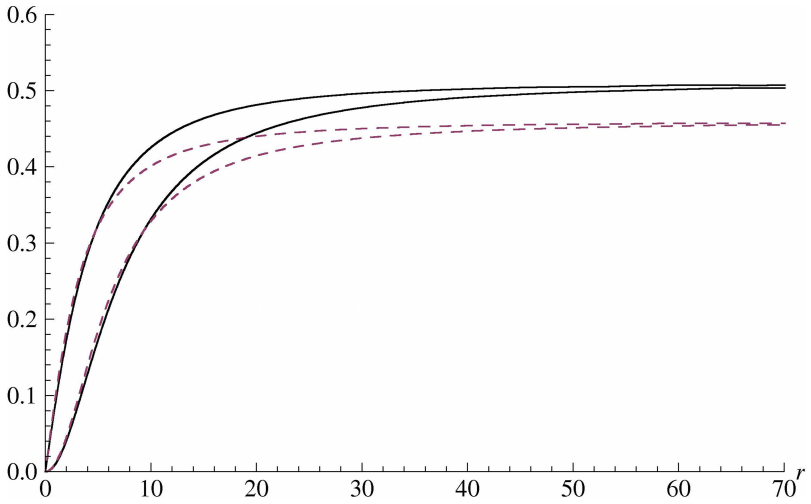

Figure 4-3: *Plots of E and ψ, at $\Omega = 1$, $\delta_p = -0.9$ in the absence of a potential where the successive curves for the (black) ψ and (purple) E-fields with winding numbers of $m = 1$ and $m = 2$.*

where $E(r)$ satisfies the boundary conditions

$$\begin{aligned} \lim_{r\to 0} E_a &= r^{|m|} \\ \lim_{r\to\infty} E_a = -\frac{\Omega_R}{\delta_p}\sqrt{\delta_p - \frac{\Omega_R^2}{\delta_p}} \quad & U(r) = 0 \\ \lim_{r\to\infty} E_a = 0 \quad & U(r) \neq 0 \end{aligned} \tag{4.33}$$

In the absence of a potential, one can observe the form of the solutions for $m = 1, 2$ vortices at $\delta_p = -0.9$ in figure 4-3, where it is clear that while $r \to 0$ the fields can be approximated by x^m, whilst as $r \to \infty$ the solutions tend towards the same background value, where it is apparent that the healing length increases with m, while we note that it remains largely independent of changes in δ_p.

As one increases the potential strength at a constant detuning, it is observed that the solutions become progressively more localized, with a correspondingly reduced particle number. As one increases the detuning parameter, it is observed that the solutions become progressively less confined, as can be observed in figure 4-4, where one can see that the effects of variation in both the potential strength and the frequency, through which it is noted that the decrease in the frequency results in a more sharply peaked solution.

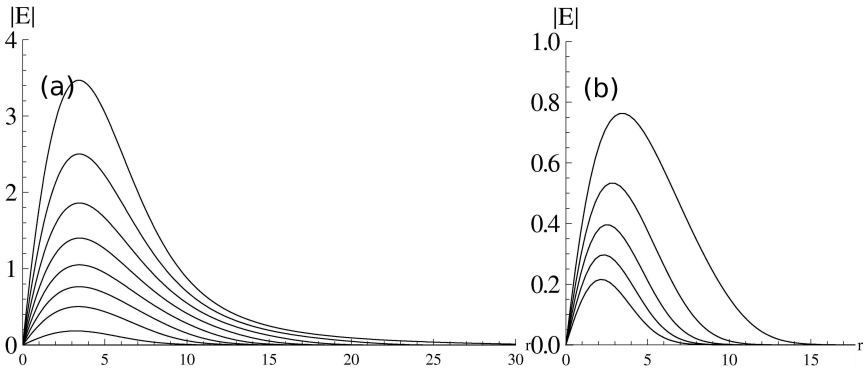

Figure 4-4: *(a) Plot of $|E|$, against radius, at constant $\alpha = 0.01$, for $m = 1$. The uppermost solid line corresponds to $\delta_p = -0.1$, with each following solid line corresponding to a decrease in δ_p of 0.1 units.*
(b) Plot of $|E|$, against radius, at constant $\delta_p = -0.66$ for $m = 1$. The uppermost solid line corresponds to $\alpha = 0.02$, with each following solid line corresponding to an increase in α of 0.0002 units.

In figure 4-2(b), the black points illustrates that good agreement exists between the three models. From which it is seen that the variational approach is capable of providing an acceptable approximation to the true solution, in the limit of detuning close to lower branch of the dispersion relation.

Having determined how the form of the stationary solutions varies with the detuning parameter and potential strength, we now investigate the presence of instabilities within the stationary system, in the same manner as performed previously for the homogeneous system to obtain the eigenvalue equation

$$\lambda \begin{pmatrix} g_{1+} \\ g_{1-} \\ g_{2+} \\ g_{2-} \end{pmatrix} = i \begin{pmatrix} L_+ & 0 & \Omega_R & 0 \\ 0 & -L_-^* & 0 & -\Omega_R \\ \Omega_R & 0 & Q & -|\psi|^2 \\ 0 & -\Omega_R & |\psi|^2 & -Q^* \end{pmatrix} \cdot \begin{pmatrix} g_{1+} \\ g_{1-} \\ g_{2+} \\ g_{2-} \end{pmatrix} \tag{4.34}$$

where

$$\begin{aligned} L_\pm &= \nabla_\pm^2 + \delta_p - \alpha r^2 \\ \nabla_\pm^2 &= \frac{d^2}{dr^2} + \frac{1}{r}\frac{d}{dr} - \frac{|m \pm l|^2}{r^2} \\ Q &= \delta_p - 2|\psi|^2 \end{aligned} \tag{4.35}$$

and the perturbation is treated as a linear superposition of modes with different

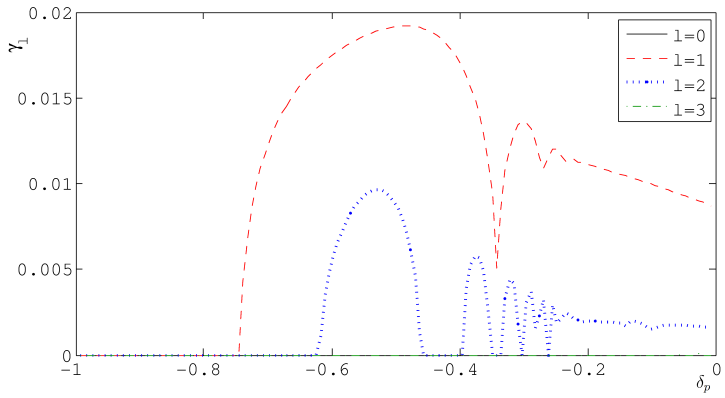

Figure 4-5: *Plot of growth rate against the detuning parameter, δ_p for $m = 2$, $\alpha = 0.01$ and l=0 (solid), l=1 (dashed), l=2 (dotted), l=3 (dot dash).*

azimuthal symmetry [167, 204] where the parameter l takes only integer values, and indicates the azimuthal mode of the perturbation. We solve this equation using the numerically determined $|\psi|^2$, and through an examination of the nonzero real components of the eigenvalues of the system, λ, one can obtain information about the stability of the system, where the maximum instability growth rate is given by $\gamma_l = max[\Im(\lambda)]$. Solving for γ_l as a function of the cavity detuning in the presence of a potential determines that both $m = 0$ and $m = 1$ solutions are stable with respect to all azimuthal perturbations, over the entire range of possible detuning parameters, for small perturbations to the system in the vicinity of the solution, as all non-zero real parts are negative. In contrast, it is found that higher order vortices are unstable over the entire range, where the azimuthal mode, $l = 1$ is generally dominant, however these higher order vortices are also stable with respect to symmetric perturbations, with $l = 0$. In figure 4-5, one can observe the variation in the instability growth rate as a function of the detuning parameter for azimuthal modes l = 0,1,2,3, where it is seen that there exist a number of competing unstable eigenmodes, which are always located along the axis.

4.3 Evolution of Vortices

Having examined a selection of the properties of vortices in the absence of loss or pumping terms, we now reinstate these and proceed to examine the formation of polariton vortices within a lossy cavity, under the influence of a noisy pump of finite width with some initial momentum, and a vortex seed possessing zero momentum, when the cavity is pumped such that we are working in the parametric scattering regime.

This is achieved through returning to the full model with pump and damping terms and introduce a Gaussian width on the pumping term, and a vortex seed of the form $E_p s e^{im\theta} e^{-(x^2+y^2)/(2\sigma^2)} e^{-t^2/(2\sigma_t^2)}$.

$$\begin{aligned} \frac{\delta}{\delta t} E &- i\nabla^2 E + (\gamma_{ph} - i\delta_p)\, E \\ &= i\Omega_R \psi + E_p e^{ik_p x} e^{-\frac{x^2+y^2}{2W^2}} + E_p s e^{im\theta} e^{-(x^2+y^2)/(2\sigma^2)} e^{-t^2/(2\sigma_t^2)} \\ \frac{\delta}{\delta t}\psi &+ \left(\gamma_e - i\delta_p + i|\psi|^2\right)\psi = i\Omega_R E \end{aligned} \tag{4.36}$$

where γ_{ph} is the cavity damping, γ_e is the exciton damping, E_p is the pump strength and k_p is the pump momentum. W and σ are the pump and vortex seed widths respectively, while s is the vortex seed fraction and σ_t is the temporal width of the vortex seed, for a vortex with winding number, m. Through this, one expects to observe the formation of a vortex antivortex pair possessed of different momenta, in a manner that is analogous to that observed in previous models [81] and experiments [93, 141] when parametric oscillations exist.

When the system in pumped below the parametric threshold, such that the signal and idler instability domains are connected, it is observed that the signal and idler regions do not experience substantial growth relative to the pump band, and we confirm that when one works far below the parametric threshold, there is no coupling into the idler band at $k = 2k_p$ which is as expected. Once the system is pumped strongly enough to operate above this threshold and a vortex seed is present, it is evident that a $m = \pm 1$ vortex-antivortex pair is formed as seen through the presence of a forked dislocation within the interference plots. This can be seen in figure 4-6 where the reversal of the fork indicates a change in the sign of the winding number, while the presence of two branches indicates that the vortex have a winding number of $m = \pm 1$.

Through the seeding of a single $m = 1$ vortex within the signal band, at $k_s = 0$

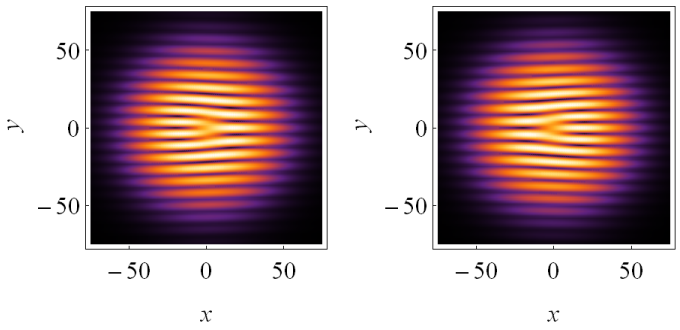

Figure 4-6: *Interference plots of the signal (Left) and idler (Right) with the pump, displaying characteristic fork diagrams for the vortex, and antivortex at* $\delta_p = -0.05$, $k_p = \pi/2$, $E_p = 0.25$, $\sigma_r = 25$, $\sigma_v = 5$ *and* $\gamma_{ph} = \gamma_e = 0.1$ *evaluated at* $t = 15$.

one can see that parametrically generated vortices are stable within polariton condensates, as illustrated within figures 4-7, 4-8 and 4-9. Through which, it is seen that parametrically generated vortices can exist across a range of energy above the inflection point. It is noted that the presence of a narrow Gaussian pump centered at $(x = 0, y = 0)$ in figure 4-9 makes the presence of a drift velocity in the roll pattern substantially more notable than in the flat case. This evolution has been experimentally observed in the paper by Marchetti *et al.* [113, 180] amongst others.

4.3.1 Evolution of Higher Order Vortices

If one replaces the $m = 1$ vortex seed with with a higher order vortex, it is observed that a $m = n$, vortex rapidly evolves into n $m = 1$ vortices, over approximately ten time units. One can observe this in figure 4-10 after 5 and 100 time units respectively, for an $m = 2$ vortex [147]. Similarly, vortices with higher winding numbers have been observed to develop in the same manner. Once these $m = n$ vortices have split, the resulting n $m = 1$ vortices behave as if they are a set of n particles possessed of equal charge. All but one of these vortices will be expelled from the signal region and dissipate, whilst the remaining vortex will stabilize.

4.4 Honeycomb Vortex Lattices

Up to this point, we have focused upon the evolution of single vortices within the system. Now, we introduce the concept of a lattice of vortices and antivortices

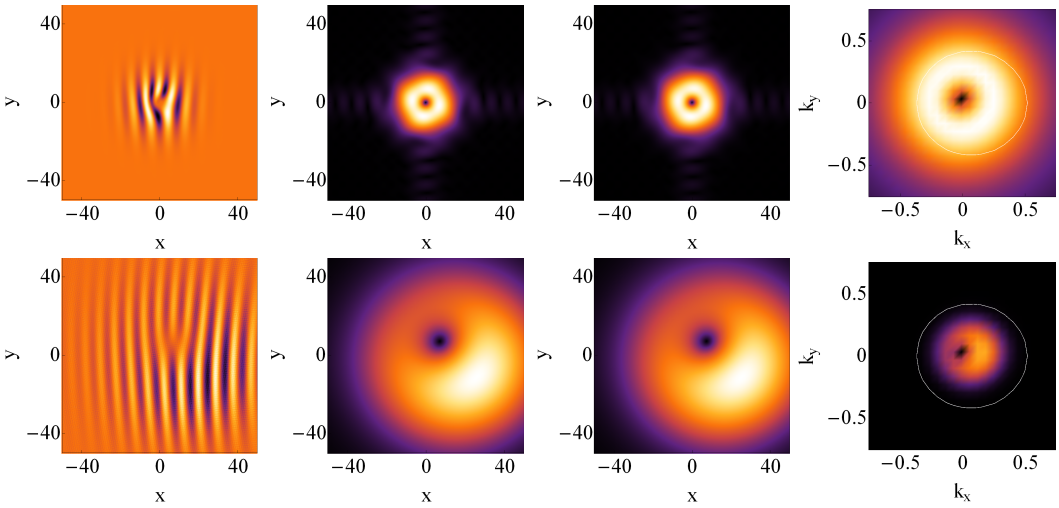

Figure 4-7: *Real-space plot of the exciton density, $|\psi|^2$ (Far Left), the signal (Center Left) and the idler (Center Right). The far right panel displays a k-space plot centered upon the signal region, as evaluated for $\delta_p = -0.05$, $k_p = \pi/2$, $E_p = 0.45$, $k_s = 0.0$ and $\gamma_{ph} = \gamma_e = 0.1$, growing from a seed vortex at $t = 5$(top) and $t = 80$(bottom). These parameters correspond to those in figure 3-1(e).*

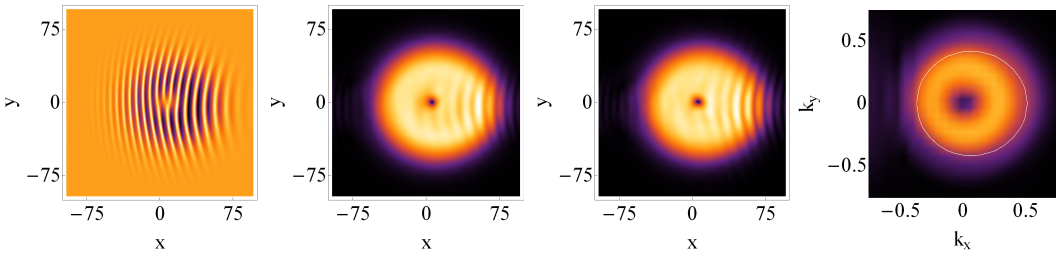

Figure 4-8: *Real-space plot of the exciton density, $|\psi|^2$ (Far Left), the signal (Center Left) and the idler (Center Right) intensity. The far right panel displays a k-space plot centered upon the signal region, as evaluated for $\delta_p = -0.05$, $k_p = \pi/2$, $E_p = 0.213$, $k_s = 0.0$ and $\gamma_{ph} = \gamma_e = 0.1$, growing from a seed $m = 1$ vortex at $t = 80$. These parameters correspond to those in panel (d) of figure 3-1.*

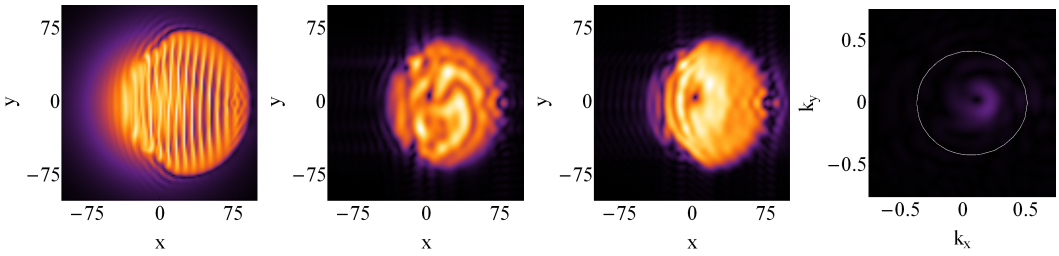

Figure 4-9: *Real-space plot of the exciton density, $|\psi|^2$ (Far Left), the signal (Center Left) and the idler (Center Right) intensity. The far right panel displays a k-space plot centered upon the signal region, as evaluated for $\delta_p = -0.05$, $k_p = \pi/2$, $E_p = 0.45$, $k_s = 0.0$ and $\gamma_{ph} = \gamma_e = 0.1$, growing from a seed $m = 1$ vortex at $t = 80$, for a Gaussian pump of width, $\sigma_v = 25$.*

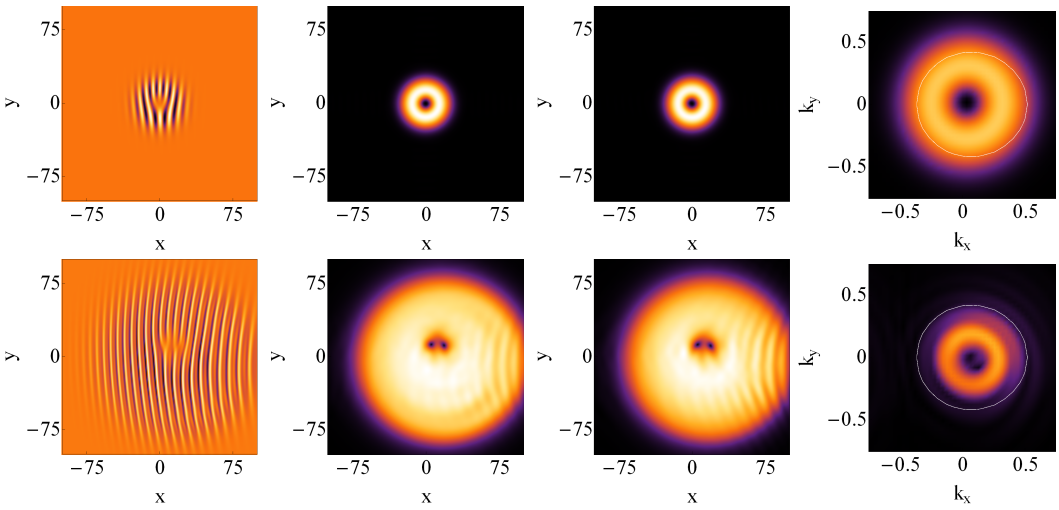

Figure 4-10: *Real-space plot of the exciton density, $|\psi|^2$ (Far Left), the signal (Center Left) and the idler (Center Right) intensity. The far right panel displays a k-space plot centered upon the signal region, as evaluated for $\delta_p = -0.05$, $k_p = \pi/2$, $E_p = 0.45$, $k_s = 0.0$ and $\gamma_{ph} = \gamma_e = 0.1$, growing from a seed $m = 2$ vortex, for a flat pump configuration for $t = 5$ (top) and $t = 100$ (bottom).*

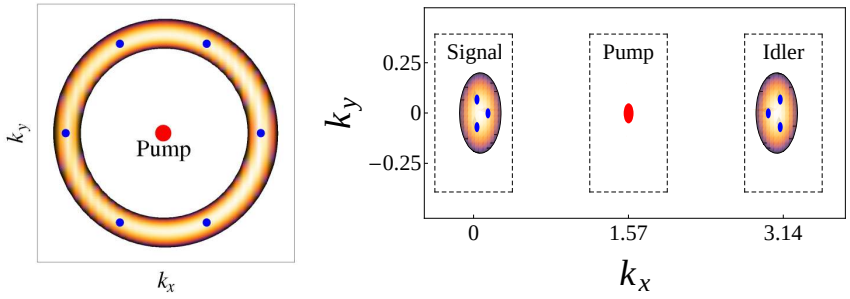

Figure 4-11: *Schematic diagram illustrating the typical distribution of Fourier components from the conventional hexagonal (left) structure and the honeycomb lattice (right) structure.*

within the optical parametric oscillator regime. These lattices are a new type of hexagonal patterns, where there is a significant difference in the distribution of the Fourier components from the conventional hexagons known in nonlinear optics [49, 187, 92] illustrated in the left panel of figure 4-11, whilst the right panel displays the distribution of Fourier components resulting from the system studied within this chapter, which corresponds to honeycomb lattices typically studied in BEC systems [142]. In principle, this is achievable experimentally as excitation of microcavities with multiple precisely arranged beams has been reported in references [139, 10, 154].

We generate a honeycomb lattice through the interference of three beams held at 120° to each other[143] of the form

$$P_{s,i} = v_{s,i}e^{2ipx} + w_{s,i}e^{-ip(x+\sqrt{3}y)} + u_{s,i}e^{-ip(x-\sqrt{3}y)} \tag{4.37}$$

where probe momentum, $p << |k_p|$ whereby it belongs to the parametric instability domain about $k_x = 0$, as shown in figure 3-1. This arrangement of probe beams serves to create a regular hexagonal lattice in position-space with a lattice spacing inversely proportional to p that consists of alternating vortices and antivortices, which in momentum space corresponds to an equilateral triangle centered about $k_x = 0$, where we initially hold the lattice spacing at $p = \pi/80$.

4.4.1 The Lattice Equation

Now, we proceed to derive a set of approximate equations that govern the behavior of a honeycomb lattice, where we begin by reproducing the relevant equation

for convenience

$$\begin{aligned} \frac{d}{dt}E &- i\nabla^2 E + (\gamma_{ph} - i\delta_p)\, E = i\Omega_R \psi + E_p e^{ik_p x} \\ \frac{d}{dt}\psi &+ \left(\gamma_e - i\delta_p + i|\psi|^2\right)\psi = i\Omega_R E \end{aligned} \tag{4.38}$$

which, we now proceed to expand the E and ψ-fields about $k = k_p$ to obtain

$$\begin{aligned} E &= A_p e^{ik_p x - i\delta_p t} + A_s e^{ik_s x - i\delta_s t} + A_i e^{ik_i x - i\delta_i t} \\ \psi &= Q_p e^{ik_p x - i\delta_p t} + Q_s e^{ik_s x - i\delta_s t} + Q_i e^{ik_i x - i\delta_i t} \end{aligned} \tag{4.39}$$

We assume that, from all unstable momenta within the $(\kappa_x,\ \kappa_y)$ plane, one can select a range of different patterns. Now we let $A_s = P_s$, $A_i = P_i^*$ and $|v_{s,i}| \approx |w_{s,i}| \approx |u_{s,i}| = E_p s$ and following the method developed in section 3.3, we obtain the set of equations

$$0 = (\alpha_s + 5|a_s|^2 + 2|\psi_p|^2 + 10|a_i|^2)a_s + \psi_p^2 a_i^* \tag{4.40}$$

$$0 = (\alpha_i + 5|a_i|^2 + 2|\psi_p|^2 + 10|a_s|^2)a_i + \psi_p^2 a_s^* \tag{4.41}$$

$$0 = (\alpha_p + |\psi_p|^2 + 6|a_s|^2 + 6|a_i|^2)\psi_p + 6a_s a_i \psi_p^* - \beta E_p \tag{4.42}$$

which lead to

$$\Im[\alpha_i]^2 + (\Re[\alpha_i] + 5|a_i|^2 + 10|a_s|^2 + 2|\psi_p|^2)^2 = |\psi_p|^4 \frac{|a_s|^2}{|a_i|^2} \tag{4.43}$$

and

$$\begin{aligned} |\beta|^2|E_p|^2 &= |\psi_p|^2|\alpha_p + |\psi_p|^2 + 6|a_s|^2 + 6|a_i|^2 \\ &- \frac{6|a_s|^2|\psi_p|^2}{\alpha_i + 5|a_i|^2 + 10|a_s|^2 + 2|\psi_p|^2}|^2 \end{aligned} \tag{4.44}$$

where β and $\alpha_{s,p,i}$ have been defined previously in the context of the roll solution through equation 3.30, which have been reproduced below for convenience

$$\begin{aligned}\beta &\equiv \frac{-i\Omega_R}{k_p^2-\delta_p-i\gamma_{ph}} \\ \alpha_{s,i,p} &\equiv -\delta_{s,i,p}-i\gamma_e-\frac{\Omega_R^2}{k_{s,i,p}^2-\delta_{s,i,p}-i\gamma_{ph}}\end{aligned}$$

As one is working within the parametric regime, one can use the relative phase symmetry between the signal and idler to make the symmetry transformation, $Q_s = Q_s e^{i\Phi}$, $Q_i = Q_i e^{-i\Phi}$ for arbitrary phase, Φ. This allows one to separate the system into real and imaginary components to obtain

$$\begin{aligned}|Q_i|^2 &= \frac{\Im(\alpha_s)}{\Im(\alpha_i)}|Q_s|^2 = \kappa|Q_s|^2 \\ |Q_s|^2 &= \frac{\Re(\alpha_s)-\Re(\alpha_i)\kappa+2|Q_p|^2(1-\kappa)}{5(\kappa^2-1)}\end{aligned} \tag{4.45}$$

and

$$\begin{aligned}\sin^2\omega &= \frac{\Im(\alpha_s)\Im(\alpha_i)}{|Q_p|^4} \\ \cos^2\omega &= \frac{\kappa}{|Q_p|^4(1-\kappa)^2}(\Re(\alpha_s)-\Re(\alpha_i)+|Q_s|^2(\kappa-1))^2\end{aligned} \tag{4.46}$$

where $\omega = 2\arg(Q_p)-\arg(Q_s)-\arg(Q_i)$. Now from the relation $\sin^2\omega+\cos^2\omega = 1$, one can obtain the quadratic equation

$$\begin{aligned}0 &= a|Q_p|^4+b|Q_p|^2+c \\ c &= \Im(\alpha_s)\Im(\alpha_i)(1-\kappa^2)^2+\kappa[2(\Re(\alpha_s)-\kappa\Re(\alpha_i))+\Re(\alpha_s)\kappa-\Re(\alpha_i)]^2 \\ b &= 4\kappa(1-\kappa)[2(\Re(\alpha_s)-\Re(\alpha_i)\kappa)+\Re(\alpha_s)\kappa-\Re(\alpha_i)] \\ a &= -(1-\kappa)^4\end{aligned} \tag{4.47}$$

We fix the pump parameters (δ_p, k_p) and scan over (δ_s, k_s) to obtain the solution set $|Q_p|(\delta_s, k_s)$. As before, this allows one to obtain the three amplitudes, $|Q_{s,p,i}|$. The discussed phase symmetry allows one to assume that $\arg(Q_s) = 0$, and from which it follows that $\arg(Q_i) = 2\arg(Q_p)-\omega$. Whilst one obtains $\arg(Q_p)$ through

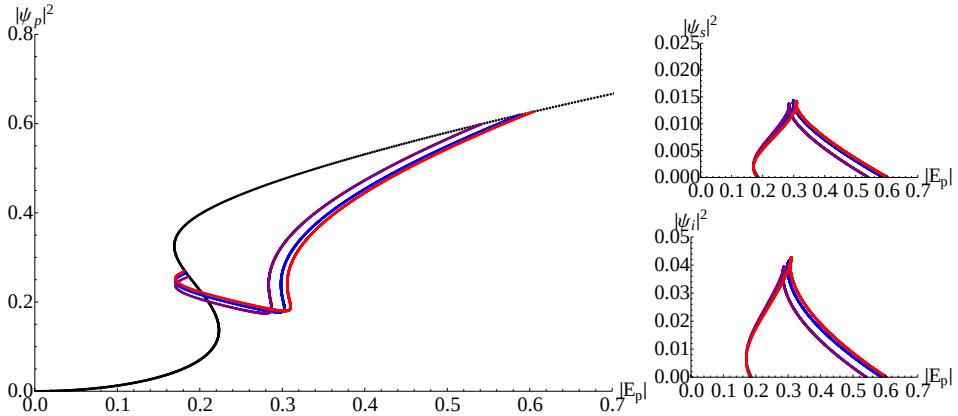

Figure 4-12: *Plot of the exciton number against pump strength for* $k_p = \pi/2$, $\delta_p = -0.05$ *and* $\gamma_e = \gamma_{ph} = 0.1$ *for the pump, signal and idler. The homogeneous solutions are shown in black. The honeycomb lattice solutions are seen at* $k_s = -0.21$*(purple),* $k_s = 0.07$ *(red) and* $k_s = 0.21$*(blue).*

$$\frac{1}{|Q_P|}\frac{iE_p e^{-i\arg(Q_p)}}{\delta_p + i\gamma_{ph} - k_p^2} = \alpha_p + |Q_p|^2 + 6|Q_s|^2 + 6|Q_i|^2 + 2|Q_s||Q_i|e^{-i\omega} \tag{4.48}$$

The solutions of this equation give us $\arg(Q_p)$ and the dependence $Q_p(E_p)$ which allows us to determine the modified E_p against $|\psi_{s,p,i}|$ curves in the presence of a honeycomb vortex lattice, which one can see in figure 4-12. Through which, it is seen that as one shifts the signal momentum away from the maximum of the instability region of the homogeneous solution, the magnitude and length of the signal and idler branches decreases.

4.4.2 Evolution under a Homogeneous Pump

From figure 3-1, it was noted that while the instability regions are positioned symmetrically about the pump momentum, the maximal growth rates are not located at the center of the instability regions. First, we consider the situation where the Fourier components of the seed lattice are orientated such that the growth rates are approximately symmetric about this maximum, while one of the components is positioned along the x-axis.

We initially utilize a flat pump and seed, whilst the system possessing the parameters: $E_p = 0.56$, $\gamma_{ph} = \gamma_e = 0.1$, $k_p = \pi/2$, $\delta_p = -0.05$, $k_s = 0.07$ and $p = \pi/80$. For a Rabi frequency of $\hbar\Omega_R = 4.99meV$, these parameters correspond

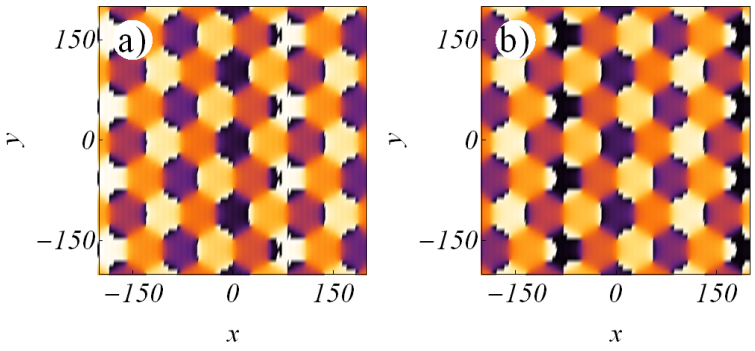

Figure 4-13: *Plots of* $arg(\psi)$*, evaluated for* $\delta_p = -0.05$*,* $k_p = \pi/2$*,* $E_p = 0.56$*,* $k_s = 0.07$ *and* $\gamma_{ph} = \gamma_e = 0.1$ *growing from a seed vortex, for a flat pump configuration for the* (a) *signal and* (b) *idler at* $t = 25$*.*

to $\hbar\delta_p \approx -0.25meV$, $\gamma_{ph} = \gamma_e \approx 0.5meV$, $k_p \approx 3.6\mu m^{-1}$, such that the nearest neighbor separation is approximately $20\mu m$, and one time unit corresponds to $0.188ps$. These parameters are such that the assumption $p << |k_p - k_s|$ is well satisfied. The vortex lattice is seeded through a Gaussian pulse centered at $t = 2.5(= 0.47ps)$ with a temporal width $W_t = 0.625(= 0.12ps)$.

Once the seed pulse has decayed, one is able to observe that additional Fourier components have been generated within the idler band. These components result in generation of vortex lattices within both the signal and idler which is best illustrated through plots of the phase as seen in figure 4-13. These lattices are seen to consist of both vortices and antivortices, wherein one finds that at the position of a vortex within the signal, there is a corresponding antivortex in the idler, as dictated by phase symmetry between signal and idler, where one can see that a closed path clockwise around a single vortex always has a phase change from 0 to 2π, corresponding to a jump from dark to light, whilst the opposite occurs to the case of an antivortex. Whilst there is no distortion of the lattice with time, it is shown in figure 4-14 that the lattice drifts along the pump axis in the same manner as for roll solutions where an approximate formula for this will be discussed in a later section.

Once the seed pulse has triggered the parametric amplification of the vortex lattice and decayed away, one can observe that the intra-cavity norms of the signal, pump and idler reach a quasi-stationary regime as seen in figure 4-15. Within this regime, it is seen that there is good agreement with the theory developed earlier. The duration of this state is seen to be highly dependent on the relative stability of the Fourier components. This dependence will be discussed in more

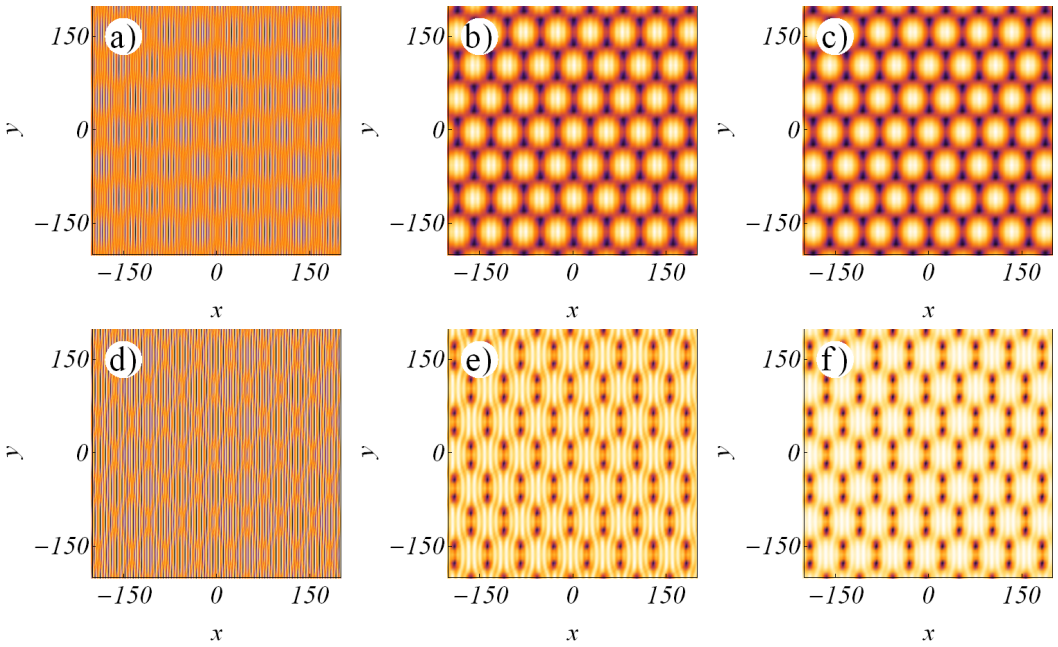

Figure 4-14: *Real-space plot of the exciton density, (a, d)* $|\psi|^2$*, the (b, e) signal and the (c, f) idler intensity, as evaluated for* $\delta_p = -0.05$*,* $k_p = \pi/2$*,* $E_p = 0.56$*,* $k_s = 0.07$ *and* $\gamma_{ph} = \gamma_e = 0.1$*, growing from a seed vortex for a flat pump configuration for* $t = 25$*(Top) and* $t = 300$*(Bottom).*

detail in section 4.4.4.

Recalling that we made the approximations $p < |k_p - k_s|$ as $u_s = v_s = w_s$ to allow for the derivation of the analytic estimate of the honeycomb branch, figure 4-16 demonstrates that these approximations are valid provided that the Fourier components are far from the edge of the instability domain when p is necessarily large. Additionally, the off-axes components, which are symmetrically positioned with respect to the pump axes, possess identical magnitudes.

4.4.3 Evolution under a Gaussian Pump

We now consider a Gaussian pump of the form

$$Pump = E_p e^{ik_p x} e^{-\frac{R^2}{2W^2}} \tag{4.49}$$

wherein one can observe that the presence of boundary effects serves to severely distort the form of the lattice resulting in its rapid destruction, shown for the ψ signal field in figure 4-17. Furthermore, one can see that the lattice only survives within the region where the effective pump strength at that position is such

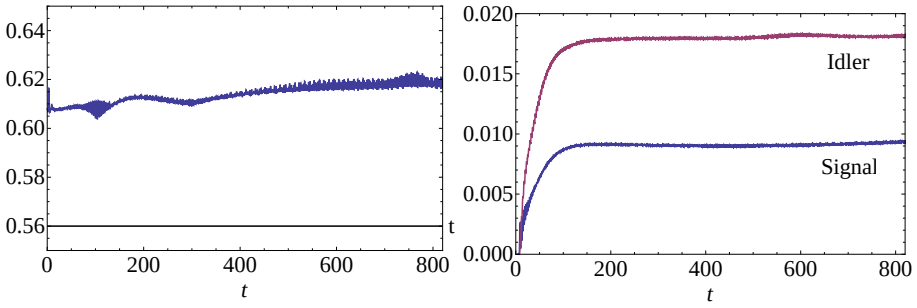

Figure 4-15: *Evolution of the average exciton density* $\langle|\Psi|^2\rangle = (1/S)\int d\vec{r}|\Psi|^2$*, of the spectrally filtered pump (left), signal and idler (right) intensity, over an area* S*.*

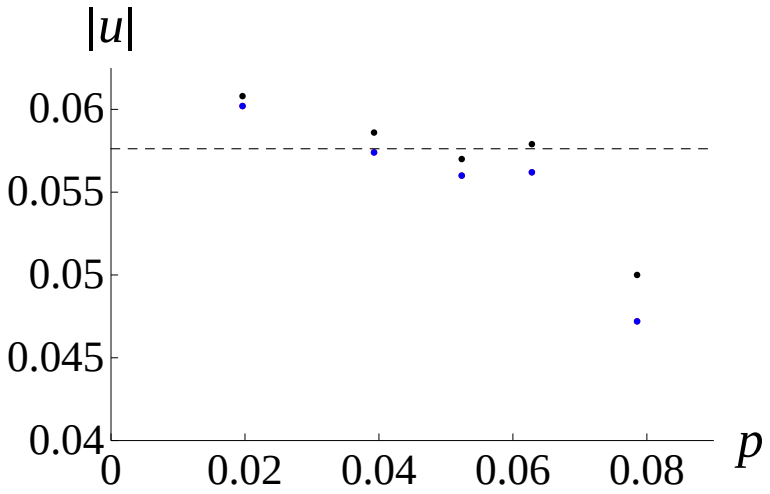

Figure 4-16: *Plot of the* $|u|$ *against the lattice spacing,* p *for* $E_p = 0.56$*,* $k_p = \pi/2$*,* $\delta_p = -0.05$ *and* $k_s = 0.07$*. The dashed line corresponds to the analytical prediction, whilst the black points correspond to the on axis components. The red and blue points correspond to the off axis components.*

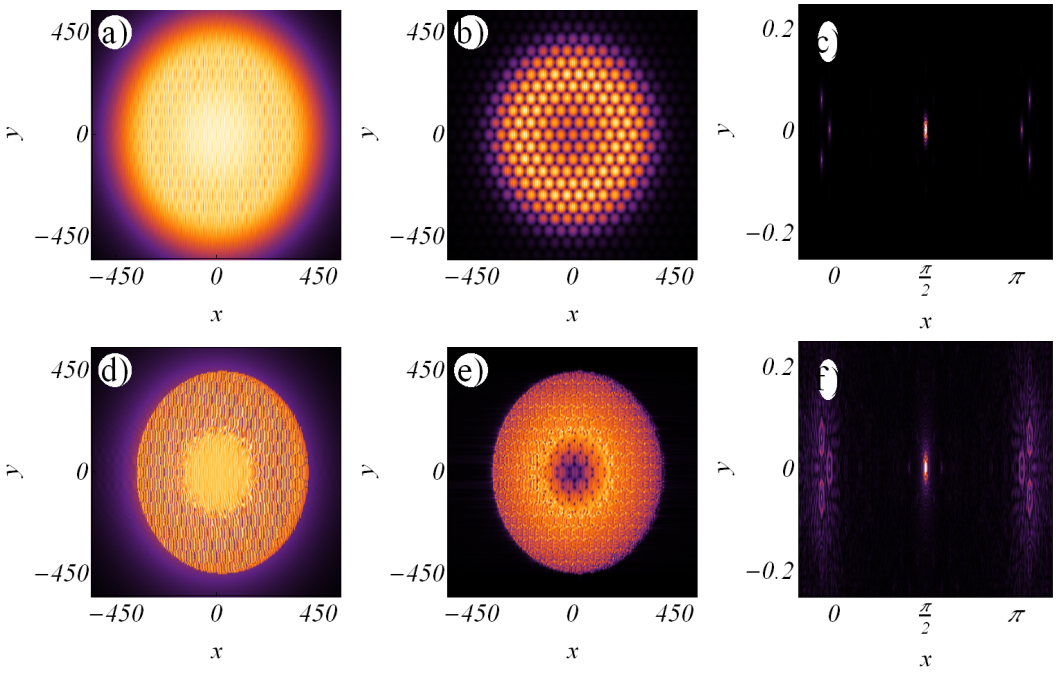

Figure 4-17: *Real-space plot of the total exciton intensity, (a, d)* $|\psi|^2$*, and the (b, e) signal intensity. Panel (c, f) displays a k-space plot centered upon the signal region, as evaluated for* $\delta_p = -0.05$*,* $k_p = \pi/2$*,* $E_p = 0.56$*,* $k_s = 0.07$*, and* $\gamma_{ph} = \gamma_e = 0.1$*, growing from a seed vortex, for a Gaussian pump configuration for* $t = 20$*(a,b,c) and* $t = 100$*(d,e,f), with width* $\sigma = 250$*.*

that one remains within the instability region. In practice, when one is working towards the upper end of this region, this corresponds to a region with a radius that is approximately one standard deviation located about the pump maximum.

We now take a super-Gaussian pump of the form

$$Pump = E_p e^{ik_p x} e^{-\frac{R^{100}}{2W^{100}}} \tag{4.50}$$

and through which it is seen that the boundary effects are significantly reduced as the gradient of the pump profile about the central region tends to zero, as illustrated in figure 4-18. From these two examples, it is evident that the structure of the hexagonal lattice is not significantly distorted by the presence provided that the pump intensity gradient is sufficiently shallow, which can be achieved by increasing the width of the pump beam or through the use of a super-Gaussian beam.

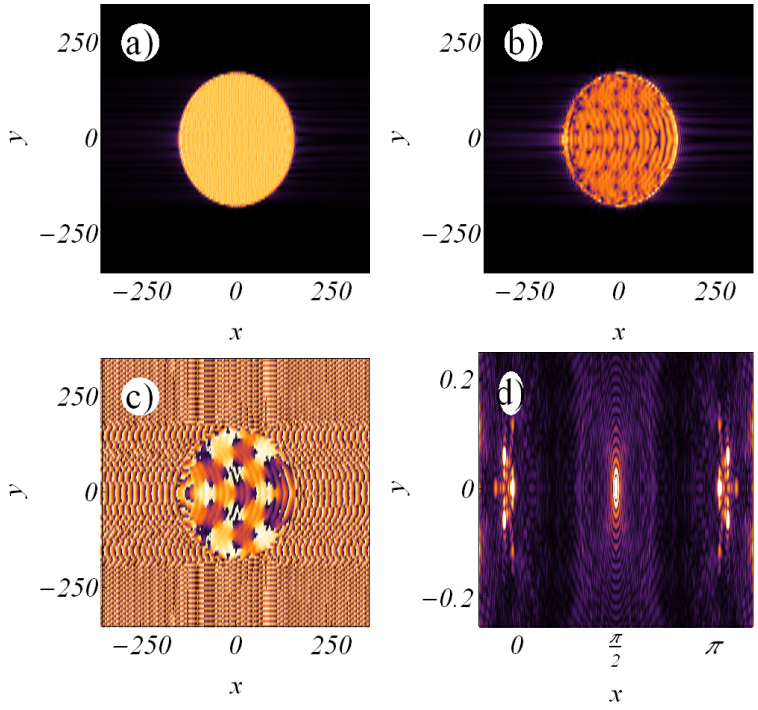

Figure 4-18: *Real-spaces plot of the (a) exciton intensity, $|\psi|^2$ and (b) signal. Panel (c) displays the phase of the signal, whilst panel (d) displays the momentum space image. The super Gaussian pump of width $W = 250$ has been evaluated for $\delta_p = -0.05$, $k_p = \pi/2$, $E_p = 0.56$, $k_s = 0.07$ and $\gamma_{ph} = \gamma_e = 0.1$ at $t = 100$.*

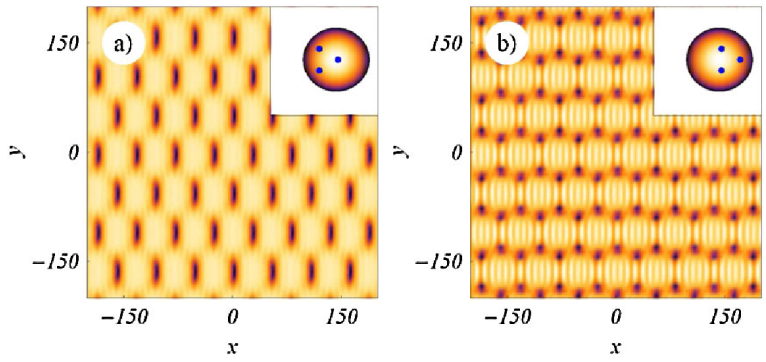

Figure 4-19: *Plot of the signal exciton density, evaluated for* $\delta_p = -0.05$, $k_p = \pi/2$, $E_p = 0.56$ *and* $\gamma_{ph} = \gamma_e = 0.1$, *at (a)* $k_s = 0$, $t = 80$, *and (b)* $k_s = 0.14$, $t = 250$. *The insets display the momentum space configuration for the respective fields. For a Rabi frequency of* $\hbar\Omega_R \approx 5meV$, *these times correspond to* $15ps$ *and* $47ps$ *respectively, while the nearest neighbor vortices are initially separated by* $20\mu m$.

4.4.4 Lattice Melting Scenarios

In section 4.4.2, we have seen that the lifetime of the observed quasi-stationary states is highly dependent upon the stability of the Fourier components. Here, we proceed to investigate this through the repositioning of the lattice seed within the instability region about $k_x = 0$.

First, we shift the seed away from the pump along that axis, such that the Fourier component along the axes is greater than the off-axes components, as illustrated in the insets of figure 4-19. This combination of growth rates is seen to result in the rapid merging of adjacent vortices and antivortices, in the direction perpendicular to the pump, such that the system returns to the homogeneous solution, which is illustrated through figures 4-19(a) and 4-20(a). As one increases the difference between these components, it is observed that this merging of vortices and antivortices occurs at an increasing rate.

However if one shifts the lattice seed, such that the off-axis components are just greater than the on-axis component, then one initially observes the creation of lines of vortices and antivortices, along the pump axes. As one moves further away from the maximum, such that the perpendicular components are significantly greater, then it is observed that whilst initially the system compresses into the vortex lines previously shown, it rebounds to a system that resembles the initial lattice. At later times, these vortex-antivortex pairs proceed to merge along the path of greatest distance perpendicular to the pump direction, illustrated in panel (b) of figures 4-19 and 4-20.

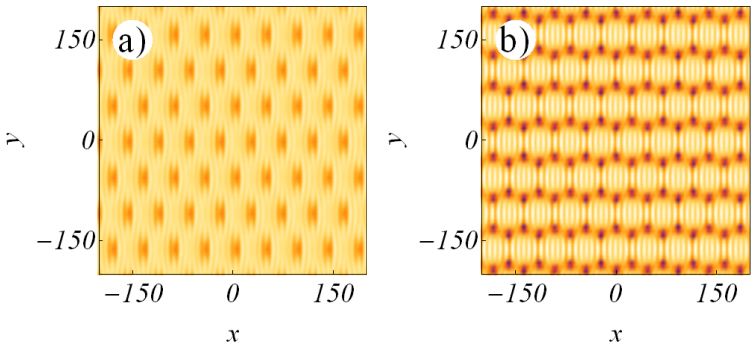

Figure 4-20: *The same as figure 4-19, but with the seed momentum k_s is shifted to either side of the optimal value, $k_{opt} \approx 0.07$ leading to the two melting scenarios illustrated for (a) $k_s = 0$ at $t = 120$ and for (b) $k_s = 0.14$ at $t = 450$. For a Rabi frequency of $\hbar\Omega_R \approx 5meV$, these times correspond to 22ps and 85ps respectively, while the nearest neighbor vortices are initially separated by $20\mu m$.*

4.4.5 Existence Domain of stable solutions

In the previous sections, we have shown that stable solutions can be found when the gain associated with each of the three Fourier components is equal. This has been seen to occur at a value of $k_s = k_{opt} \neq 0$. and thus through these conditions, we determine a region in the (k_s, E_p) plane where stable solutions may exist. We find this by evaluating the maximally unstable eigenvalue of equation 3.8 at $\vec{\kappa} = (k_{opt} + 2p, 0)$ and $\vec{\kappa} = (k_{opt} - p, \pm\sqrt{3}p)$, where the form of the eigenvalues on the lower polariton branch has been reproduced below

$$\begin{aligned} \lambda &= \frac{\tilde{\Omega}_i - \tilde{\Omega}_s - i\left[2\bar{\gamma} + \gamma_d(\epsilon_\alpha + \epsilon_\beta)\right]}{2} \\ &\pm \sqrt{\frac{\left[\tilde{\Omega}_i + \tilde{\Omega}_s - 2\delta_p + i\gamma_d(\epsilon_\beta - \epsilon_\alpha)\right]^2}{4} - \frac{|\Psi_0|^4}{\alpha^2\beta^2}} \end{aligned} \tag{4.51}$$

$$\begin{array}{ccc} \bar{\gamma} = \frac{\gamma_{ph}+\gamma_e}{2} & \gamma_d = \frac{\gamma_{ph}-\gamma_e}{2} & \epsilon_\alpha = (\Omega_i^2 - 1)/\alpha^2 \\ \epsilon_\beta = (\Omega_s^2 - 1)/\beta^2 & \tilde{\Omega}_i = \Omega_i + 2|\Psi_0|^2/\alpha^2 & \tilde{\Omega}_s = \Omega_s + 2|\Psi_0|^2/\beta^2 \\ & \alpha^2 = 1 + \Omega_i^2 & \beta^2 = 1 + \Omega_s^2 \\ & \Omega_i(\vec{\kappa}) = \Omega(\vec{k}_p + \vec{\kappa}) & \Omega_s(\vec{\kappa}) = \Omega(\vec{k}_p - \vec{\kappa}) \end{array} \tag{4.52}$$

Now the eigenvalues $(k_{opt} - p, \sqrt{3}p)$ and $(k_{opt} - p, -\sqrt{3}p)$ are identical due to symmetry with respect to reflection in the x-axis, as seen in figure 4-21(a), where

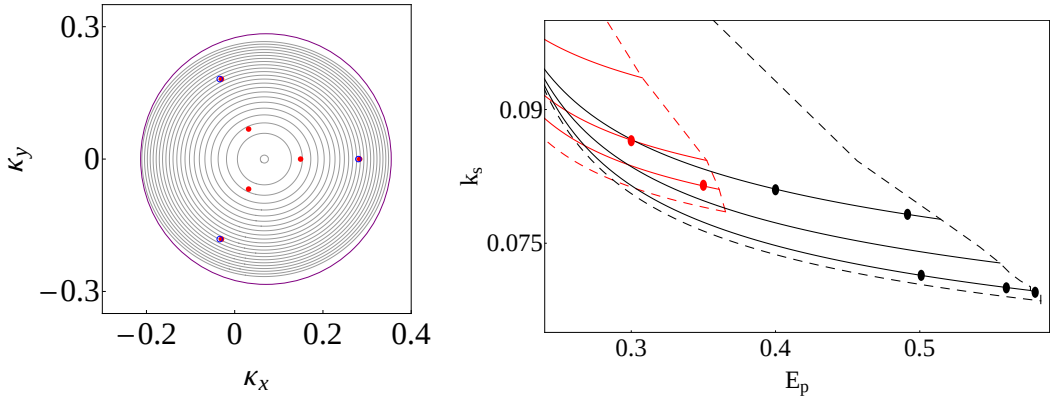

Figure 4-21: *(a) Instability plot evaluated at* $E_p = 0.54$, $k_p = \pi/2$ *and* $\delta_p = -0.05$. *The spots indicate the position of the Fourier components for* $p = \pi/80$, $k_s = 0.082$*(red) and* $p = \pi/40$, $k_s = 0.07$ *(blue). The red (blue) components are also seen to be associated with stable (unstable) lattices. The contours spacing is* 0.00075. *The purple curve corresponds to a circle centered about the maximum growth rate to illustrate the asymmetry of the instability region.*
(b) Existence domain of stable solutions on the (k_s, E_p) *plane, for* $k_p = \pi/2$, $\delta_p = -0.05$ *(blue) and* $k_p = 1.5$, $\delta_p = -0.25$ *(red) where the solid lines denote the region boundaries, whilst the dashed lines indicated the curves for* $p = \pi/80$, $\pi/40$ *and* $\pi/20$ *from the lowest curve.*

the asymmetry of the instability regimes for the homogeneous solution is further demonstrated, through the equally spaced contours and the bounding circle. At small p, these contours become increasingly circular. As a result, we have the equation

$$\Im(\lambda(k_{opt} - p, \sqrt{3}p)) = \Im(\lambda(k_{opt} + 2p, 0))$$

which one solves to obtain k_{opt} for a given set of parameters. When this condition is satisfied, one has an approximate boundary for the existence of stable lattices as shown in figure 4-21(b). Through this, it is seen that as the size of the lattice decreases (corresponding to an increase in p), stable lattice solutions require increasingly larger signal momentum, such that $k_s \to k_p$ whilst remaining within the parametric scattering regime.

4.4.6 Vortex Drift Velocity

In the cases of either a single vortex or a vortex lattice, one observes a drift of the pattern in the direction of the pump momentum, due to the non-flat dispersion at the points. Working under the approximations, $t_s = v_s = u_s = w_s$ and $p \ll |k_p - k_s|$, the group velocity of this drift is given through

$$\begin{aligned} \vec{v}_g^{(u)} &\equiv \nabla Re(\lambda(\vec{k}_s - \vec{k}_p)) \\ &= \frac{\vec{v}_i + \vec{v}_s}{2} - |\Psi_0|^2 \left(\vec{v}_i \frac{\Omega_i}{(1+\Omega_i^2)} + \vec{v}_s \frac{\Omega_s}{(1+\Omega_s^2)} \right) \end{aligned} \tag{4.53}$$

where $\vec{v}_i = \nabla\Omega(\vec{k}_i)$, $\vec{v}_s = \nabla\Omega(\vec{k}_s)$ are group velocities of the idler and signal polaritons, respectively, whilst the other parameters are defined through the system of equations 3.19, which are reproduced below

$$\begin{array}{ccc} \bar{\gamma} = \frac{\gamma_{ph}+\gamma_e}{2} & \gamma_d = \frac{\gamma_{ph}-\gamma_e}{2} & \epsilon_\alpha = (\Omega_i^2 - 1)/\alpha^2 \\ \epsilon_\beta = (\Omega_s^2 - 1)/\beta^2 & \tilde{\Omega}_i = \Omega_i + 2|\Psi_0|^2/\alpha^2 & \tilde{\Omega}_s = \Omega_s + 2|\Psi_0|^2/\beta^2 \\ & \alpha^2 = 1 + \Omega_i^2 & \beta^2 = 1 + \Omega_s^2 \\ & \Omega_i(\vec{\kappa}) = \Omega(\vec{k}_p + \vec{\kappa}) & \Omega_s(\vec{\kappa}) = \Omega(\vec{k}_p - \vec{\kappa}) \end{array} \tag{4.54}$$

Equation 4.53 provides the drift velocity of the background roll or a single vortex, when evaluated at k_s. It does not however provide the net drift velocity of the lattice, for that one must evaluated this expression for each Fourier component separately and take the average. This averaging allows one to allow for the differing gradients at the respective Fourier components, which is significant for large p or Fourier components that are not aligned symmetrically about the x-axis. For the honeycomb vortex lattice at the parameters provided in figure 4-14, the analytical value of this drift velocity is 0.0886, whilst the numerical value is 0.0923 and one can see that there is good agreement between the analytics and numerics. For a typical Rabi frequency $\hbar\Omega_R = 4.99meV$, this drift corresponds to approximately $1.8\mu m/ps$.

4.5 Square Vortex Lattices

By the introduction of an additional beam, such that the four beams exist at 90° to each other, one can generate a square vortex lattice of the form

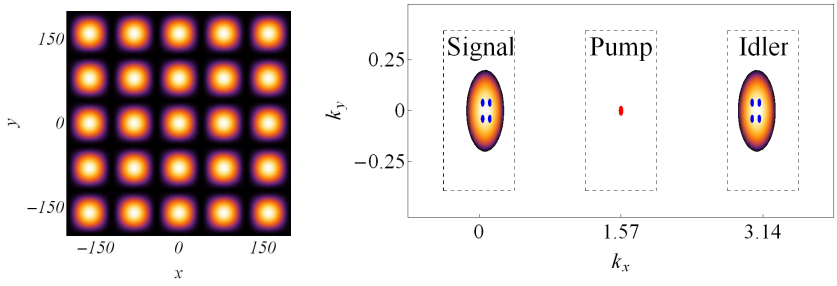

Figure 4-22: *(Left) Schematic of the square lattice arrangement. (Right)Schematic diagram illustrating the distribution of Fourier components associated with the square lattice structure.*

$$P_{vortex} = v_s e^{ipx+ipy} + u_s e^{-ipx+ipy} + w_s e^{-ipx-ipy} + q_s e^{ipx-ipy} \tag{4.55}$$

where $|v_s| \approx |w_s| \approx |u_s| \approx |q_s| = E_p s$ and probe momenta, $|p| << |k_p|$, such that it belongs to the parametric instability domain about $k = 0$, in figure 3-1. This arrangement of probe beams serves to create a regular square lattice in position-space consisting of alternating vortices and antivortices. In momentum space, this lattice corresponds to four spots located at the corners of a square orientated about the pump axis within the signal and idler bands, as can be observed within figure 4-22 in a direct analogy to figure 4-11.

4.5.1 The Lattice Equation

Following the same method as was utilized for honeycomb lattices, we let

$$A = A_p e^{ik_p x - i\delta_p t} + A_s e^{ik_s x - i\delta_s t} + A_i e^{ik_i x - i\delta_i t} \tag{4.56}$$

$$\psi = Q_p e^{ik_p x - i\delta_p t} + Q_s e^{ik_s x - i\delta_s t} + Q_i e^{ik_i x - i\delta_i t} \tag{4.57}$$

and

$$\begin{aligned} A_s &= t_s e^{ipx+ipy} + u_s e^{-ipx+ipy} + v_s e^{-ipx-ipy} + w_s e^{ipx-ipy} \\ A_i &= t_i e^{-ipx-ipy} + u_i e^{ipx-ipy} + v_i e^{ipx+ipy} + w_i e^{-ipx+ipy} \end{aligned} \tag{4.58}$$

where we have again made the approximations $p \ll |k_p - k_s|$ and $t_s = u_s = v_s = w_s$. This arrangement of Fourier components serves to produce a square lattice of alternating vortices and antivortices. We substitute into the equation for the exciton component as before to obtain

$$\begin{aligned} 0 &= (\alpha_s + 9|a_s|^2 + 2|\psi_p|^2 + 18|a_i|^2)a_s + \psi_p^2 a_i^* && (4.59)\\ 0 &= (\alpha_i + 9|a_i|^2 + 2|\psi_p|^2 + 18|a_s|^2)a_i + \psi_p^2 a_s^* && (4.60)\\ 0 &= (\alpha_p + |\psi_p|^2 + 8|a_s|^2 + 8|a_i|^2)\psi_p + 8a_s a_i \psi_p^* - \beta E_p && (4.61) \end{aligned}$$

from which, one obtains expressions for the signal and idler

$$\begin{aligned} |Q_i|^2 &= \frac{\Im(\alpha_s)}{\Im(\alpha_i)}|Q_s|^2 = \kappa|Q_s|^2 \\ |Q_s|^2 &= \frac{\Re(\alpha_s) - \Re(\alpha_i)\kappa + 2|Q_p|^2(1-\kappa)}{9(\kappa^2-1)} \end{aligned} \qquad (4.62)$$

The dependence of the pump branch on δ_s

$$\begin{aligned} 0 &= a|Q_p|^4 + b|Q_p|^2 + c \\ c &= \Im(\alpha_s)\Im(\alpha_i)(1-\kappa^2)^2 + \kappa[2(\Re(\alpha_s) - \kappa\Re(\alpha_i)) + \Re(\alpha_s)\kappa - \Re(\alpha_i)]^2 \\ b &= 4\kappa(1-\kappa)[2(\Re(\alpha_s) - \Re(\alpha_i)\kappa) + \Re(\alpha_s)\kappa - \Re(\alpha_i)] \\ a &= -(1-\kappa)^4 \end{aligned} \qquad (4.63)$$

and the phase relation

$$\frac{1}{|\psi_P|}\frac{iE_p e^{-i\arg(Q_p)}}{\delta_p + i\gamma_{ph} - k_p^2} = \alpha_p + |\psi_p|^2 + 8|\psi_s|^2 + 8|\psi_i|^2 + 2|\psi_s||\psi_i|e^{-i\omega} \qquad (4.64)$$

These equations allow one to obtain the curves of the signal and idler associated with a square lattice solution, which are shown in figure 4-23. Through this, it is seen that as for honeycomb lattices, the square lattice begins and ends at the same pump strengths as the roll branch, with the signal and idler components being further reduced from those for the honeycomb branch.

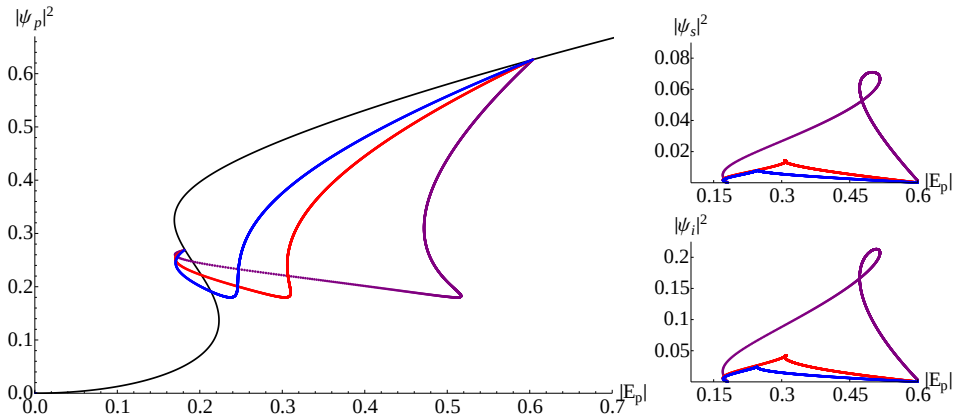

Figure 4-23: *Plots of (Left) pump exciton density, $|\psi_p|^2$, (Top Right) $|\psi_s|^2$ and (Lower Right) $|\psi_i|^2$ against E_p, for $k_p = \pi/2$, $\delta_p = -0.05$ and $\gamma_{ph} = \gamma_e = 0.1$. The purple (blue) line display the solution in the presence of a roll (square) pattern, whilst the red line displays the honeycomb branch, for comparison.*

4.5.2 Lattice Evolution and Melting

As for hexagonal lattices, we consider a lattice positioned such that all Fourier components possess an equal gain. The signal field is shown in figures 4-25(a) and (b), whilst figure 4-24 displays the phases of the signal and idler. Lattices with signal momentum shifted left and right with respect to the maximum of the instability region are shown in figures 4-25(c) and (d) respectively, where it is seen that provided the growth rate associated with each component is equal, one can form a stable square lattice, as was the case for the honeycomb lattices.

When one seeds the lattice one either side of this optimal position, one witnesses identical behavior in the formation of vortex lines (shown in figure 4-25(c)). This behavior mirrors that observed previously in figure 4-19(b). This change in behavior is due to the symmetry of the seed in momentum space along the pump axis.

4.5.3 Existence Domain of stable solutions

As for our consideration of the stability of honeycomb lattices in section 4.4.5, we now examine the stability of square lattices. As before, a set of (E_p, k_s) exists such that the instability growth rates associated with each component are equal, when one is working in the parametric scattering regime. These square lattices are observed to be stable over a range of pump strengths and lattice spacings, as observed within figure 4-26, wherein one notes that unlike for the honeycomb lat-

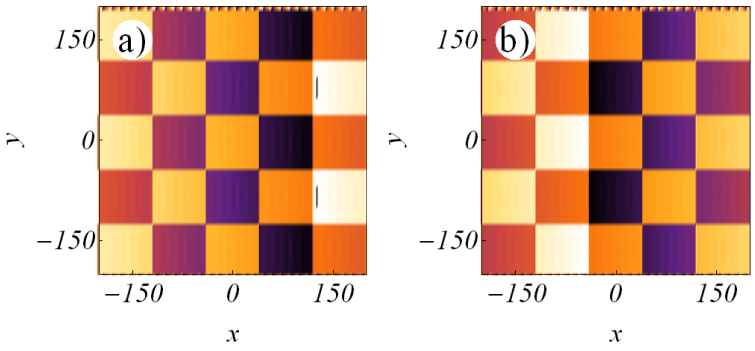

Figure 4-24: *Plots of $arg(\psi)$, evaluated for $\delta_p = -0.05$, $k_p = \pi/2$, $E_p = 0.56$, $k_s = 0.07$ and $\gamma_{ph} = \gamma_e = 0.1$, growing from a seed vortex for a flat pump configuration, for the (a) signal and (b) idler at $t = 25$.*

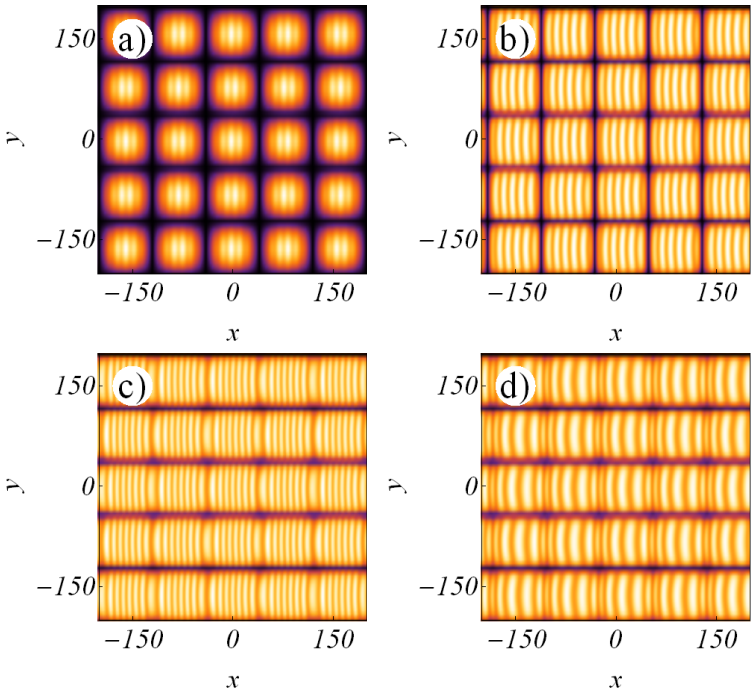

Figure 4-25: *Intensity of the signal component of E corresponding to a square vortex lattice generated by a seed pulse, for the plane wave pump, with $E_p = 0.56$, $k_p = \pi/2$, $\delta_p = -0.05$ and $p = \pi/80$ at (a) $t = 5$ and (b)$t = 100$ for $k_s = 0.07$. Whilst the shifted images are seen for the signal field in (c) $t = 100$ and $k_s = 0$, and (d) $t = 100$ and $k_s = 0.14$.*

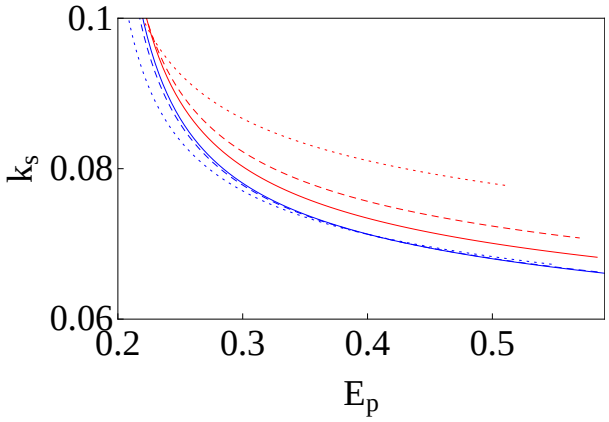

Figure 4-26: *Existence domain of stable solutions on the (k_s, E_p) plane, for $k_p = \pi/2$ and $\delta_p = -0.05$ where the solid lines denote the region boundaries, whilst the dashed lines indicated the curves for $p = \pi/80$ (solid), $p = \pi/40$ (dashed) and $p = pi/20$ (dotted) for both square (blue) and honeycomb (red) lattices.*

tice, there is significantly less variance in k_{opt} with p, close to the upper instability boundary. This dramatic change in the form of this existence domain is directly related to the asymmetry of the instability domain associated the homogeneous solution. It results in a shift of the optimum signal momentum away from the pump at larger lattice constants, which means that for square lattices, k_{opt} tends towards a constant value for arbitrary $p < p_{max}$ where the particular value of k_{opt} corresponds with position of the instability domain maxima as can be witnessed in figure 4-26.

4.6 Other forms of Vortex Lattice

Through the study of honeycomb and square lattices, it is simple to extrapolate to arbitrary lattices. This can be achieved because the square and honeycomb lattices are the simplest lattices that can be arranged symmetrically and asymmetrically with respect to the pump axis, and thus their behavior will cover the main melting scenarios exhibited in the system. From which, it follows that arbitrary polariton vortex lattices will be stable when the growth rates associated with all components are equal. When this is not the case, the form of the resulting instability is dependent on the number and position of the Fourier components, along with the distance of the averaged probe momentum from the line of stability.

For an even number of components arranged symmetrically about the average

probe momentum, the instability develops in an identical manner, regardless of the position of the probe momenta, to form lines of vortices orientated parallel to the pump direction. When there are an odd number of components, in addition to the possibility of vortex line formation, one can also observed annihilation of vortex-antivortex pairs.

4.7 Summary

Through perturbative, variational and direct numerical modeling, it has been observed that there is a minimum potential dependent value of the detuning parameter for vortices to exist in the stationary system. An increase in the strength of the potential or an increase in the winding number of the vortex results in the cut-off shifting to progressively higher energies, while the number of particles contained within the vortex is observed to increase, as the detuning parameters tend to zero.

The stability of the stationary system in the absence of loss or gain has been analyzed. It is seen that $m = 0$ and $m = 1$ vortices are stable over the entire range of possible detuning parameters, and a large range of potential strengths. In contrast to this, higher order vortices with $m = n$ have been observed to be unstable over the whole range, and decay into n $m = 1$ vortices. This stability analysis has been verified through propagation over long periods.

In the presence of loss and gain, the model has been observed to permit the spontaneous formation of localized vortex-antivortex pairs in addition to pattern formation, when the system is pumped at energies within the region of parametric instability, along the upper branch of the bistability diagram.

In the presence of a single seeding vortex with a momentum that corresponds to the signal band of the system, vortex-antivortex pairs are observed to form within signal and idler bands, such that the pair is pinned to the location of the seed. This localization is seen to result from the Gaussian pump acting as an effective potential for the signal and idler bands. The signal(idler) vortices (antivortices) are seen to remain be stable and travel towards the boundaries of the excitation region with a velocity determined by the pump momentum. Whilst, if one introduces a $m = n$ vortex seed, one observes the vortex splitting into n $m = 1$ vortices and similar behavior for the antivortex.

For the honeycomb solutions, it has been seen that it is possible to obtain a quasi-stable lattice. These stable solutions can only be achieved when the growth

rates associated with the Fourier components that compose the lattice are equal. Otherwise, it is observed that adjacent vortices and antivortices merge. For non-flat pumps, the same effects are observed away from the boundaries. These effects have also been observed for square lattices. From which, it appears reasonable to conclude that provided one can position the Fourier components such that they possess equal gain, lattices of arbitrary shapes can be supported. Finally, we discussed the origin of the drift velocity for the patterns.

CHAPTER 5

Polarization effects on Solitons and Vortices

In the previous chapters, we have discussed the behavior of vortices and lattices in a scalar exciton-polariton condensate, however one of the most significant features of polaritons is the presence of an additional degree of freedom due to the presence of spin. Potentially, this feature can be combined with the long soliton lifetime to allow for potential applications in spin-optronic devices, as it provides an additional means to store or transmit information.

In spin-dependent exciton-polariton systems, the behavior of vortices has been studied extensively[51, 144, 170]. Through the works of Borgh *et al.* [18], it is seen that in the absence of a $TE - TM$ splitting, vortices and lattices can persist in each of the polarization components independently, whilst exhibiting properties that are typical of vortices in other media.

In contrast to the many studies into the effects of arbitrarily polarized pumps on the dynamics of exciton-polariton vortices, there have been relatively few studies on polarized solitons[126, 9], which theoretically and experimentally illustrate the nucleation of dark solitons and vortex-antivortex pairs from a defect. Although experimental studies of solitons have been rare, there have been related studies such as the work by Amos *et al.* [8, 2]. These experimental studies demonstrate that spin polariton bullets of differing polarizations can be observed within the system as a potential realization of polariton neurons for all-optical integrated circuits.

Initially, we discuss an extended model that accounts for polarization and spin

effects, wherein we determine the eigenvalues of the linearized system, and discuss the stability of the homogeneous system. Following which, we briefly extend the discussion of vortices from an earlier chapter to include the effects of pump polarization on such a system. After which we proceed to discuss soliton dynamics under an arbitrarily polarized pumping regime, and examine the possibility of switching between spin states under a linearly polarized pump. Except for the scalar case of circularly polarized solitons, the solitons we discuss in this chapter are vector solitons. These have been studied extensively in fibers, where it is seen that bright and dark solitons can couple to form a vector soliton[87].

In this chapter, we finally relax the restrictions on the detuning parameters and allow $\delta_p \neq \delta_e$. This relaxation is necessary to provide a better fit with experimental data, as it is difficult to fabricate large microcavities with coincident resonances. Some components of the discussion about solitons in section 5.7 have been mentioned in reference [161].

5.1 The model

To extend the model to study polarization, one adapts the kinetic energy terms [76, 104, 122] to take the form

$$T_{ij} \cdot \begin{pmatrix} E_r \\ E_l \\ \psi_r \\ \psi_l \end{pmatrix} = i \begin{pmatrix} \nabla^2 & \eta\nabla^2 & 0 & 0 \\ \eta\nabla^2 & \nabla^2 & 0 & 0 \\ 0 & 0 & 0 & 0 \\ 0 & 0 & 0 & 0 \end{pmatrix} \cdot \begin{pmatrix} E_r \\ E_l \\ \psi_r \\ \psi_l \end{pmatrix} \tag{5.1}$$

where η governs the parabolic splitting between TE and TM modes [51, 123], and we note that as in the previous sections we assume the exciton mass, and thus the corresponding splitting terms are negligible. One now introduces a magnetic field, χ to allow one to distinguish between the polarizations, where a and b are the fractions of the pump intensity associated with the $|E_r\rangle$ and $|E_l\rangle$ fields respectively. Lastly, we replace the interaction term [101], $|\psi|^2$ with $(\alpha_1 - \alpha_2)|\psi_{r,l}|^2 + \alpha_2|\psi_{l,r}|^2$, where $\alpha_{1,2}$ describe the interaction strength between excitons with parallel and anti-parallel spin components [135, 144, 192]. This interaction is strongly anisotropic, where a repulsion is experienced between polaritons possessing the same helicity, while a weak attraction is experienced by polaritons with opposing polarization. The right handed circularly polarized

state is associated with polaritons in the spin up state[121, 132, 160]. Additionally, one allows the cavity and exciton detuning terms to vary independently, and thus ones arrives at the system of equations

$$\begin{aligned}
\frac{d}{dt}E_r - i\nabla^2 E_r - i\eta\nabla^2 E_l + (\gamma_{ph} - i\delta_p)\, E_r &= i\Omega_R\psi_r + aE_p e^{ik_p x} \\
\frac{d}{dt}E_l - i\nabla^2 E_l - i\eta\nabla^2 E_r + (\gamma_{ph} - i\delta_p)\, E_l &= i\Omega_R\psi_l + bE_p e^{ik_p x} \\
\frac{d}{dt}\psi_r + \left(\gamma_e - i\delta_e - i\chi + i\alpha_0|\psi_r|^2 + i\alpha_2|\psi_l|^2\right)\psi_r &= i\Omega_R E_r \\
\frac{d}{dt}\psi_l + \left(\gamma_e - i\delta_e + i\chi + i\alpha_0|\psi_l|^2 + i\alpha_2|\psi_r|^2\right)\psi_l &= i\Omega_R E_l
\end{aligned} \tag{5.2}$$

which governs the behavior of the exciton-polariton system accounting for spin and polarization effects, for $\alpha_0 = (\alpha_1 - \alpha_2)$.

It is worth noting that the splitting terms are modeled in this manner to illustrate the explicit momentum dependence, while in reality, there will be additional contributions through a spin orbit splitting, that produces an additional momentum dependent term, and a birefringence that could be modeled through a shift of the left and right detuning parameters. These terms control the spin-orbit coupling [76] between the left and right handed polarizations, which can be attached to the spin-orbit coupling between spin down and up photons. The corresponding terms for the excitons are neglected, as they are significantly smaller than exciton mass, which is already small.

5.2 The Dispersion Relation

First, we examine the effects of polarization upon the dispersion relation, in the absence of an external magnetic field. To begin, we insert the one dimensional traveling wave solutions of the form

$$\begin{aligned}
E_r &= A_r e^{ik_p x}, \quad E_l = A_l e^{ik_p x + i\mu t} \\
\psi_r &= B_r e^{ik_p x}, \quad \psi_l = B_l e^{ik_p x + i\mu t}
\end{aligned} \tag{5.3}$$

into equation 5.2, whilst neglecting nonlinearity to express the system as

$$\mu\vec{A} = \hat{M}\vec{A}$$

$$\begin{aligned}
\vec{A}^T &= \begin{pmatrix} E_r & E_l & \psi_r & \psi_l \end{pmatrix}^T \\
\hat{M} &= \begin{pmatrix} i\gamma_{ph} - k_p^2 + \delta_p & -\eta k_p^2 & \Omega_R & 0 \\ -\eta k_p^2 & i\gamma_{ph} - k_p^2 + \delta_p & 0 & \Omega_R \\ \Omega_R & 0 & \delta_e + i\gamma_e & 0 \\ 0 & \Omega_R & 0 & \delta_e + i\gamma_e \end{pmatrix}
\end{aligned} \tag{5.4}$$

and thus we determine that the eigenvalues are

$$\begin{aligned}
2\mu_{-1} &= -\sqrt{4\Omega_R^2 + \left(k_p^2(\eta+1) + \Delta + i\left(\gamma_e - \gamma_{ph}\right)\right)^2} + i(\gamma_{ph} + \gamma_e) \\
&- k_p^2(\eta+1) + 2\delta_p + \Delta \\
2\mu_{-2} &= -\sqrt{4\Omega_R^2 + \left(k_p^2(\eta-1) + \Delta - i\left(\gamma_e - \gamma_{ph}\right)\right)^2} + i(\gamma_{ph} + \gamma_e) \\
&+ k_p^2(\eta-1) + 2\delta_p + \Delta \\
2\mu_{+1} &= \sqrt{4\Omega_R^2 + \left(k_p^2(\eta+1) + \Delta + i\left(\gamma_e - \gamma_{ph}\right)\right)^2} + i(\gamma_{ph} + \gamma_e) \\
&- k_p^2(\eta+1) + 2\delta_p + \Delta \\
2\mu_{+2} &= \sqrt{4\Omega_R^2 + \left(k_p^2(\eta-1) + \Delta - i\left(\gamma_e - \gamma_{ph}\right)\right)^2} + i(\gamma_{ph} + \gamma_e) \\
&+ k_p^2(\eta-1) + 2\delta_p + \Delta
\end{aligned}$$

where $\Delta = \delta_e - \delta_p$, and it is seen that there is a splitting of both upper (μ_{+i}) and lower (μ_{-i}) branches. As we discussed for the spin-less system in section 2.4, we require that $Re[\mu_{\pm i}] = 0$ which provides the dispersion relation

$$\begin{aligned}
\delta_p &= \frac{\sqrt{4\Omega_R^2 + (\eta \pm 1)^2 k_p^4} + (1 \pm \eta)k_p^2 - \Delta}{2} \\
\delta_p &= \frac{-\sqrt{4\Omega_R^2 + (\eta \pm 1)^2 k_p^4} + (1 \pm \eta)k_p^2 - \Delta}{2}
\end{aligned} \tag{5.5}$$

for the upper and lower branches respectively for $(+)$ left and right-handed $(-)$ circular polarizations. Thus the left-handed component that is attached to a spin down exciton (wherein we have anti-parallel electron-hole spins) has a lower energy in the presence of $TE - TM$ splitting, while recalling the dispersion relation for the spinless system is given by

$$\delta_p = \frac{1}{2}(k_p^2 - \Delta \pm \sqrt{k_p^4 + 4\Omega_R^2}) \tag{5.6}$$

By comparison of these relations it is evident that the polarized branches follow the unpolarized branches, and that the separation of the branches is negligible for small values of η. At larger values of η, however the TM dispersion is seen to become increasingly flattened, whilst the dispersion of the TE mode is seen to be strengthened, which can be observed within figure 5-1 of $\eta = 0.25$. In which, it is seen that the separation between the TE and TM branches is negligible while k_p tends toward zero and at very large momentum. As a result, the maximum separation along the lower branch is achieved at a momentum that is just above the inflection point of the dispersion curve, wherein the exact position is dependent on the particular value of η. Now, we return to equation 5.4 and determine the eigenvectors for a fields orientated along the x-axis with a momentum, k_p to obtain

$$\begin{aligned}
\vec{A_1}^T &= \begin{pmatrix} \Phi_{+1} & \Phi_{+1} & 1 & 1 \end{pmatrix} \\
\vec{A_2}^T &= \begin{pmatrix} -\Phi_{-1} & \Phi_{-1} & -1 & 1 \end{pmatrix} \\
\vec{A_3}^T &= \begin{pmatrix} \Phi_{+2} & \Phi_{+2} & 1 & 1 \end{pmatrix} \\
\vec{A_4}^T &= \begin{pmatrix} -\Phi_{-2} & \Phi_{-2} & -1 & 1 \end{pmatrix}
\end{aligned} \tag{5.7}$$

where

$$\begin{aligned}
\Phi_{+1} &= \frac{-\sqrt{4\Omega_R^2 + \left((\eta+1)k_p^2 - 2i\gamma_d + \Delta\right)^2} + 2i\gamma_d - (\eta+1)k_p^2 + \Delta}{2\Omega_R} \\
\Phi_{+2} &= \frac{-\sqrt{4\Omega_R^2 + \left((\eta-1)k_p^2 - 2i\gamma_d + \Delta\right)^2} + 2i\gamma_d + (\eta-1)k_p^2 + \Delta}{2\Omega_R} \\
\Phi_{-1} &= \frac{\sqrt{4\Omega_R^2 + \left((\eta+1)k_p^2 - 2i\gamma_d + \Delta\right)^2} + 2i\gamma_d - (\eta+1)k_p^2 + \Delta}{2\Omega_R} \\
\Phi_{-2} &= \frac{\sqrt{4\Omega_R^2 + \left((\eta-1)k_p^2 - 2i\gamma_d + \Delta\right)^2} + 2i\gamma_d + (\eta-1)k_p^2 + \Delta}{2\Omega_R}
\end{aligned} \tag{5.8}$$

for $\Delta = \delta_p - \delta_e$ and $\gamma_d = (\gamma_{ph} - \gamma_e)/2$, where the eigenvectors are normalized such that the component, $\psi_l = 1$ so that it is readily apparent that on the lower branch, the eigenvalues Φ_{-i} tend towards zero at high momentum such that they are mostly excitonic. The eigenstates of the linear system coincide with the linear polarization vectors, in the limit that η tends to zero. These polarization vectors

are favored within ideal microcavities in the absence of an external magnetic field as predicted by Laussy *et al.* [99].

The TE mode is polarized in the cavity plane perpendicular to the in-plane pump momentum, while TM mode has one component that is aligned perpendicular to the cavity plane and another that is aligned in the cavity plane with the pump momentum. Generally, TE photonic and excitonic modes can be represented through $|E_y\rangle = i(|E_r\rangle - |E_l\rangle)$, however the equivalent transformation is only approximate for the TM modes as the nonzero perpendicular component does not couple to excitons. For large pump momentum, it is observed that a circularly polarized pump can excite intracavity modes possessing an approximately circular polarization. Correspondingly, the longitudinal component of the TM mode is negligible and thus it is reasonable to assume that the TM and TE modes can be approximately expressed through

$$|E_x\rangle = |E_r\rangle + |E_l\rangle \quad |E_y\rangle = i(|E_r\rangle - |E_l\rangle) \tag{5.9}$$

where $|\phi_r\rangle$ and $|\phi_l\rangle$ correspond to circular polarizations, while $|\phi_x\rangle$ and $|\phi_y\rangle$ correspond to polarizations that are collinear (TM) and perpendicular (TE) to the cavity plane. Thus, it is seen that the TM and TE polarizations are the preferred cavity modes, in which basis we can re-express the one-dimensional system as

$$\begin{aligned}
\frac{d}{dt}E_x - i(1+\eta)\frac{d^2}{dx^2}E_x + (\gamma_{ph} - i\delta_p)E_x &= i\Omega_R\psi_x + (a+b)E_p e^{ik_p x} \\
\frac{d}{dt}E_y - i(1-\eta)\frac{d^2}{dx^2}E_y + (\gamma_{ph} - i\delta_p)E_y &= i\Omega_R\psi_y + (a-b)E_p e^{ik_p x} \\
\frac{d}{dt}\psi_x + (\gamma_{ph} - i\delta_p)\psi_x + \frac{i}{4}((1+V)|\psi_x|^2 + 2|\psi_y|^2)\psi_x & \\
-\frac{i}{4}(1-V)\psi_x^*\psi_y^2 &= i\Omega_R E_x + i\chi\psi_y \\
\frac{d}{dt}\psi_y + (\gamma_{ph} - i\delta_p)\psi_y + \frac{i}{4}((1+V)|\psi_y|^2 + 2|\psi_x|^2)\psi_y & \\
-\frac{i}{4}(1-V)\psi_y^*\psi_x^2 &= i\Omega_R E_y + i\chi\psi_x
\end{aligned} \tag{5.10}$$

where $V = \alpha_2/\alpha_0$. Again, we note that the vortices, vortex lattices and solitons discussed in the previous chapters correspond to the right or left handed circularly polarized solutions in the limit of weak interactions between excitons of opposite spin, no external magnetic field in the absence of $TE - TM$ splitting.

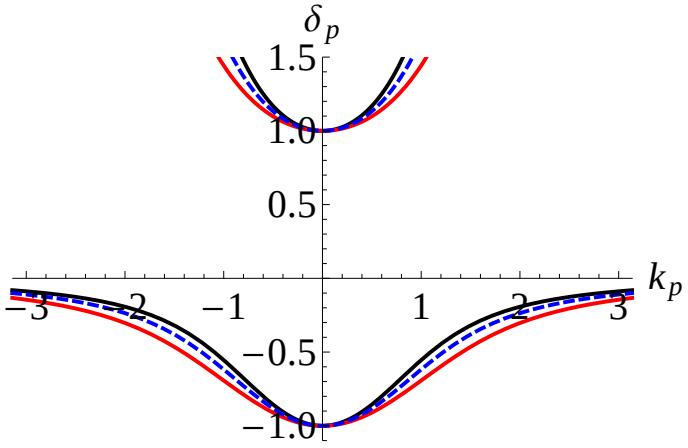

Figure 5-1: *Dispersion relation for polaritons with a TE (black) and TM (red) polarization for $\eta = 0.25$. The dashed line indicates the dispersion curve in the absence of polarization.*

5.3 Homogeneous Solutions

Now, we proceed to analyze the homogeneous solutions in the left-right basis, through the substitutions, $E_{l,r} = A_{l,r}e^{ik_p x}$, $\psi_{l,r} = B_{l,r}e^{ik_p x}$. We work in this basis as it provides a significantly clearer demonstration of the existence of multiple bistability regimes than is observable in the $TE-TM$ basis. We begin by solving the first pair of equations in system 5.2 for A_r and A_l to obtain

$$\begin{aligned} A_r &= \frac{iE_p(-bk_p^2\eta + a(k_p^2-\delta_p) - ia\gamma_{ph})}{(-(k_p^2-\delta_p)^2 + k_p^4\eta^2 + 2i(k_p^2-\delta_p)\gamma_{ph} + \gamma_{ph}^2)} \\ &+ \frac{(B_l k_p^2\eta - B_r(k_p^2-\delta_p) + iB_r\gamma_{ph})\Omega_R}{-(k_p^2-\delta_p)^2 + k_p^4\eta^2 + 2i(k_p^2-\delta_p)\gamma_{ph} + \gamma_{ph}^2} \\ A_l &= \frac{-iE_p(ak_p^2\eta + b(-k_p^2+\delta_p) + ib\gamma_{ph})}{(-(k_p^2-\delta_p)^2 + k_p^4\eta^2 + 2i(k_p^2-\delta_p)\gamma_{ph} + \gamma_{ph}^2)} \\ &+ \frac{(B_r k_p^2\eta + B_L(-k_p^2+\delta_p) + iB_l\gamma_{ph})\Omega_R}{-(k_p^2-\delta_p)^2 + k_p^4\eta^2 + 2i(k_p^2-\delta_p)\gamma_{ph} + \gamma_{ph}^2} \end{aligned} \tag{5.11}$$

which one substitutes into the remaining equations and multiplies by their conjugates to obtain

$$0 = \frac{\left(\eta^2 |B_L|^2 k_p^4 + |B_R|^2 \left(\left(k_p^2-\delta_p\right)^2 - \gamma_{ph}^2\right)\right)\Omega_R^4}{\left(\gamma_{ph}^2 + \left((\eta^2+1)k_p^4 - 2\delta_p k_p^2 + \delta_p^2\right)\right)^2}$$

$$
\begin{aligned}
&+ \quad |B_R|^2 \left(\alpha_2^2 |B_L|^4 - 2(\delta_e + \chi)\alpha_2 |B_L|^2 + \delta_e^2 + \chi^2\right) \\
&+ \quad |B_R|^2 \left(|B_R|^4 \alpha_0^2 + \gamma_e^2 + 2\delta_e\chi - 2|B_R|^2 \alpha_0 \left(-\alpha_2 |B_L|^2 + \delta_e + \chi\right)\right) \\
&+ \quad \frac{E_p^2 \left(\left(b\eta k_p^2 - a\left(k_p^2 - \delta_p\right)\right)^2 + a^2\gamma_{ph}^2\right)\Omega_R^2}{\left(\gamma_{ph}^2 + \left(\left(\eta^2+1\right)k_p^4 - 2\delta_p k_p^2 + \delta_p^2\right)\right)^2}
\end{aligned}
\tag{5.12}
$$

and

$$
\begin{aligned}
0 \quad = \quad & \frac{\left(\eta^2 |B_R|^2 k_p^4 + |B_L|^2 \left(\left(-k_p^2 + \delta_p\right)^2 + \gamma_{ph}^2\right)\right)\Omega_R^4}{\left(\gamma_{ph}^2 + \left(\left(\eta^2+1\right)k_p^4 - 2\delta_p k_p^2 + \delta_p^2\right)\right)^2} \\
&+ \quad |B_L|^2 \left(|B_R|^4 \alpha_2^2 + \gamma_e^2 - 2\delta_e\chi + 2(\chi - \delta_e)|B_R|^2 \alpha_2\right) \\
&+ \quad 2|B_L|^2 \left(\alpha_0 \left(\alpha_2 |B_R|^2 - \delta_e + \chi\right)|B_L|^2 + \delta_e^2 + \chi^2 + \alpha_0^2 |B_L|^4\right) \\
&+ \quad \frac{E_p^2 \left(\left(a\eta k_p^2 + b\left(-k_p^2 + \delta_p\right)\right)^2 + b^2\gamma_{ph}^2\right)\Omega_R^2}{\left(\gamma_{ph}^2 + \left(\left(\eta^2+1\right)k_p^4 - 2\delta_p k_p^2 + \delta_p^2\right)\right)^2}
\end{aligned}
\tag{5.13}
$$

From this pair of equations, one can obtain the multistability curves for $|\psi_r|$ and $|\psi_l|$ against E_p, wherein one can see that for a system pumped with a circularly polarized beam, one retrieves a curve that follows the unpolarized system. However, when one works with a linearly polarized beam, in the region where the unpolarized system would be bistable, it is seen that two additional elliptically polarized branches exist. This is in agreement with the work done by Gippius *et al.* [54, 159] as illustrated in figure 5-2 shown for $\eta = 0$, where the TE and TM modes coincide. When this is not the case, it is seen in figure 5-3 that the solutions no longer coincide, whilst the bistable regions are generally shifted towards a higher pump intensity. It is worth noting that even the small splitting ($\eta = 0.01$) results in the change in the size of the bistability domains such that the region that is misaligned with the dominant circularly polarized pump component will notably expand, whilst the separation of the branches of the dispersion relation at this location is relatively small. At high intensities, the solution tends toward a linear polarization for an arbitrary pump polarization.

To study the existence conditions for these additional side branches, we eliminate the terms E_r and E_l through the system 5.12, take the absolute squared value and solve for E_p to obtain

$$
E_p \quad = \quad -ia_{0,r}(\alpha_0|B_r|^2 B_r + a_{1,r}B_r + \alpha_2|B_l|^2 B_r - b_1 B_l)
$$

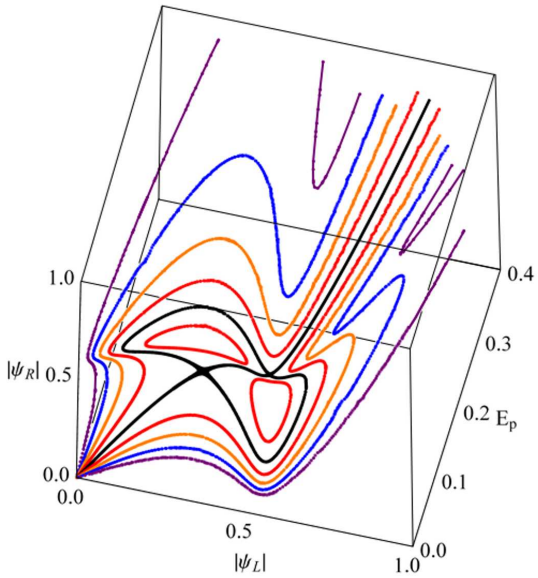

Figure 5-2: *Plot of E_p over the $|\psi_r|-|\psi_l|$ plane for $k_p = 1.02$, $\delta_p = -0.45$, $\delta_e = -0.36$, $\gamma_{ph} = \gamma_e = 0.05$ and $\eta = 0$. The black line corresponds to the solution under TM pumping, while the red lines correspond to a solution under an elliptically polarized pump of the form $0.6|\psi_{r,l}| + 0.4|\psi_{l,r}|$. The successive lines are associated with a change of $0.1|\psi_{r,l}| - 0.1|\psi_{l,r}|$.*

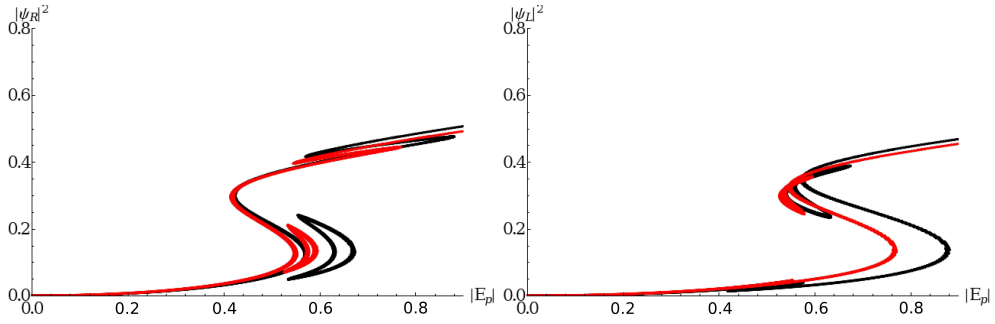

Figure 5-3: *Plot of E_p, as a function of $|\psi_r|^2$, $|\psi_l|^2$, displaying the multistability domain for $\delta_p = \delta_e = -0.05, k_p = \pi/2$ and $\eta = 0.01$, for a pump beam, for (Red) $a = 0.55$, $b = 0.45$ and (Black) $a = 0.55$, $b = -0.45$ modes to the cavity.*

$$E_p = ia_{0,l}(\alpha_0|B_l|^2B_l + a_{1,l}B_l + \alpha_2|B_r|^2B_l - b_1B_r) \tag{5.14}$$

where

$$\begin{aligned}
a_{0,r} &= \frac{\left(2i\gamma_{ph}\left(k_p^2-\delta_p\right)-\left(k_p^2-\delta_p\right)^2+\eta^2k_p^4+\gamma_{ph}^2\right)}{a\Omega_R\left(a\left(k_p^2-\delta_p\right)-ia\gamma_{ph}-b\eta k_p^2\right)}\\
a_{0,l} &= \frac{\left(2i\gamma_{ph}\left(k_p^2-\delta_p\right)-\left(k_p^2-\delta_p\right)^2+\eta^2k_p^4+\gamma_{ph}^2\right)}{b\Omega_R\left(a\eta k_p^2+b\left(-k_p^2+\delta_p\right)+ib\gamma_{ph}\right)}\\
a_{1,\pm} &= -i\gamma_e+\frac{\Omega_R^2\left(k_p^2-\delta_{ph}-i\gamma_{ph}\right)}{2k_p^2\left(\delta_p+i\gamma_{ph}\right)+\left(\eta^2-1\right)k_p^4+\left(\gamma_{ph}-i\delta_p\right)^2}-\delta_e\pm\chi\\
b_1 &= \frac{\eta k_p^2\Omega_R^2}{2k_p^2\left(\delta_p+i\gamma_{ph}\right)+\left(\eta^2-1\right)k_p^4+\left(\gamma_{ph}-i\delta_p\right)^2}
\end{aligned} \tag{5.15}$$

Differentiating this system with respect to $|B_{l,r}|^2$ and demanding they equal zero at the turning points of the system, yields

$$\begin{aligned}
2\alpha_2\Re\left(a_{1,-}\right)|B_r|^2 &+ 2\alpha_0\alpha_2|B_r|^4+|b_1|^2+2\alpha_2^2|B_l|^2|B_r|^2-\alpha_2\left(b_1^*B_rB_l^*-b_1B_lB_r^*\right)=0\\
2\alpha_2\Re\left(a_{1,+}\right)|B_l|^2 &+ 2\alpha_0\alpha_2|B_l|^4+|b_1|^2+2\alpha_2^2|B_l|^2|B_r|^2-\alpha_2\left(b_1^*B_lB_r^*-b_1B_rB_l^*\right)=0\\
4\alpha_0\alpha_2|B_l|^2|B_r|^2 &+ 2\alpha_2\Re\left(a_{1,-}\right)|B_l|^2+4\alpha_0\Re\left(a_{1,-}\right)|B_r|^2+3\alpha_1^2|B_r|^4+|a_{1,-}|^2\\
&- \alpha_0(b_1^*B_rB_l^*+b_1B_lB_r^*)+\alpha_2^2|B_l|^4=0\\
4\alpha_0\alpha_2|B_l|^2|B_r|^2 &+ 2\alpha_2\Re\left(a_{1,+}\right)|B_r|^2+4\alpha_0\Re\left(a_{1,+}\right)|B_l|^2+3\alpha_1^2|B_l|^4+|a_{1,+}|^2\\
&- \alpha_0(b_1B_rB_l^*+b_1^*B_lB_r^*)+\alpha_2^2|B_r|^4=0
\end{aligned} \tag{5.16}$$

After elimination of the complex terms through substitution, we solve the resulting pair of simultaneous equations to find

$$\begin{aligned}
|B_l|^2 &= \frac{-2\alpha_2^2\Re\left(a_{1,+}\right)t_+\pm\sqrt{\alpha_2^3t_+\left(3\alpha_0|b_1|^2-2\alpha_2\Im\left(a_{1,+}\right)^2\right)^2}}{2\alpha_2^3t_+}\\
|B_r|^2 &= \frac{-2\alpha_2^2\Re\left(a_{1,-}\right)t_-\pm\sqrt{\alpha_2^3t_-\left(3\alpha_0|b_1|^2-2\alpha_2\Im\left(a_{1,-}\right)^2\right)^2}}{2\alpha_2^3t_-}
\end{aligned} \tag{5.17}$$

with

$$t_\pm = \alpha_0|b_1|^2-\alpha_2\Im\left(a_{1,(\pm)}\right)^2 \tag{5.18}$$

through which, we see that the system is bistable when either of the two conditions

$$t_+ \geq 0, \quad t_- \geq 0 \tag{5.19}$$

is satisfied, and it is noted that along the main branch of the linearly polarized solutions, both of these conditions are satisfied simultaneously, which allows for the existence of two bistable side branches that leave and rejoin the main branch at the turning points where $t_\pm = 0$. This can be observed within figure 5-2, where it is unsurprising to note that the system is symmetric about the linearly polarized branch. Additionally, this demonstrates that the side branches can exist only when the system in pumped above the inflection point of the dispersion relation, and the system is bistable. Otherwise, the homogeneous solutions will retain the polarization of the pump for all pump intensities. It is noted that the two elliptically polarized branches (that are degenerate under the interchange of left and right handed polarization components) emerge from the turning points of the bistable linearly polarized branch. This degeneracy is broken once $a \neq b$.

When the system is bistable and pumped with an elliptically polarized beam, two bistable regimes are present, each one of these is associated with either t_l or t_r. These regimes occur at significantly different energies where the first has the polarization of the pump, whilst the second bistable region is orientated such that the polarization of the homogeneous solution tends towards a linear polarization at high energies. Whilst the pump intensity required to access the first bistable region is almost independent of polarization, the energy required to access the second of these regions is highly dependent upon it. When the polarization tends towards a circular polarization, the pump intensity required access the second of these regions tends to infinite as shown through figure 5-2.

The transition between the solution associated with linearly and elliptically polarized pumps occurs through the separation of one of the sideband from the main branch to form a closed loop, while there is an opening of the 'main linearly polarized branch' to leave a single curve. The closed region is found to shrink and once $a/b > 1.1$ or equivalently $b/a > 1.1$, the loop disappears entirely. While this closed region exists, it is noted that the two elliptically polarized components are no longer degenerate. In this transitional regime, there still exist three bistable regions yet one of these is located upon the closed loop.

By considering the variation of the system in the presence of an external magnetic field, χ as seen in figure 5-4, under a linearly polarized pump, the change associated with the variation of the magnetic field is superficially similar to that associated with changes in polarization. Through equation 5.17, it is apparent

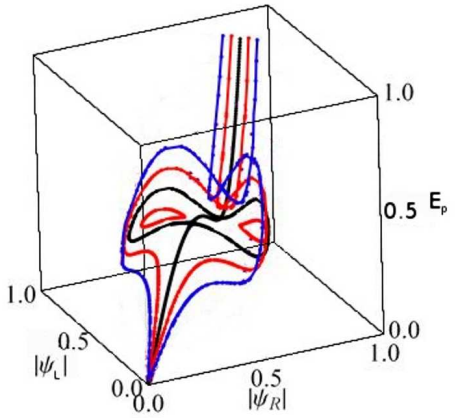

Figure 5-4: *Plot of E_p over the $|\psi_r|-|\psi_l|$ plane for $k_p = \pi/2$, $\delta_p = -0.05$, $\delta_e = -0.05$, $\gamma_{ph} = \gamma_e = 0.1$ and $\eta = 0$, under a linearly polarized pump. The black line corresponds to the solution in the absence of an external magnetic field, while the red (blue) lines correspond to the solution for $\chi = \pm 0.05$ ($\chi = \pm 0.10$).*

that the magnitudes of $|\psi_l|^2$ and $|\psi_r|^2$ no longer coincide at the turning points, and correspondingly neither do the associated pump intensities in contrast to the case of varying polarization in the absence of a magnetic field. Additionally, it is noted that at high energies, the final polarization of the system opposed the initial case, where at low energy, a solution with $\chi > 0$ will favor $|\psi_l|$, whilst at high energies, this solution will twist away from $|\psi_x|$ towards $|\psi_r|$.

5.4 Stability of the Polarized System

In the manner discussed for the strongly coupled homogeneous case, we now consider the stability of the system in the absence of magnetic fields, where as before, we proceed to expand the fields as

$$E_{r,l} \to A_{r,l} + \epsilon_{Er,l+} e^{i\vec{\kappa}\cdot\vec{x}+\lambda t} + \epsilon_{Er,l-} e^{-i\vec{\kappa}\cdot\vec{x}+\lambda^* t}$$
$$\psi_{r,l} \to B_{r,l} + \epsilon_{\psi r,l+} e^{i\vec{\kappa}\cdot\vec{x}+\lambda t} + \epsilon_{\psi r,l-} e^{-i\vec{\kappa}\cdot\vec{x}+\lambda^* t}$$

We substitute these back into the system of equations to obtain the eigenvalue equation

$$\begin{aligned} \lambda\epsilon &= M\epsilon \\ M &= \begin{pmatrix} M_E & M_\Omega \\ M_\Omega & M_\psi \end{pmatrix} \end{aligned} \tag{5.20}$$

where

$$\begin{aligned} \epsilon &= \begin{pmatrix} \epsilon_E & \epsilon_\psi \end{pmatrix}^T \\ \epsilon_E &= \begin{pmatrix} \epsilon_{ER+} & \epsilon_{ER-} & \epsilon_{EL+} & \epsilon_{EL-} \end{pmatrix} \\ \epsilon_\psi &= \begin{pmatrix} \epsilon_{\psi R+} & \epsilon_{\psi R-} & \epsilon_{\psi L+} & \epsilon_{\psi L-} \end{pmatrix} \end{aligned}$$

and

$$\begin{aligned} M_\Omega &= \begin{pmatrix} \Omega_R & 0 & 0 & 0 \\ 0 & -\Omega_R & 0 & 0 \\ 0 & 0 & \Omega_R & 0 \\ 0 & 0 & 0 & -\Omega_R \end{pmatrix} \\ M_E &= \begin{pmatrix} L_+ & 0 & -h_+ & 0 \\ 0 & -L_-^* & 0 & h_+^* \\ -h_- & 0 & L_+ & 0 \\ 0 & h_-^* & 0 & -L_-^* \end{pmatrix} \\ M_\psi &= \begin{pmatrix} Q_+ & \alpha_0 B_r B_r & \alpha_2 B_r B_l^* & \alpha_2 B_l B_l \\ -\alpha_0 B_l^* B_r^* & -Q_+^* & -\alpha_2 B_l^* B_r^* & -\alpha_2 B_l B_r^* \\ \alpha_2 B_l B_r^* & \alpha_2 B_l B_r & Q_- & \alpha_0 B_l B_l \\ -\alpha_2 B_l^* B_r^* & -\alpha_2 B_l^* B_r & -\alpha_0 B_l^* B_l^* & -Q_-^* \end{pmatrix} \end{aligned}$$

with

$$\begin{aligned} L_\pm &= -(k_p \pm k_x)^2 - k_y^2 + \delta_p + i\gamma_{ph} \\ Q_+ &= \delta_e + \chi - 2\alpha_0 |B_r|^2 - \alpha_2 |B_l|^2 + i\gamma_e \\ Q_- &= \delta_e - \chi - 2\alpha_1 |B_l|^2 - \alpha_2 |B_r|^2 + i\gamma_e \\ h_\pm &= \eta((k_p \pm k_x)^2 - k_y^2) \end{aligned}$$

which provides the means to determine the stability of the system. The Bogoliobov spectra illustrates that the parametric scattering regime is preserved for combinations of pump momentum and detuning that are located above the inflection point of the lower branch.

Now, we transform to the $TM-TE$ basis for the case of a linearly polarized pump and obtain a set of matrices associated with parallel and perpendicular perturbations in order to examine the difference in stability of these components. For parallel perturbations in the absence of a magnetic field, we obtain

$$\lambda \begin{pmatrix} \epsilon_{Ex} \\ \epsilon^*_{Ex} \\ \epsilon_{\psi x} \\ \epsilon^*_{\psi x} \end{pmatrix} = \begin{pmatrix} L_+ & 0 & -\Omega_R & 0 \\ 0 & -L^*_- & 0 & \Omega_R \\ -\Omega_R & 0 & Q_x & Q_1 \\ 0 & \Omega_R & -Q^*_1 & -Q^*_x \end{pmatrix} \cdot \begin{pmatrix} \epsilon_{Ex} \\ \epsilon^*_{Ex} \\ \epsilon_{\psi x} \\ \epsilon^*_{\psi x} \end{pmatrix} \tag{5.21}$$

while for perpendicular perturbations

$$\lambda \begin{pmatrix} \epsilon_{Ex} \\ \epsilon^*_{Ex} \\ \epsilon_{\psi x} \\ \epsilon^*_{\psi x} \end{pmatrix} = \begin{pmatrix} L_+ & 0 & -\Omega_R & 0 \\ 0 & -L^*_- & 0 & \Omega_R \\ -\Omega_R & 0 & Q_y & -\frac{|B_x|^2}{4} \\ 0 & \Omega_R & \frac{|B_x|^2}{4} & -Q^*_y \end{pmatrix} \cdot \begin{pmatrix} \epsilon_{Ex} \\ \epsilon^*_{Ex} \\ \epsilon_{\psi x} \\ \epsilon^*_{\psi x} \end{pmatrix} \tag{5.22}$$

where

$$\begin{aligned} Q_x &= -\frac{1}{2}\left(1+\frac{\alpha_2}{\alpha_1}\right)|B_x|^2 + i\gamma_e + \delta_e \\ Q_y &= -\frac{|B_x|^2}{2} + i\gamma_e + \delta_e \\ Q_1 &= -\frac{1}{4}\left(1+\frac{\alpha_2}{\alpha_0}\right)|B_x|^2 \end{aligned} \tag{5.23}$$

Along the linearly polarized branch of the system under a linearly polarized pump, the system is always stable with respect to these perpendicular perturbations. However, at the turning points of the bistable region, zero eigenvalues exist and the two degenerate elliptically polarized branches separate and reconnect to the main branch. In contrast to this, perturbations that are parallel to the pump can lead to instabilities within such a system. These instabilities are only present when the system is bistable, wherein it takes the form of parametric instabilities,

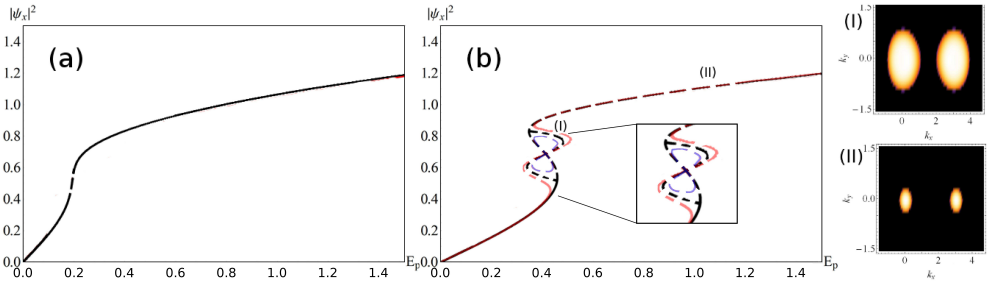

Figure 5-5: *Plot of* $|\psi_x|^2$ *against* E_p *for* $\gamma_{ph} = \gamma_e = 0.05$ *and (a)* $k_p = 1.2$, $\delta_p = \delta_e = -0.36$, *(b)* $k_p = \pi/2$, $\delta_p = \delta_e = -0.05$ *and* $a = b = 0.5$. *The dashed lines indicate where the respective solutions are unstable. The red and blue lines in (b) are for* $a = 0.525$ *and* $b = 0.475$. *The insets (I) and (II) display the associated instability domain for mixed perturbations at the associated points.*

as it does for the scalar system. This form of instability is exhibited within the insets of figure 5-5, when the main panel serves to illustrate the extent of the instability regions. A solution under elliptically polarized pumping is shown in figure 5-6. These elliptically polarized solutions are also seen to be unstable and take the form of parametric instabilities in the same manner as those exhibited along the linearly polarized branch when the system in pumped by a beam with either a linear or elliptical polarization. Additionally, the blue curve in this figure illustrates the stabilization of the first bistable region in the presence of an external magnetic field of the appropriate sign, in constant to the two distinct unstable regions attached to changes in polarization.

When a system under elliptical pumping is exposed to an external field of sufficient strength, the first bistable region can be stabilized by an appropriate signed field. However, if the solution is exposed to a field of the opposite sign, then the instability domain will extend between both bistable regions.

The existence of a nonzero η results in the splitting of the dispersion curves with respect to the left and right-handed circularly polarized components, wherein the left-handed component is associated with the lower curve associated with each branch, as marked at $k_x = 0$ which is illustrated in figure 5-7. This results in different stability properties for each polarization component. In this figure, η is an order of magnitude less than that shown in figure 5-1 and it can be seen that even whilst the splitting as a relatively minor effect on the dispersion relation, it has a significant effect on the stability of the homogeneous solution. Interestingly, these differences result in the instability of the linearly polarized

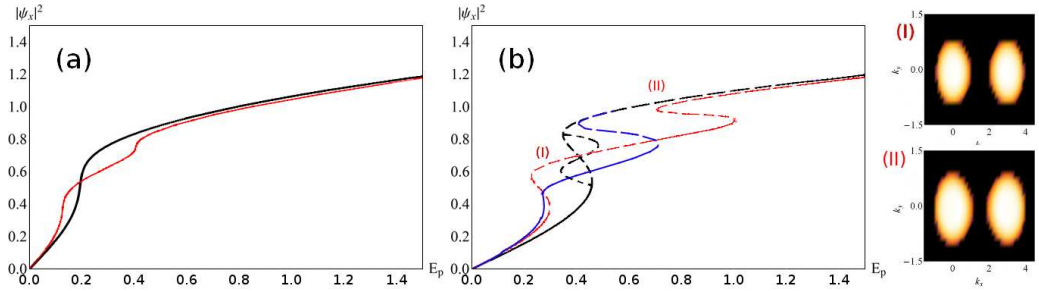

Figure 5-6: *Plot of* $|\psi_x|^2$ *against* E_p *for* $\gamma_{ph} = \gamma_e = 0.05$ *and (a)* $k_p = 1.2$, $\delta_p = \delta_e = -0.36$ *and (b)* $k_p = \pi/2$, $\delta_p = \delta_e = -0.05$. *The black line corresponds to the solution under linearly polarized pumping, while the red lines correspond to the system under an elliptically polarized pump with of the form* $a = 0.75$, $b = 0.25$. *Finally, the blue line in (b) corresponds to the solution under linearly polarized pumping in the presence of a magnetic field,* $\chi = 0.1$. *The dashed lines indicate where the respective solutions are unstable. The insets (I) and (II) display the associated instability domain for mixed perturbations at the associated points.*

modes with respect to perturbations possessing an orthogonal polarization. The evolution of this regime with increasing pump intensity can be observed in figures 5-10 and 5-11 in the absence and presence of the splitting term, through the changing boundary of the colored region, starting from just above the bistable region, wherein it is seen that the spot size decreases with increasing intensity as for the scalar case.

5.5 Spin Vortices

The system is seeded in the same manner as discussed in previous section, with the same polarization as that of the pump. When $\eta = 0$, it is observed that vortices develop exactly as discussed previously, where $m = 1$ vortices are stable, whilst higher order ($m = n$) vortices split into n $m = 1$ vortices, that retain their polarization. When $\eta \neq 0$, a linearly polarized $m = 1$ vortex will develop into left and right-handed circularly polarized $m = 1$ vortices, which does not occur for $\eta = 0$, as illustrated in figure 5-8. Correspondingly, it is feasible for independent vortices to exist in each polarization component, in the absence of TE-TM splitting.

Higher order vortices are still unstable and split into n $m = 1$ vortices, however they also experience this splitting into left and right components. This is illustrated within figure 5-9 where the splitting of a higher order vortex serves

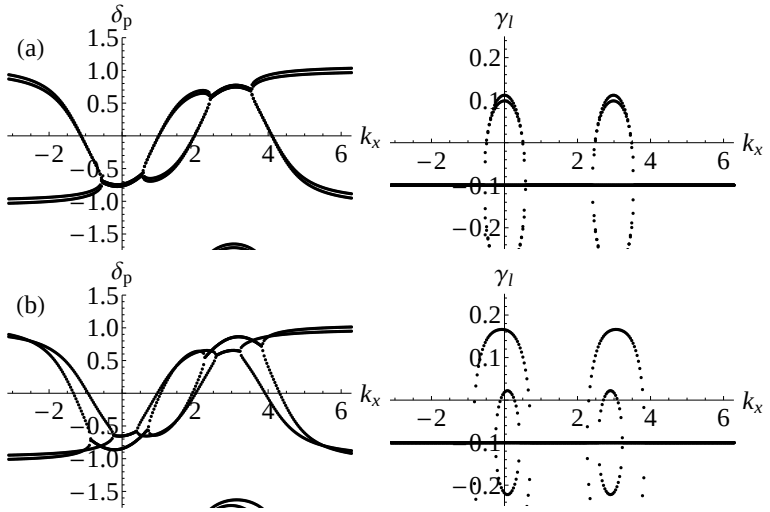

Figure 5-7: *Bogoliobov spectra (left) and instability domains expressed in the circular basis (right) along the k_x axis, for a linear polarization parallel to the pump for $k_p = \pi/2$, $\delta_p = \delta_e = -0.05$, $\gamma_{ph} = \gamma_e = 0.1$ and $E_p = 0.56$, for (a) $\eta = 0$ and (b) $\eta = 0.025$.*

to better illustrate this separation of the left and right components through the panels displaying the $|\psi_x|$ and $|\psi_y|$ polarizations.

When the splitting is large, the splitting couples the two component such that a vortex seeded exclusively in one polarization will stimulate a corresponding vortex in the other at the same location. Whilst the position of the phase singularities will coincide, the distribution of polariton density about the vortex core will be different between the left and right-handed polarization components due to the differences between the velocity of the components, where one recalls that the velocity of the signal is dependent on the gradient of the dispersion relation about the signal and idler, as discussed in section 4.4.6.

5.6 Polarized Vortex Lattices

In section 4.4.5, we noted that a line of existence exists for an arbitrary vortex lattice and now we consider how this line is modified as one varies the polarization of the system.

First, we consider the case where $\eta = 0$, where no momentum dependent splitting of the photonic component occurs. Through which, it is found that the location of the stable points for both polarizations coincide, thus it is possible to retrieve stability curves for vortices in the (E_p, k_x) plane that resemble those

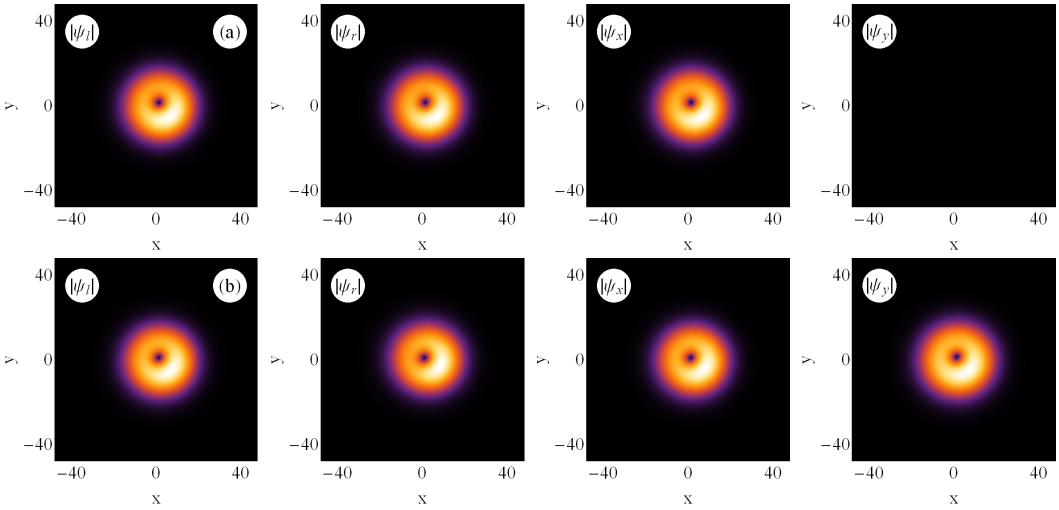

Figure 5-8: *Plot of an $m = 1$ vortex evaluated at $k_p = \pi/2$, $\delta_p = \delta_e = -0.05$, $\gamma_{ph} = \gamma_e = 0.1$, $E_p = 0.45$ at $t = 50$, pumped along E_x. In (a) we have $\eta = 0$ while (b) has $\eta = 0.0093$. Each panel displays the filtered signal about $k_x = 0$ of the exciton field for the circular and linear polarizations respectively. We note that in each case, there is no photon or exciton density with a polarization $|\psi_y|$ at $t = 0$.*

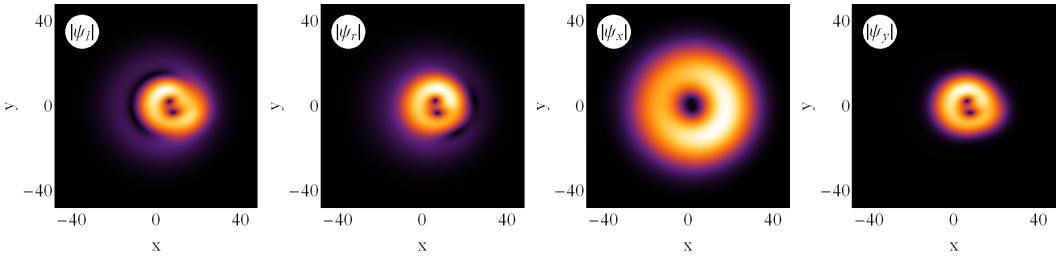

Figure 5-9: *Plot of an $m = 2$ vortex evaluated at $k_p = \pi/2$, $\delta_p = \delta_e = -0.05$, $\gamma_{ph} = \gamma_e = 0.1$, $E_p = 0.45$ and $\eta = 0.0093$ at $t = 50$, pumped along E_x. Each panel displays the filtered signal about $k_x = 0$ of the exciton field for the circular and linear polarizations respectively. We note that at $t = 0$, there is no photon or exciton density with a polarization $|\psi_y|$.*

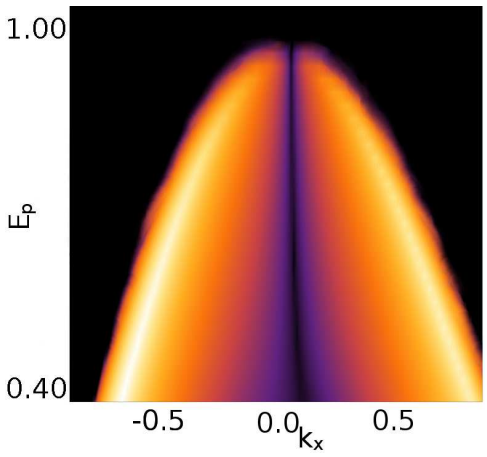

Figure 5-10: *Existence domain of stable solutions on the (k_x−E_p) plane, for $k_p = \pi/2$, $\delta_p = \delta_e = -0.05$, $p = \pi/80$, $\eta = 0$ with a linear polarized pump that is parallel to cavity plane, along the main upper branch, beginning just over the bistable region. The purple regions indicate locations of stable honeycomb vortex lattices in the plane, while the lighter regions indicate areas of increasing instability.*

observed in the scalar system. These lattices are found to possess the same dynamics as observed for scalar lattices, however it is found that modification of the instability domain results in the existence of stable lattices at different seed momentum for a given pump, as illustrated within figure 5-10. As earlier, polarized systems can possess points where the stable points coincide and thus there are stable lattices. As one moves away from these points of stability, the dynamics of these vortex lattices are seen to be resemble to those discussed previously in chapter 4.

As in the scalar case, we seed a honeycomb vortex lattice through the signal, with the same polarization as that of the pump. Although this choice of signal polarization is arbitrary, since the interaction between the polarizations will lead to the generation of the lattice associated with the pump polarization, regardless of that for the initial seed. When the two Fourier components that are off-axis are greater than the on-axis component, one observes that vortices develop as in the spin-less case, rather the pairs do not merge along the perpendicular axis, rather the $|\phi_l\rangle$ and $|\phi_r\rangle$ merge along the opposing axes, while when the on-axes component dominates, the vortex-antivortex pairs are seen to annihilate is exactly the same manner as for the spin-less case. However, when the instability domains associated with each circularly polarized component differ.

When one allows $\eta \neq 0$, the splitting results a separation of the instability

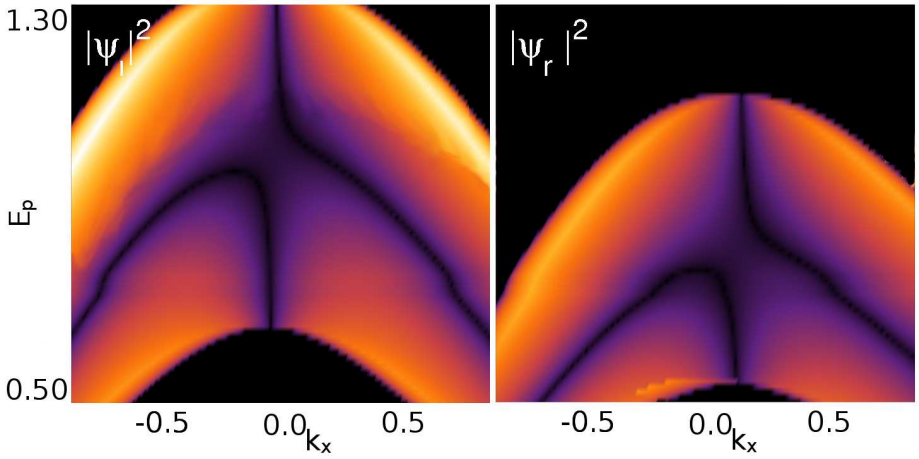

Figure 5-11: *Existence domain of stable solutions on the ($k_x - E_p$) plane, for $k_p = \pi/2$, $\delta_p = \delta_e = -0.05$, $p = \pi/80$ and $\eta = 0.025$. The system is pumped with a beam that has a linear polarization that is parallel to cavity plane, along the main upper branch, beginning just over the bistable region. The purple regions indicate locations of stable honeycomb vortex lattices in the plane, while the lighter regions indicate areas of increasing instability, for left and right-handed circular polarizations respectively.*

domains for the $|x\rangle$ and $|y\rangle$ polarization states. This separation allows for the patterns that form in each component to possess different velocities and thus separate into half-vortex lattices [83]. Each of these lattices will evolve independently in the manner previously discussed and it is possible to determine that the lattice in each polarization component will be stable for certain seed momentum and pump intensities. While stable points exist within each polarized component, they do not occur at the same value of k_s, as evident in figure 5-7. Thus, one cannot obtain a stable lattice when η is large when the system possesses a polarization other than either of the circularly polarized states, as observed in figure 5-11, or equivalently when the pump possesses an elliptical polarization. In each case, the left and right handed components of the lattice evolving differently, as is illustrated in figure 5-12. Additionally the presence of η leads to differing dispersion relations for $|\psi_r\rangle$ and $|\psi_l\rangle$, from which it is seen that the velocities associated with each polarization component of the lattice do not coincide. These differences in velocity and within the instability domains are also present in elliptically polarized systems regardless of the absence or presence of the splitting terms.

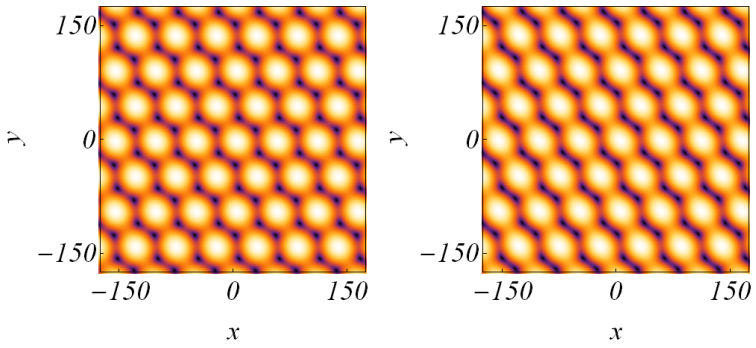

Figure 5-12: *Plot of the signal $|\psi_l|$ and $|\psi_r|$ fields respectively, as evaluated for $\delta_p = \delta_e = -0.05$, $k_p = \pi/2$, $E_p = 0.56$, $\eta = 0.025$ and $\gamma_{ph} = \gamma_e = 0.1$, at $k_s = 0.08$, $t = 90$.*

5.7 Soliton Polarization Effects

Now, we examine the behavior of solitons under pumps of different polarizations. The parameters featured in the sections on linear and elliptically polarized solitons correspond to $\hbar\Omega_R = 4.99meV$, $\hbar\delta_p = -2.34meV$, $\hbar\delta_e = -1.84meV$, $k_p = 2.37\mu m^{-1}$ and $\hbar\gamma_e = \hbar\gamma_{ph} = 0.2meV$ for a $GaAs$ microcavity at a temperature of $5K$. One time unit corresponds to $0.188ps$, and one unit of distance corresponds to $0.54\mu m$. These parameters correspond to the experimental values used in the paper by Sich *et al.* [161], for studying their dynamics at low temperatures.

In this work, we only consider bright solitons and thus the term linearly polarized soliton is often used in the place of the term vector bright soliton, as there is no risk of confusion between soliton being discussed which feature localized intensity peaks in both components and the vector dark solitons. When there is no risk of confusion the scalar circularly polarized solitons will be referred to as solitons, otherwise they will be referred to as scalar solitons or circularly polarized solitons.

For conciseness, when we refer to left-handed elliptically polarized solitons, we are referring to a vector dark bright soliton as in the work by Kivshar *et al.* [87] with the localized intensity peak located in the left-handed circular polarization, whilst the dark soliton profile is expressed in the right-handed polarization.

5.7.1 Solitons under Circularly Polarized Pumping

As we have reviewed, scalar bright solitons have been shown to be long lived in the presence of a flat pump, and exist when the system is bistable. In the limit of weak

interactions between opposing polarizations ($\alpha_2 \to 0$), these circularly polarized solitons coincide with the scalar cavity solitons reviewed in the introduction, since at low energies, a non-zero polariton density is present only in a single polarization component.

In the presence of a Gaussian pump, the maximum of the solitons that form in this case corresponds with the maximum of a soliton under a flat pump. Here, solitons are seen to exist within exactly the same bistable region, as shown in figure 1-4(a), where one can see that for a fixed probe intensity, the exciton density decreases with increasing pump momentum above the bistable region. In the same region, the photon density is seen to decrease at a substantially faster rate. The solitons that exist at this energy are seen to move significantly faster than the group velocity of the background, as is demonstrated within figure 1-4(b). In which, we have calculated the group velocity of the background is calculated through $d\omega/dk|_k = k_p$ where the frequency ω found through the real part of the appropriate lower branch eigenvalue of equation 3.22. Additionally, it is noted that just as the soliton maximum coincided with that of the homogeneously pumped case, the velocities also coincide.

We seed the system with the solitons associated with the homogeneously pumped system into the Gaussian regime at a point where the pump intensity is sufficient for the system to be bistable, whilst remaining along the lower branch. As before, a split step method is used to enable the study of their temporal evolution. Through which, one can observe that the solitons can be seen to persist in a region that is approximately one standard deviation away from the pump maximum, as shown in figure 5-13. Within this region, there behavior is identical to that associated with the flat pump system. If one uses a narrow writing beam positioned within this window, these solitons have been found to develop naturally. Beyond this region, solitons rapidly decay.

Similarly, these effects are visible under super-Gaussian pumps, as illustrated within figure 5-14, through which it can be observed that the solitons will decay when the pump intensity has decreased by approximately 15% from the maximum. In both cases, the solitons are observed to travel with a velocity that is exactly equal to that associated with the homogeneously pump system, up until the moment of the dissipation.

Having seen that solitons are supported within the one dimensional system, we proceed to examine the two-dimensional system, following the same approach as previously, where the pump is orientated along the x-axis, and the seed is

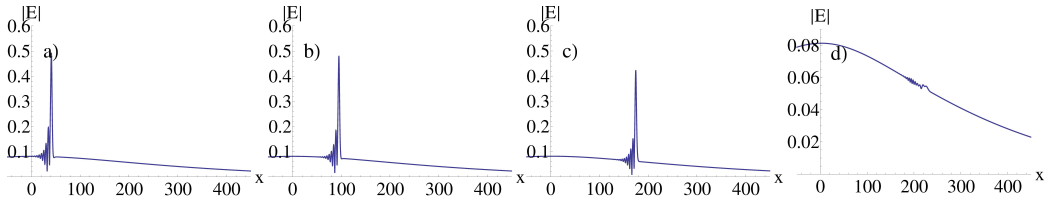

Figure 5-13: *Plot of a one dimensional soliton in a circularly polarized Gaussian pumping regime, for* $\delta_p = -0.184$, $k_p = 1.25$, $E_p = 0.160$ *and* $\eta = 0$ *at times of (a)*$t = 300$, *(b)*400, *(c)*500 *and (d)*600 *respectively. Only the right-handed component is shown as* $|\psi_l| = 0$.

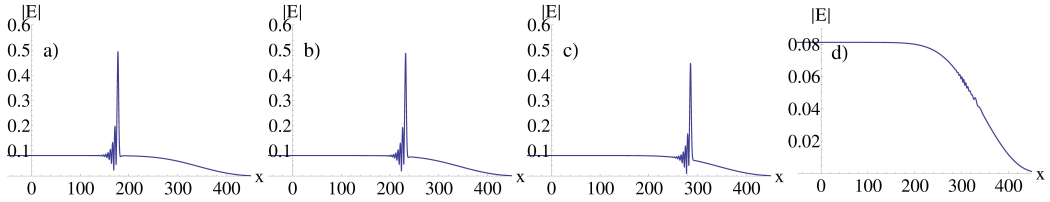

Figure 5-14: *Plot of a one dimensional soliton in a circularly polarized super-Gaussian pumping regime, for* $\delta_p = -0.184$, $k_p = 1.25$, $E_p = 0.160$ *and* $\eta = 0$ *at times of (a)*$t = 300$, *(b)*400, *(c)*500 *and (d)*600 *respectively. Only the right-handed component is shown as* $|\psi_l| = 0$.

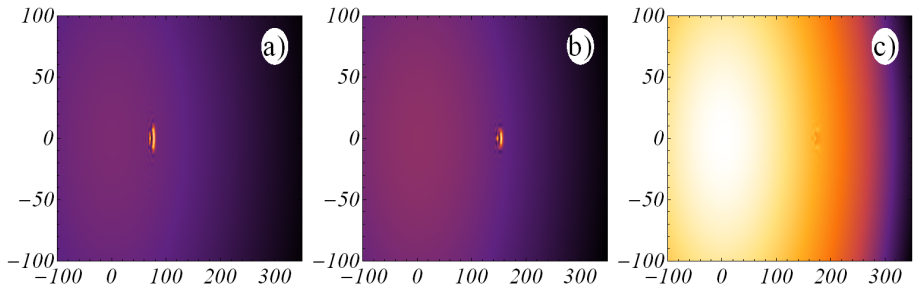

Figure 5-15: *Plot of a two dimensional soliton in a circularly polarized Gaussian pumping regime, for* $\delta_p = -0.184$, $k_p = 1.25$, $E_p = 0.160$ *and* $\eta = 0$ *at times: (a)* $t = 250$, *(b)* 400 *and (c)* 450. *The pump has a width* $W = 350$, *whilst the seed has a width* $W_s = 10$ *and an intensity of* $0.25E_p$, *for the total* ψ*-field. Only the right-handed component is shown as* $|\psi_l| = 0$.

initially aligned with the pump. At different energies within the bistable regime, the soliton-like solutions experience either a focusing or defocusing effect along the y-axis while the pump is flat.

For a narrow seed, the evolution is initially analogous to a soliton on the flat background. As it moves towards the position of maximum pump intensity, the soliton is observed to grow along the direction that is perpendicular to that of the pump. Once it has passed this position, it is observed that the soliton begins to shrink along the y-axis. This remains until it approaches the edge of the bistable region which is typically located at approximately one standard deviation away from the pump maximum, wherein it rapidly decays as can be seen in figure 5-15. This behavior is due the variation in the gradient of the pumping spot along the y-axis, where the more pronounced the gradient; the faster the soliton grows and shrinks. This behavior is produces rates of expansion or contraction that are significantly stronger than that associated with the magnitude of the soliton energy with respect to the Maxwell point.

The use of a super-Gaussian beam that is very much wider than the soliton serves to mitigate this effect, due to the slower variation along the y-axis, however it is noted that once the soliton reaches the edge of the pump region, then the embedded soliton will also decay in the same manner, as is shown in figure 5-16. Solitons are found to evolve from a writing beam, provided that it is situated in a region where the pump intensity is located in the bistable regime, which typically exists as a region that extends for one standard deviation to either side of the pump maximum. The soliton group velocity is found to match that for the flat pump, as for the one-dimensional case.

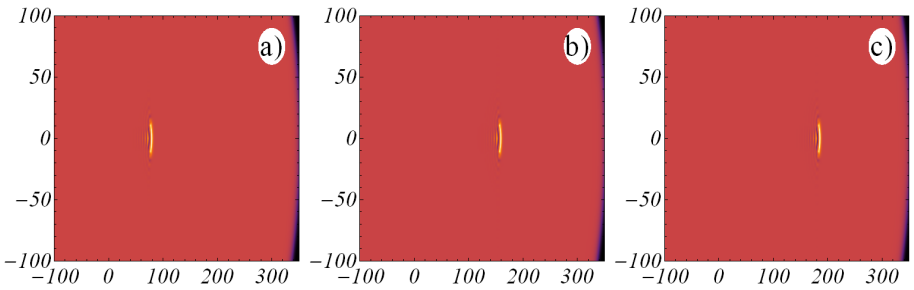

Figure 5-16: *Plot of a two dimensional soliton in a circularly polarized super-Gaussian pumping regime, for* $\delta_p = -0.184$, $k_p = 1.25$, $E_p = 0.160$ *and* $\eta = 0$ *at times: (a)* $t = 250$, *(b)* 400 *and (c)* 450. *The pump has a width* $W = 350$, *whilst the seed has a width* $W_s = 10$ *and an intensity of* $0.25E_p$ *for the total* ψ*-field. Only the right-handed component is shown as* $|\psi_l| = 0$.

As one increases the width of the seed, the formation of a soliton no longer occurs. Instead, the seed becomes modulated by a roll pattern that grows from the leading edge, along which the creation of vortex-antivortex pairs is noted. In general, these are $m = 1$ vortices located within the signal and idler bands, however for seeds that possess a similar width to that of the pump, one can observe the creation and annihilation of $m = 2$ vortex-antivortex pairs. These pairs are generated by the phase difference between the pump and probe [188, 148], or equivalently the presence of a phase difference across the pump spot due to noise or variations in the profile of the pump beam. These are illustrated through the presence of forked dislocations within the roll, where a single branch splits to $n+1$ branches at a vortex of winding number $m = n$. All of these vortex pair are observed to annihilate at a later time, such that vortex pairs along the pump axis survive for longer before annihilating.

In both the one and two-dimensional cases as shown in figures 5-13 through 5-16, we have seen that solitons exist until they reach the edge of the bistable region. In these simulations, we have also monitored the group velocity by tracking the position of the soliton maximum, and through which it is seen that it remains constant up until it reaches the position where the pump energy has decreased to the edge of the bistability region. After which, the soliton velocity is observed to rapidly decrease as can be seen in figure 5-17, where the comparison between the Gaussian and super-Gaussian pumping regimes demonstrates that this decreasing group velocity is a direct consequence of the pump beam profile.

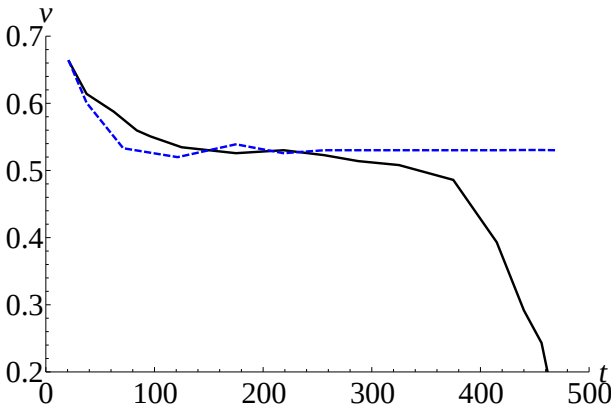

Figure 5-17: *Plot of soliton group velocity against time, as evaluated for* $k_p = 1.02$, $\delta_p = -0.45$, $\delta_e = -0.36$, $\gamma_{ph} = \gamma_e = 0.05$, $E_p = 0.05$ *and* $\eta = 0$ *for a circularly polarized Gaussian (black) and super-Gaussian (blue, dashed) pump with a width* $W_{pump} = 350$ *and Gaussian seed of width,* $W_{seed} = 10$ *as calculated for the two-dimensional system.*

5.7.2 Solitons under Linearly Polarized Pumping

Solitons are found to exist within each bistable regime, which can be observed in figure 5-18 for a system excited with a linearly polarized pump, and we note that these solitons do not coincide with the scalar solutions as the nonlinear interactions are weaker by a factor of four, as shown through equations 5.10. Instead, solitons in a linearly polarized pump regime are vector solitons, although it is noted that the $|E_x|$ and $|\psi_x|$ components of these soliton resemble the profile of the scalar solitons shown previously.

Through the use of the eigenvalue equation 5.20 that we derived for the analysis of the stability of the homogeneous system, it is also possible to evaluate the stability of the one-dimensional solitons by making the substitutions

$$\begin{aligned}
L_{\pm} &= -k_p^2 - \frac{d^2}{dx^2} + i(2k_p - v)\frac{d}{dx} + \delta_p + i\gamma_{ph} \\
Q_{+} &= i(2k_p - v)\frac{d}{dx} + \delta_e + \chi - 2\alpha_0|B_r|^2 - \alpha_2|B_l|^2 + i\gamma_e \\
Q_{-} &= i(2k_p - v)\frac{d}{dx} + \delta_e - \chi - 2\alpha_0|B_l|^2 - \alpha_2|B_r|^2 + i\gamma_e \\
h_{\pm} &= \eta(\pm k_p + \frac{d}{dx})^2
\end{aligned}$$

where v is the soliton velocity. It is seen that all three soliton branches are stable in the case of linearly polarized pumping in the absence of $TE - TM$ splitting

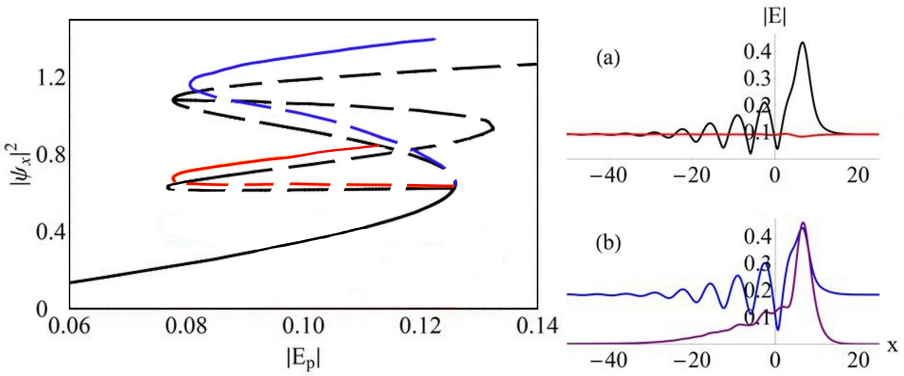

Figure 5-18: *Plot of the $|E_x|^2$ against pump intensity, displaying the position of the linear (red) and elliptically (blue) polarized single hump solitons under linearly polarized pumping along E_x. The system is operated at $k_p = 1.02$, $\delta_p = -0.45$, $\delta_e = -0.36$, $\gamma_{ph} = \gamma_e = 0.05$, $\eta = 0$ and $E_p = 0.095$. The dashed lines indicate the corresponding solution is unstable at those points. Panel (a) displays the (black) right and (red) left-handed elliptically polarized components of the 1d $|E|$ soliton profiles, while panel (b) displays (blue) $|E_x|$ and (purple) $|E_y|$.*

and external magnetic fields.

As before, we seed the system through a Gaussian pulse, which develops into a soliton. These solitons are strongly localized in real space, whilst possessing a broad energy-momentum spread, as observed experimentally in references [2] and [161]. This localization is in contrast to the well-studied polariton condensates, which correspond to a macroscopic occupation of a single momentum state.

For linear polarizations, the existence of a multiply stable region allows for the existence of multiple soliton branches. For all parameter sets, these soliton branches always emerge from the point where the homogeneous solution splits and in all cases, these solitons sit upon the linearly polarized lower branch. The resulting pitchfork bifurcation is most evident through consideration of the z-component of the pseudospin vector, $S_z = (|E_r|^2 - |E_l|^2)(|E_r|^2 + |E_l|^2)$ as witnessed in figure 5-19(a). Panel (b) illustrates the velocity curves associated with the linear and elliptically polarized solitons, wherein it is seen that the velocities of the excited solitons are identical for a given pump intensity, as determined through Newton's method.

Under Gaussian pumping, these polarized solitons travel in exactly the same manner as those undergoing homogeneous pumping, up until they are approach the boundary of the bistable region where they are found to rapidly decay as in the circularly polarized case. This is illustrated within figure 5-20 where it

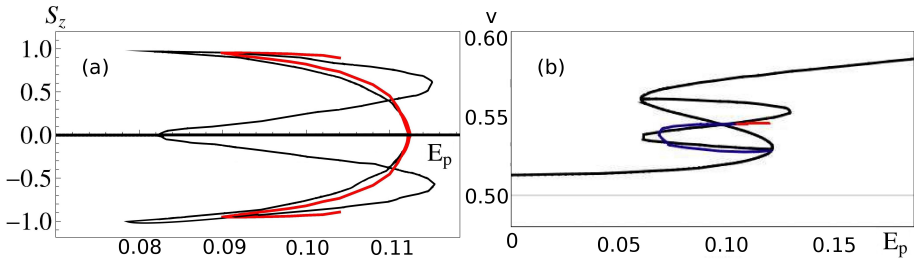

Figure 5-19: *(a) Plot of pseudospin component, S_z against pump intensity, E_p where the black curve indicates the homogeneous solution while the red curve illustrate the elliptical soliton branches to illustrate the pitchfork bifurcation.*
(b) Plot of the soliton velocity against pump intensity for linear (red) and elliptically (blue) polarized solitons, under linearly polarized pumping. The black curve displays the velocity as determined through stability analysis of the system as evaluated at $k = k_p$, as determined previously. In each case, the system is operated at $k_p = 1.02$, $\delta_p = -0.45$, $\delta_e = -0.36$, $\gamma_{ph} = \gamma_e = 0.05$ and $\eta = 0$.

is seen that once the soliton has developed from the initial Gaussian pulse, it initially expands and then begins to contract once it has passed the maximum of the Gaussian pump. The maximum of this soliton can be seen in figure 5-21(a), where it is observed that the soliton maximum rapidly decreases once it has passed the maximum of the pump profile. Panel (c) displays the variation of the width along the y-axis, where the rate of expansion or contraction is constant for as long as it persists. The polarization of the soliton is found to be preserved over its lifetime, where the polarization of the soliton maximum follows that of the homogeneous solution.

By following the evolution of these solitons in the frequency momentum domain, it can be seen within figure 5-22 that the seed pulse initially excites a polariton population about the seeding momentum on both upper and lower branches. The upper branch component is observed to swiftly decay to the lower branch (panels (b) and (g)). On the lower branch, a small fraction of the population decays to the minimum of the lower branch. Once the soliton has formed, a straight line is found to connect the minimum to the pump location that is almost tangential to the linear dispersion for that polarization component, at the pump momentum. This line is found to persist for as long as the soliton exists (panels (d) and (i)). Once the soliton reaches the boundary of the pump region, this line relaxes towards the linear dispersion, which is illustrated within figure 5-22(e) and (j).

In two-dimensional linearly polarized case, solitons evolve along the axis that

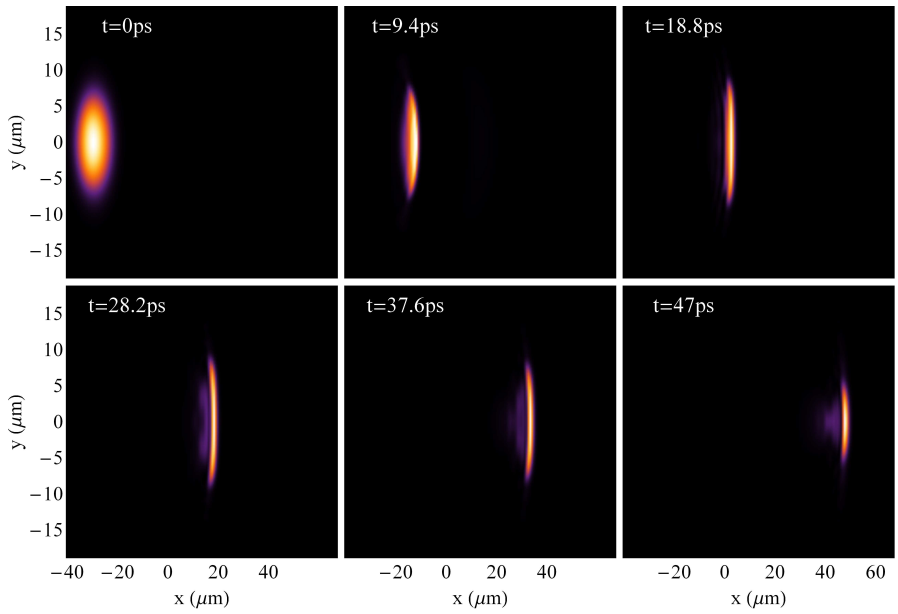

Figure 5-20: *Plot of the evolution of an elliptically polarized 2D soliton upon a Gaussian background. The system is operated at* $\hbar\Omega_R = 4.99meV$, $\hbar\delta_p = -2.34meV$, $\hbar\delta_e = -1.84meV$, $k_p = 2.37\mu m^{-1}$, $\hbar\gamma_e = \hbar\gamma_{ph} = 0.2meV$ *and* $\eta = 0$, *where it is pumped with a beam of TM polarization(a=b=0.5) whilst only the TE polarization is shown. In arbitrary units, these parameters correspond to those in figure 5-19. The system is seeded with a photonic Gaussian pulse at* $t = 0$.

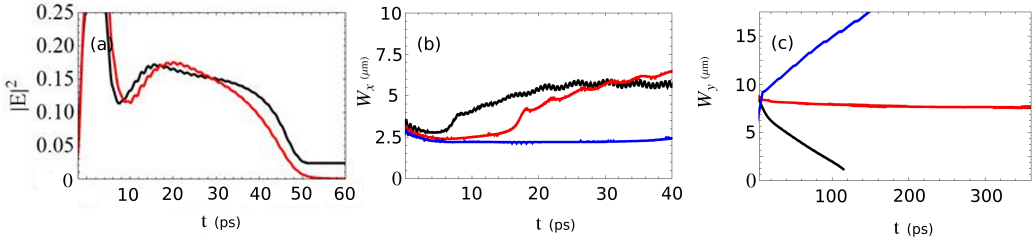

Figure 5-21: *(a) Plot of the variation in the soliton maximum for a seed of width* $W_s = 6$, *for (black)* $|E_x|^2$ *and (red)* $|E_y|^2$.
(b) Plot of the variation in the soliton width at half its peak value along the x axis over time, for (black) $E_s = 0.04$, *(red)* 0.05, *(blue)* 0.06.
(c) Plot of the variation in the soliton width at half its peak value along the y axis over time for (black) $E_p = 0.091$, *(red)* 0.095 *and (blue)* 0.105. *In each case, the remaining parameters are given in figure 5-20, which displays the corresponding two dimensional soliton profile for the curves shown in (a).*

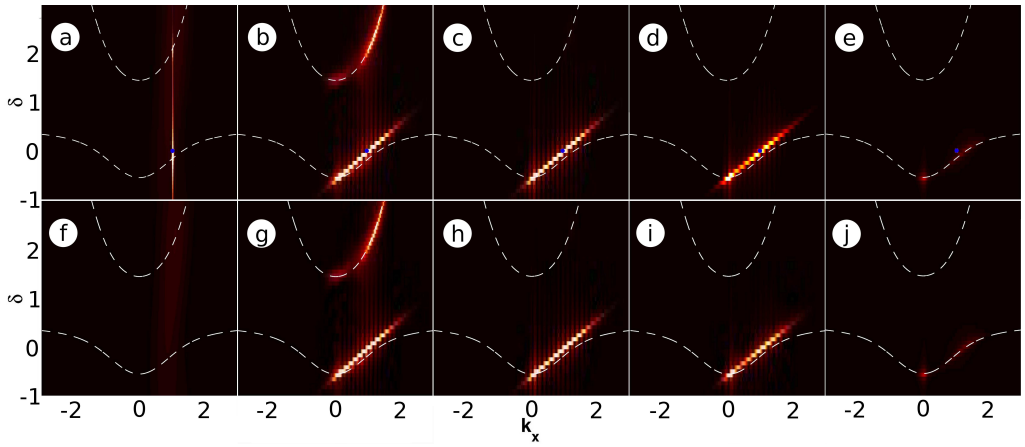

Figure 5-22: *Plot of the right-handed elliptically polarized soliton dispersion at* (a, f) $t = -37.5$, (b, g) $t = 37.5$, (c, h) $t = 112.5$, (d, i) $t = 187.5$ *and* (e, j) $t = 262.5$. *Panels* $(a - e)$ *correspond to a polarization of* ψ_x *while panels* $(f - j)$ *correspond to* ψ_y. *The dashed line illustrates the linearized polariton dispersion. The system is operated at* $k_p = 1.03$, $\delta_p = -0.45$, $\delta_e = -0.36$, $\gamma_{ph} = \gamma_e = 0.05$, $\eta = 0$ *and* $E_p = 0.078$ *when it is seeded with a right-handed circularly polarized pulse for a Gaussian pump of standard deviation* $W = 65$.

is perpendicular to the pump, in a manner that is qualitatively identical to the evolution of scalar solitons. The velocity of this expansion in the second dimension can be observed in figure 5-23 for both linearly and elliptically polarized solitons. Through which, it is observed that the velocity associated with elliptically polarized solitons is larger than for the linearly polarized case and the corresponding Maxwell point ($v_y = 0$) occurs for a lower pump intensity. When one is within a narrow range just below the Maxwell point, it is found that for a generic set of initial conditions, elliptically polarized solitons act as a set of stable attractors. The existence range of these attractors is illustrated through figure 5-24, where it is seen that stable elliptically polarized solitons achieve a greater maximum than the one-dimensional case, whilst the linearly polarized ones have a smaller magnitude.

The width of these solitons along the x-axis is shown in figure 5-21(b) for a range of seed intensities, wherein it is seen that there is a minimum energy required to excite the soliton. Once it has formed, the soliton maintains its width along this axis for its lifetime. When the initial pulse is not sufficient to excite a soliton, there is a rapid relaxation back to the background. While the seed strength is held constant, solitons excited by Gaussian pulses of different

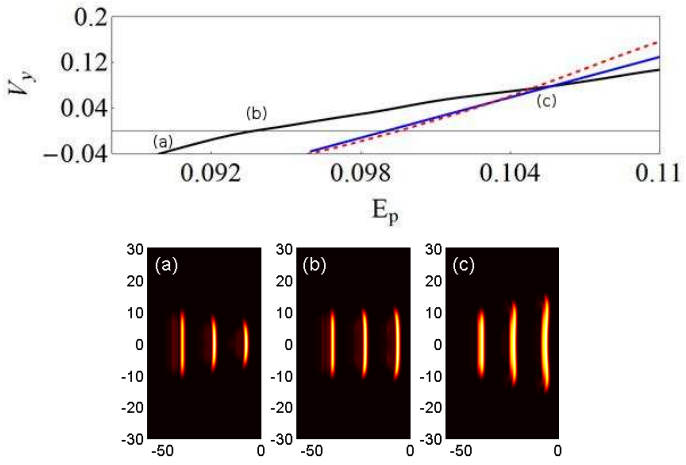

Figure 5-23: *Plot of the velocity, v_y perpendicular to the propagation direction as a function of pump intensity, E_p for (red) linear and (black) elliptically polarized solitons, for $\eta = 0$. The velocity of an elliptically polarized soliton with $\eta = 0.005$ is shown in blue. Panels (a-c) display the contraction and expansion of the elliptically polarized solitons as shown through the perpendicular polarization, E_y. The system is operated at $k_p = 1.03$, $\delta_p = -0.45$, $\delta_e = -0.36$, $\gamma_{ph} = \gamma_e = 0.05$, $\eta = 0$, starting from the linearly polarized homogeneous background, where the system is seeded with the extended 1d soliton profile.*

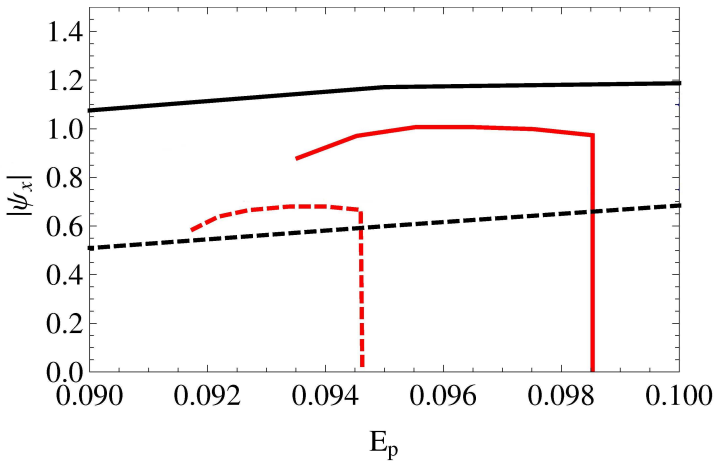

Figure 5-24: *Plot of the $|\psi_x|$ against E_p. The black lines show the branches of linear (solid) and elliptically (dashed) polarized 1d cavity polariton solitons. The red curves illustrate the existence range of stable 2d solitons.*

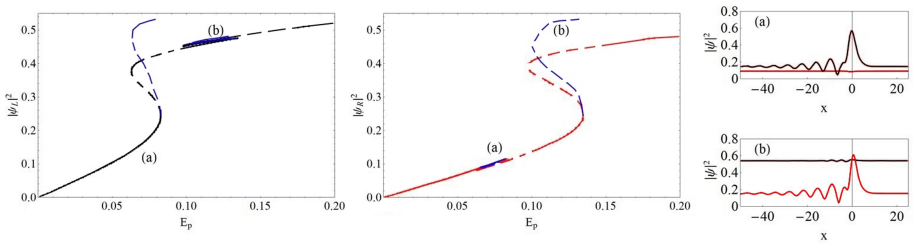

Figure 5-25: *Plot of the $|\psi_R|^2$ and $|\psi_L|^2$ against pump intensity, for an elliptically polarized pump with $a = 0.6$ and $b = 0.4$. The remaining parameters are identical to those given in figure 5-20. The blue curves indicate the soliton branches and the dashed line indicates the unstable region. Panel (a) displays the soliton profile at $E_p = 0.075$, while (b) corresponds to a pump intensity of $E_p = 0.125$. The red curves correspond to the right-handed polarization, whilst the black curves are associated to the left-handed polarization.*

widths will develop with the same width along the x-axis.

5.7.3 Solitons under Elliptically Polarized Pumping

Having discussed the special cases of circular and linearly polarized solitons, we discuss the dynamics under an elliptically polarized pump.

As we have discussed in the case of a purely circularly polarized pump ($a = 1$), it is readily apparent that the system corresponds exactly to the scalar solitons, in the limit of $\alpha_2 \to 0$. When this is not the case the circularly polarized solution still corresponds to scalar homogeneous solution at low energies, however there exists a second bistability regime at $E_p \to \infty$ as $a \to 1$, where in principle solitons could exist.

As one moves away from a circularly polarized pump, the energy required to access the second bistable region decreases rapidly. In this bistable region, a soliton branch exists that is well separated in energy from the other as shown in figure 5-25. Along these branches, the solitons resemble the elliptically polarized soliton observed when the system is pumped with a linearly polarized beam, as shown in panels (a) and (b) of figure 5-18, where the soliton peak is solely expressed in either the left or right handed circular polarization component, while along the second branch at a greater pump intensity, the soliton peak is seen to exist in the polarization that is not favorably aligned with the pump.

By evaluating the stability of theses solitons, it is seen that along the first soliton branch, the solutions are always completely stable whilst those along the second branch are generally unstable. This instability only arises when the cir-

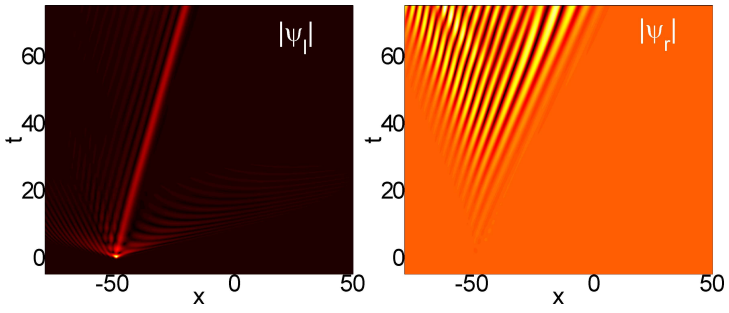

Figure 5-26: *Plot of $|\psi_r|$ and $|\psi_l|$ over time and distance, displaying the effects of instability on the soliton. The system is operated at $k_p = \pi/2$, $\delta_p = \delta_e = -0.05$ and $E_p = 0.6$ for an elliptically polarized pump with $a = 0.75$ and $b = 0.25$, in the absence of $TE - TM$ splitting or an external magnetic field.*

cularly polarized component that is favorably aligned with the pump exists upon a significantly stronger background than which can be associated with the peak of the soliton. When this is true, the interactions between the two modes result in an unstable soliton branch, wherein instabilities develop within the favorably aligned component, where a roll pattern is seen to develop behind the soliton as it propagates and eventually dissipates, as observable in figure 5-26.

As one approaches a linearly polarized pump, the emergence of the closed loop in the homogeneous system yields a third soliton branch in the emerging bistable region, which is illustrated previously through the red curves in figure 5-2, where along this branch, the solitons are increasingly linearly polarized, while the first of the elliptically polarized soliton branches develops to one of the elliptically polarized branches. The second of the soliton branches disconnects from the homogeneous solution whilst the background of the left and right components smoothly evolve to be equivalent, and thereby form the second of the degenerate elliptical branches. When the soliton peak is stronger than the background in the other component then up until the point when the second branch disconnects from the main branch, they are stable, however once it occurs it becomes strongly unstable. As the pump is further tuned towards a linear polarization, the two unstable branches become increasingly stable, such that all three branches are stable when the system is pumped with a linear polarization.

As discussed earlier, an external magnetic field produces a change in the polarization of the homogeneous solution, and it is unsurprising to note that when a soliton branch exists, the polarization of the solitons is similarly affected.

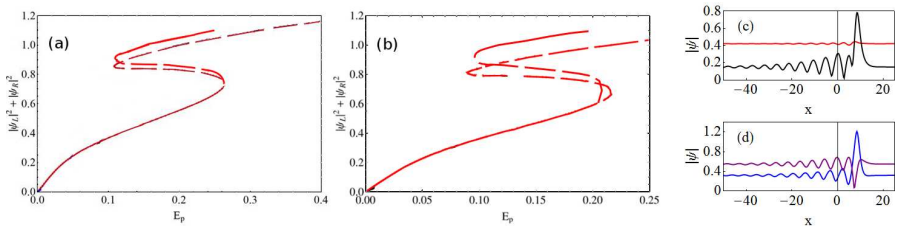

Figure 5-27: *Plot of the $|\psi_r|^2 + |\psi_l|^2$ against pump strength, displaying the position of single hump solitons for under linearly polarized pumping along E_x at a magnetic field,$\chi = +0.15$, where the dashed lines indicate the corresponding solution is unstable at those points. The system in operated at the parameters given in (a) figure 5-18, and (b) 5-25. Panels (c) and (d) illustrate the form of the solitons at $E_p = 0.15$ and $\chi = 0.15$ where the remaining parameters are associated with panel (a). Panel (c) displays the left (red) and right (black) components, while panel (d) illustrates the same soliton shown in the x-y basis through the blue and purple lines.*

Under a linearly polarized pump, it is seen in figure 5-27(c-d) that the solitons resemble those that exist under an elliptically polarized pump, but there is one significant difference in that these solitons as illustrated in panel (c) possess a notably longer tail.

In figure 5-27(a-b), it is seen that under a linearly polarized pump, the change associated with the variation of the magnetic field is superficially similar to that associated with changes in polarization. However, it is stressed that at high energies, the final polarization of the system opposes the initial polarization of the system. At low energy, for a solution with $\chi > 0$ that initially favors $|\psi_l|$ will at large energies, the solution will favor $|\psi_r|$, as opposed to $|\psi_x|$ when there is no field present. In figure 5-28, the variation in the width of the soliton branches is displayed, where it is clear that the magnetic field can be tuned to allow for the existence of a linearly polarized soliton branch when the system is pumped with an elliptically polarized beam.

Up to this point, we have focused on the situation where no momentum dependent splitting of TE and TM modes occurs. When $\eta \neq 0$, one can still observe the change from contracting to expanding two-dimensional solitons and the presence of a narrow region of stable solutions. The rate of change of velocity along the y-axis with pump intensity is found to increases, as illustrated in figure 5-23, and we note that the existence range of spin bullets is found to narrow as one increases the magnitude of the splitting.

As one increases either the absolute magnitude of the external field or in-

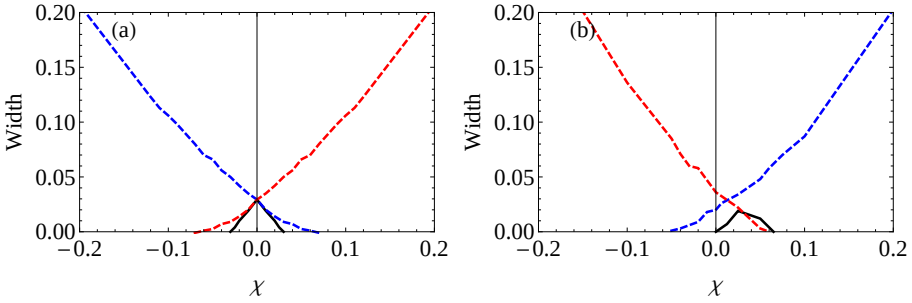

Figure 5-28: *Plot of the width of the soliton branch under a varying magnetic field, under (a) linearly and (b) elliptically polarized pumping (a=0.6, b=0.4). The remaining parameters are as given in figure 5-27. The dashed lines illustrate the first (red) and second (blue) elliptically polarized soliton branches, whilst the solid curve illustrates the linearly polarized branch.*

creases the size of the splitting, soliton which are unfavorably aligned with respect to an elliptically polarized pump, in the case of increased η, or aligned against the magnetic field will become unstable. In which case, both components will decay back to the homogeneous background.

5.7.4 Vector Parametric Cavity Solitons

Up to this point, we have focused on solitons that are strongly localized along the pump axis, however other families of soliton exist. For scalar solitons in micro-cavities, parametric cavity polariton solitons have been studied extensively[42], where it is suggested that parametric nonlinearity can support localization along the axis possessing a negative effective mass.

Parametric cavity polariton solitons have the form

$$\psi = \psi_s(y)e^{ik_s x} + \psi_p(y)e^{ik_p x} + \psi_i(y)e^{ik_i x} \tag{5.24}$$

where k_s is the momentum of the signal component located within an instability spot of the form witnessed within the insets of figure 5-5 about $k_x = 0$ while the idler momentum is given through $k_i = 2k_p - k_s$. Unlike vector solitons, these vector cavity parametric solitons are only localized along the direction that is perpendicular to the pump. A typical profile can be observed within figure 5-29, where the signal and idler components in both polarizations are seen to be particularly narrow and quasi-Gaussian in the same manner as the components orientated with $|E_y|$, while the central region of the $|E_x|$ polarization is broader

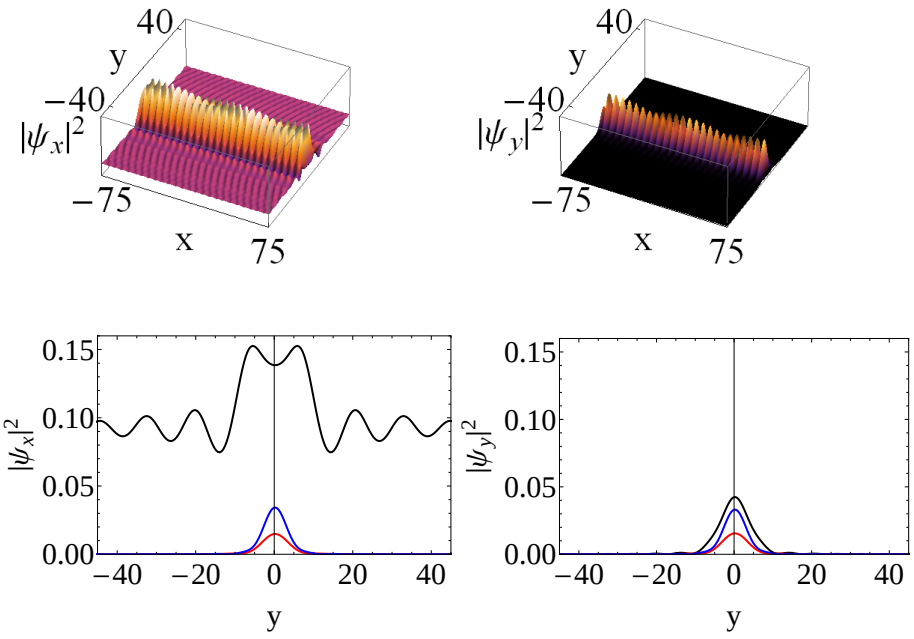

Figure 5-29: *Plot of a single humped elliptically polarized parametric cavity polariton soliton at* $E_p = 0.095$ *in the* $x - y$ *plane for* $|E_x|^2$ *and* $|E_y|^2$ *respectively. The profiles of the signal (red), pump (black) and idler (blue) components of the soliton along the y-axis are shown below. The parameters are the same as those given in figure 5-23.*

and possesses steep sides which develop into extended tails.

As one shifts the signal momentum along the pump axis whilst remaining within the instability spots, the amplitude of the soliton is observed to vary where the soliton's maximum amplitude can be associated with value of the signal momentum that is connected with the greatest instability, as is illustrated through figure 5-30. Furthermore as one moves away from the momentum with the maximum instability, the length of the soliton branch is seen to decrease. In a similar manner, multi-humped solitons can also be excited within the region, where a typical profile can be observed in figure 5-31. These multi-hump solitons are substantially broader than single-humped solitons whilst the idler component does not resemble the Gaussian signal component.

As for scalar parametric cavity polariton solitons discussed by Egorov *et al.* [42], the persistence of vector solitons serves to suggest that parametric processes work to promote the localization of solitons in a manner that is independent of the cross-interactions.

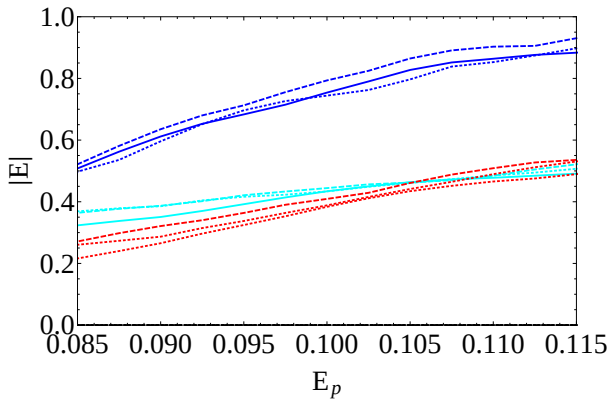

Figure 5-30: *Plot of $|\psi|$ against E_p for parametric cavity polariton solitons. The blue lines correspond to the linearly polarized $|E_x|$ solution while cyan (red) lines correspond to the $|\psi_x|$ ($|\psi_y|$) components for the elliptically polarized solution. The solid, dashed and dotted lines are evaluated at $k_s = 0$, $k_s = 0.1$ and $k_s = -0.1$. The parameters are the same as those given in figure 5-23.*

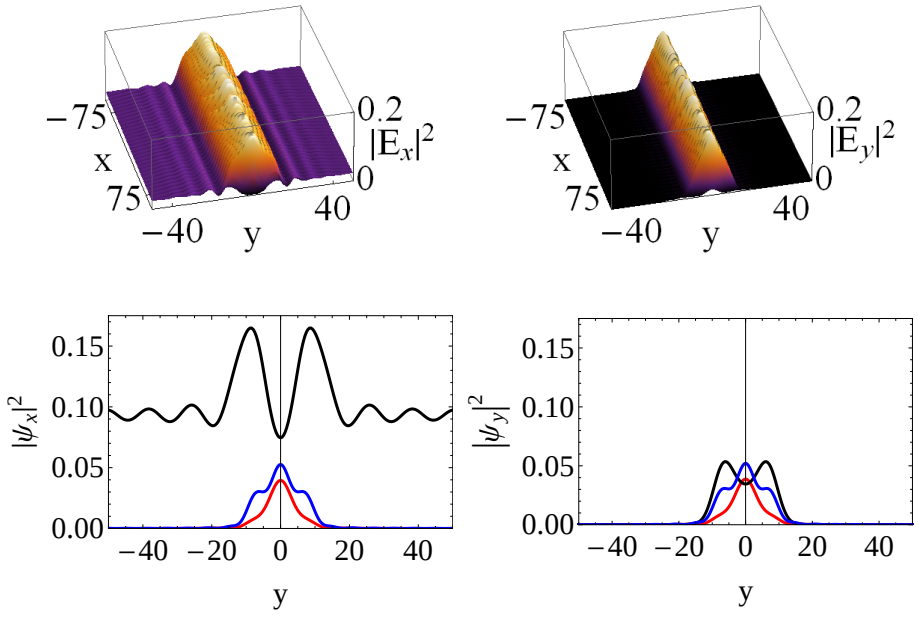

Figure 5-31: *Plot of a double humped elliptically polarized parametric cavity polariton soliton in the $x - y$ plane, for $|E_x|^2$ and $|E_y|^2$ respectively. The profiles of the signal (red), pump (black) and idler (blue) components of the soliton along the y-axis are shown below. The parameters are the same as in figure 5-29.*

5.7.5 Coherent Control of Polarized Solitons

Having examined the behavior of individual solitons in the system, we consider the possibility of controlling the behavior of solitons using a second pulse in phase or antiphase with the soliton. The soliton is initialized in the manner discussed earlier, and after it has survived until $t = 100$, we provide a second pulse of identical intensity and opposite phase of the initial pulse. When one works towards the lower edge of the soliton existence domain, this pulse is sufficient to disable the soliton, can be seen in figure 5-32. However as one moves along the soliton branch, the second pulse is no longer sufficient to completely remove the soliton, rather only one component of the elliptically polarized soliton can be efficiently eliminated. The remaining component is capable of rapidly restoring the soliton to the initial state.

Following this evolution in frequency-momentum space, it is seen that the addition of the second seed that is out of phase with the initial seeding pulse serves to excite additional population about the pump momentum. This population is excited primarily along the lower branch, and does not play any significant role in switching the soliton. These associated images are shown in figure 5-33, where panel (a) shows the initial excitation along both branches which rapidly develops to the linear soliton dispersion seen in panel (b). In panel (c), the second pulse is shown to excite polaritons along both branches; yet this excitation results in the rapid decay of polaritons to the linear dispersion of the lower branch, which is witnessed within panel (d). This decay follows the same evolution as that observed for a soliton that has reached the boundary of the bistable region under a Gaussian pumping regime, as the straight line connecting the signal region about $k_x = 0$ to the pump momentum descends back to the linear dispersion of the lower branch.

If the polarization of the second pulse is allowed to vary when one is working at a pump intensity where both elliptically and linearly polarized solitons exist, then one can transform the soliton between these states, provided that the polarization and strength of the seed are chosen to be just greater than the size of the gap between the respective soliton branches, as is illustrated within figure 5-34. When the intensity of this second pulse is significantly greater than the separation between the soliton and upper branch of the bistability region, the roll solution associated with the main branch will grow from the location of the pulse, regardless of the polarization of the soliton of the pulse. In both of these figures, the presence of a dispersive wave originating at the location of the seeds

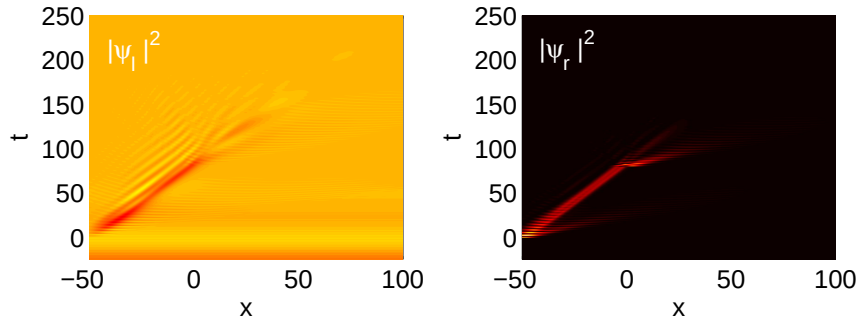

Figure 5-32: *Plot of the variation of* $|\psi_l|^2$ *and* $|\psi_r|^2$ *with time, illustrating the disabling of an elliptically polarized soliton at* $E_p = 0.095$*. The remaining parameters are the same as those in figure 5-23. The right-handed soliton is excited at* $t = 0$*, through the initially right-handed seed. The second pulse to disable the soliton occurs at* $t = 100$*.*

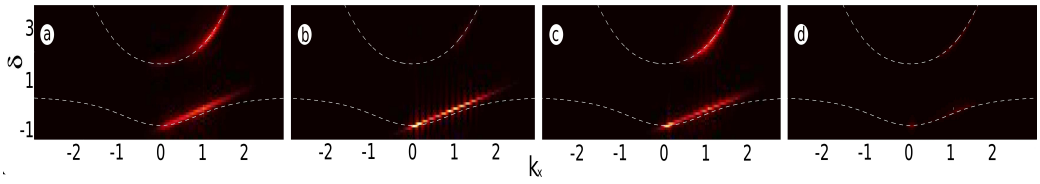

Figure 5-33: *Plot of the linearly polarized soliton dispersion at* (a) $t = 0$*,* (b) $t = 75$*,* (c) $t = 150$ *and* (d) $t = 225$*, when seed pulses of opposing phase enter the system at* $t = 0$ *and* $t = 150$*. The dashed line illustrates the linearized polariton dispersion. The system is operated at* $k_p = 1.03$*,* $\delta_p = -0.45$*,* $\delta_e = -0.36$*,* $\gamma_{ph} = \gamma_e = 0.05$*,* $\eta = 0$ *and* $E_p = 0.095$ *when it is seeded with a linearly polarized pulse under homogeneous pumping.*

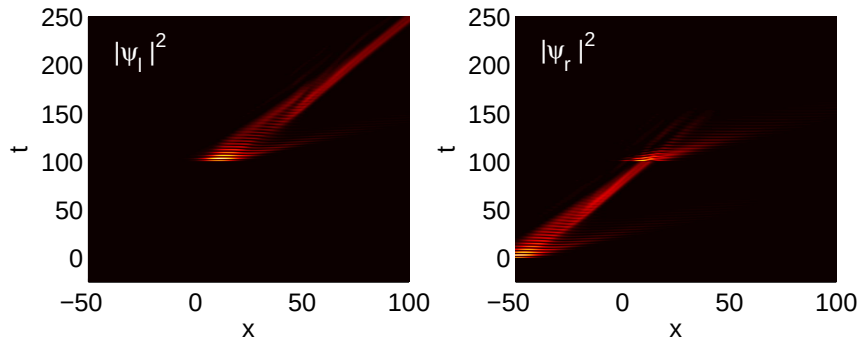

Figure 5-34: *Plot of the variation of $|\psi_l|^2$ and $|\psi_r|^2$ with time, illustrating the switching between the elliptically polarized solitons at $E_p = 0.095$. The remaining parameters are given in figure 5-23. The right-handed soliton is excited at $t = 0$, through the initial right-handed seed. The second pulse that initiates the switch to the left-handed soliton occurs at $t = 100$.*

is noted. This wave travels at the phase velocity of the linear system. The initial magnitude of these dispersive waves increases as the temporal width of the seed pulse is decreased.

In the absence of TE-TM splitting, it is unsurprising that a TE pulse will not excite a TM soliton. However when $\eta \neq 0$, a sufficiently strong and broad TE pulse can give the impression that a TM soliton is excited, but this is not a direct process, rather it is a two-step process where the pulse initially begins to excite an elliptically polarized soliton. When the pulse is sufficiently strong and broad, the initial elliptical soliton can be close to forming whilst the pulse is present. The effect of the persistent TE pulse acts on the newly formed soliton as if it were a separate pulse that excites the elliptical soliton to a linearly polarized state. We note that this transfer can only occur when multiple soliton branches exist at the same pump intensity, and thus switching of solitons from one branch to another can only occur when the system is pumped with a linear polarization.

5.8 Summary

In this chapter, we have seen that the eigenvectors of the linearized system are the linearly polarized states, and determined the existence condition for side branches that possess a different polarization from the pump. These side branches exist for linearly polarized pumps exclusively, where they emerge and rejoin the main homogeneous branch at its turning points. A brief study of vortices has revealed

that the polarized vortices separate into left and right handed components which are seen to evolve independently in the presence of $TE - TM$ splitting.

Following which, we have confirmed that a set of stable honeycomb vortices exists for circular and linearly polarized pumps, in the limit of small η. In contrast to the scalar case, there are numerous points where stable lattices can exist. Away from these lines of stability, the dynamics are seen to be identical to those observed in the scalar case. When $\eta \neq 0$, the separation of $|\psi_r\rangle$ and $|\psi_l\rangle$ allows the two polarized components to possess different velocities, and the associated lattice will evolve independently. For each component, the dynamics are seen to match that for the scalar case.

Solitons within the polarized system exist within the bistable regimes, with a polarization that is fixed by the polarization of the homogeneous system, along each branch except in the special case of linear polarizations. For which, the two degenerate elliptically polarized branches emerge from the first turning point as a pitchfork bifurcation, and sit upon the same linearly polarized background associated with the lower branch regardless of the soliton's polarization.

Under a Gaussian pumping regime, solitons can be seen to exist within the one-dimensional system for a circularly polarized pump. These solitons survive only within a region that extends approximately one standard deviation from the pump maximum, which corresponds to the extent of the bistable region. Similarly, it is seen that within two-dimensional systems, solitons evolve in an analogous form to that observed in the one-dimensional system, such that they survive up until it reaches the edge of the bistable domain. After that point, it is seen that the solitons relax back to the initial homogeneous solution. For a super-Gaussian pumping regime, the group velocity of the solitons matches that associated with a flat pumping regime. This is not the case for Gaussian beams, instead there is a gradual decrease in this group velocity, as it travels towards the boundary. Once this is reached the group velocity rapidly tends to zero.

Qualitatively, the dynamics of vector solitons and scalar solitons are equivalent, where they each exhibit growth and contraction along the axis that is perpendicular to the pump. The Maxwell point for elliptically polarized solitons occurs at a lower pump intensity than for linearly polarized systems, where there exists a stable region of solutions just below it. As the splitting increases, the location of these points and the associated stable regions shifts towards higher pump intensities. Similarly, it is seen that stable vector parametric cavity solitons localized along the y-axis can exist around the Maxwell point. The dynamics of

which correspond to those observed in the scalar model.

As the polarization of the pump is moved away from a linear polarization, the three bistable regions become increasingly separated in energy, whilst one of them disappears. In each region, a soliton branch exists, although only the first of these branches as aligned with the dominant circular polarization is always stable.

When an additional pulse is present, it is possible to transform between elliptically and linearly polarized solitons. These elliptically polarized solitons are particularly robust. If an antiphase pulse disables one component, the surviving component is capable of restoring it, provided that the pulse is not substantially stronger than the seed that originally excited the soliton.

In this chapter, the work on solitons is strongly connected to the experimental study by Sich *et al.* [161], where the first observations of exciton-polariton solitons was reported. These observed solitons were by elliptically polarized and are in good agreement with the theory discussed here.

CHAPTER 6

Conclusions

We conclude this work with a brief review of the salient findings reported herein on modulation instability, vortices and solitons. Afterwards, we discuss the significance of this work with respect to the recent theoretical and practical applications in the field. Finally, we highlight an instance which could serve as a motivation for future research.

On Modulation Instability

We began by discussing modulation instabilities within the exciton polariton system. We have discussed the strongly coupled system, wherein we illustrated the presence of parametric amplification for a homogeneous pumping region, through a study of the stability of the system along the lower polariton branch. From this, we proceeded to examine the stability of the system under a Gaussian regime.

For this Gaussian pumping, the main features associated with the homogeneous regime are preserved, however motion within the pump region serves to produce a roll pattern. Beyond which, we have derived the strongly coupled roll solution and studied its stability. Through this, it was seen that instability in the roll solution results in the generation of a weak standing wave with momentum, $\vec{k} \approx 3\vec{k_p}$.

On Vortices and Lattices

Through perturbative, variational approaches and direct numerical modeling, it has been observed that there is a minimum potential dependent value of detuning parameter. Increasing the strength of the potential, or increasing the winding number of the vortex results in the cut off shifting to progressively higher energies. The number of particles contained within the vortex is observed to increase, as one approaches resonance.

The stability of the stationary system in the absence of loss or gain has been analyzed, and it has been found that $m = 1$ vortices are stable over the entire range of possible detuning parameters. In contrast, higher order ($m = n$) vortices have been observed to be unstable over the whole range, and decay into n $m = 1$ vortices.

In the presence of loss and gain, the model has been observed to permit the spontaneous formation of localized vortex-antivortex pairs in addition to pattern formation, when the system is pumped at energies within the region of parametric instability, along the upper branch of the bistability diagram.

For a single seed vortex with a momentum located in the signal band of the system, vortex-antivortex pairs are observed to form within signal and idler bands, where this pair is pinned to the location of the seed. This localization results from the Gaussian pump acting as an effective potential for the signal and idler bands. The signal(idler) vortices (antivortices) are seen to remain be stable and travel towards the boundaries of the excitation region with a velocity determined by the pump momentum.

For polarized vortices separate into left and right handed components which are seen to evolve independently in the presence of $TE - TM$ splitting.

For honeycomb lattices, it is possible to obtain a quasi-stable lattice. These stable solutions can only be achieved when the growth rates associated with the Fourier components that compose the lattice are equal. Otherwise, adjacent vortices and antivortices merge. These effects have also been observed for square lattices. From which, it appears reasonable to conclude that provided one can position the Fourier components such that they possess equal gain, lattices of arbitrary shapes can be supported. Away from the boundaries of a non-flat pump, the same effects are observed. Finally, we discussed the origin of the drift velocity for the roll solutions, single vortices and vortex lattices.

Following which, we have confirmed that there exists a set of stable honeycomb vortices for linearly and circularly polarized pumps, in the limit of small η. In

contrast to the unpolarized case, it is seen that there are numerous points where stable lattices can exist. When $\eta \neq 0$, the two polarized components to possess different velocities, and the lattice evolve independently, while the dynamics of each component match those for the scalar case. In this situation, there can be no vortex lattices wherein both polarizations possess the same velocity and remain stable.

On Solitons

In a system pumped with a Gaussian beam, solitons exist in the one-dimensional system inside a region that extends approximately one standard deviation around the pump maximum. Similarly, two dimensional solitons will evolve in an analogous manner until they reach the boundary of the bistable region where they relax back to the background.

Vector solitons in polarized systems exist in all bistable regimes, with a polarization that is fixed by the polarization of the appropriate branch of the homogeneous system. In the circularly polarized case, these solitons correspond to those found in the scalar system.

As the pump polarization is made increasingly elliptical, the presence of a second bistable region and corresponding soliton branch has been noted. Only solitons on the first of these branches are always stable, as it is aligned with the dominant circular polarization. When the system is pumped with a linearly polarized beam, then these three branches emerge from the turning point, as a pitchfork bifurcation sitting upon the same linearly polarized background that is associated with the lower branch of the homogeneous solution.

Qualitatively, the dynamics of polarized solitons are equivalent those of scalar solitons, where they exhibit both growth and contraction along the axis that is perpendicular to the pump. The Maxwell point for elliptically polarized solitons occurs at a lower pump intensity than for linearly polarized systems, yet a stable region of solutions exist just below the point. As the splitting increases, the location of these points and the associated stable regions shifts towards higher pump intensities. Similarly, it is seen that stable vector parametric cavity solitons that are localized along the y-axis can exist close to the Maxwell point, where the dynamics correspond to those associated with the well-studied scalar case.

It is possible to transform between elliptically and linearly polarized solitons, using an additional pulse. These elliptically polarized solitons are particularly robust, such that if an antiphase pulse disables one component then the surviving

component is capable of restoring it, provided that the pulse is not substantially stronger than the seed that originally excited the soliton.

Outlook

In recent times, there have numerous reports of polaritons forming a coherent state[6, 74, 148, 147]. These papers amongst others demonstrate the intense interest in the area. This interest has been focused on two particular questions.

In some respects, the coherent state formed by exciton-polaritons can be treated as a non-equilibrium Bose-Einstein condensate or as a polariton laser, however the terminology used in the field remains rather confused such that no universal agreement exists on which of these terms is valid[22]. We recall that a condensate can be characterized through the conditions[82]

- Local thermal equilibrium
- A Landau critical velocity
- Quantized vortices
- Solitary waves
- Two-fluid hydrodynamics
- Metastable persistent flow

where as discussed in the introduction, not all of these properties are satisfied for exciton-polaritons in microcavities, while the ones that are fulfilled arise through different mechanisms than for atomic condensates. In particular, it has been proposed[22] that the reported superfluid effects can be explained through the suppression of scattering through a disorder potential. A polariton laser on the other hand, does not require thermal equilibrium while retaining the remaining characteristics.

Irrespective of these differences in the terminology, solitons and vortices can be observed in both in true Bose-Einstein condensates and in lasers and have recognized uses in both fields. Particularly in the paper [161], we have shown that the presence of solitons with a controllable polarization in the linearly pumped system have the potential to be used in optical logic gates, wherein they act as substitute for the electron the corresponding electronic equivalent. As a result of these properties, exciton polariton solitons could be used to aid work in producing

a future generation of information-processing devices[140]. In addition, to these more conventional uses of solitons in exciton-polariton systems, there have been some proposal to use polarized vortices in such systems as a means to model black-holes in a laboratory[172] at room-temperatures to make the study of event horizons as observed[95] in atomic Bose-Einstein condensate at low temperatures.

Regardless of the exact terminology that is eventually chosen, the underlying physics of microcavity polaritons is a particularly rich field for study because of the differences between their dynamics and those of Bose-Einstein condensates or lasers.

APPENDIX A

Appendix: Numerical Methods

In this appendix, we outline the main numerical methods used in the text. Over its duration, we have frequently utilized Newton's method to determine the $1D$ solution under Gaussian pumping in both the scalar and vector case in addition to determining the profiles of stationary vortices within a potential along one axis. Initially, we discuss the implementation of this method. After which, we illustrate the methods utilized for studying the evolution of every system covered in the document.

A.1 Newton's Method

In numerical computation, Newton's method [129] allows one to determine progressively better approximations to the root of a system of nonlinear equations. This method utilizes the Taylor expansion

$$f(\vec{x_0}+\vec{\epsilon}) = f(\vec{x_0}) + \frac{d}{d\vec{x}}f(\vec{x_0})\vec{\epsilon} + \frac{1}{2}\frac{d^2}{d\vec{x}^2}f(\vec{x_0})\vec{\epsilon}^2 + O(\vec{\epsilon}^3) \tag{A.1}$$

for a system of equations, $f(\vec{x})$. Now neglecting all but the lowest order terms, and requiring that $f(\vec{x_0}+\vec{\epsilon}) = 0$ yields

$$\vec{\epsilon_0} = -f(\vec{x_0})/J(x_0) \tag{A.2}$$

where the (i,j)-element of the Jacobian matrix, J is given as

$$J_{i,j} = \frac{d}{dx_j} f_i \tag{A.3}$$

This provides a first order correction to the location of the root, in an iterative manner, such that the root can be found through the relation

$$\hat{x}_{n+1} = \hat{x}_n - \frac{f(x_n)}{J(x_n)} \tag{A.4}$$

where x_n corresponds to the $n-th$ approximation to the root starting from an initial guess x_0, however computing the inverse of the Jacobian can be computationally expensive, and as such one often rewrites equation A.4 as

$$J(x_n)(\hat{x}_{n+1} - \hat{x}_n) = -f(x_n) \tag{A.5}$$

and solves for the unknown function $(\hat{x}_{n+1} - \hat{x}_n)$. This method is known to converge quadratically provided x_n is sufficiently close to the root, such that it exists in that particular root's basin of attraction.

A.2 Time Evolution

We first proceed to express the system as a sum of matrices containing linear and nonlinear components such that, one has

$$\frac{d}{dt}\begin{bmatrix} E(x,y) \\ \psi(x,y) \end{bmatrix} = \begin{pmatrix} L & i\Omega_R \\ i\Omega_R & Q \end{pmatrix} \cdot \begin{bmatrix} E(x,y) \\ \psi(x,y) \end{bmatrix} \tag{A.6}$$

where

$$L = i\nabla^2 + i\delta_p + iU(x,y) - \gamma_{ph} + E_p e^{ik_p x}$$

$$Q = i\delta_e - i|\psi|^2 - \gamma_e \tag{A.7}$$

which has the general solution

$$|\phi(t)\rangle = exp((S_L + S_{NL})t) \cdot |\phi(0)\rangle \tag{A.8}$$

with

$$|\phi(0)\rangle = \begin{pmatrix} E(0) \\ \psi(0) \end{pmatrix} \tag{A.9}$$

where it is seen that we have a linear step defined through the matrix

$$S_L = \begin{bmatrix} i\nabla^2 & 0 \\ 0 & 0 \end{bmatrix} \tag{A.10}$$

and a nonlinear step

$$S_{NL} = -\begin{bmatrix} \gamma_{ph} - i\delta_p - iU(x,y) - E_p e^{ik_p x} & -i\Omega_R \\ -i\Omega_R & \gamma_e - i\delta_p + i|\psi|^2 \end{bmatrix} \tag{A.11}$$

$$\begin{aligned} e^{A+B} &= e^A e^B e^{[A,B]} \\ e^{A+B} &= e^{A/2} e^B e^{A/2} \end{aligned} \tag{A.12}$$

Using the Campbell-Baker-Hausdorf theorem [117], displayed in equation A.12, one obtains

$$\phi(t) = e^{iS_L\tau} e^{iS_{NL}\tau} \phi(0) \tag{A.13}$$

Given that the linear component contains momentum dependent terms, it is convenient to transform the solution vector into momentum space through Fourier transforms such that one has

$$\phi(t) = e^{iS_{NL}t} I F e^{iS_L^F t} F \phi(0) \tag{A.14}$$

where in momentum space the linear part becomes

$$S_L^F = \begin{bmatrix} ik_p^2 & 0 \\ 0 & 0 \end{bmatrix} \tag{A.15}$$

Now, while it is feasible to solve this system, the presence of the matrix exponentials makes it convenient to separate the system to yield

$$\begin{aligned} \phi(t)^1 &= IF\left[e^{iS_L^F\tau}F\left[\phi(0)\right]\right] \\ \frac{d}{dt}\phi(t) &= S_{NL}\phi(t)^1 \end{aligned} \tag{A.16}$$

where the second step is performed through a 4th order Runge-Kutta method [129], as displayed through

$$v_{n+1} = v_n + \frac{1}{6}\left(k_1 + 2k_2 + 2k_3 + k_4\right) \tag{A.17}$$

where

$$\begin{aligned} k_1 &= hf(v_n, q_n) \\ k_2 &= hf(v_n + \frac{h}{2}, q_n + \frac{k_1}{2}) \\ k_3 &= hf(v_n + \frac{h}{2}, q_n + \frac{k_2}{2}) \\ k_4 &= hf(v_n + h, q_n + k_3) \end{aligned}$$

and

$$f(v_n, y_n) = -\begin{bmatrix} \gamma_c - i\Delta - iU(x,y) & -i\Omega_R \\ -i\Omega_R & \gamma_0 - i\Delta + i|\psi|^2 \end{bmatrix} \cdot \begin{bmatrix} E_n(r) \\ \psi_n(r) \end{bmatrix}$$

Through this split-step evolution, we are able to stably evolve the polariton system.

List of Figures

Bibliography

[1] A. A. Abrikosov, *On the magnetic properties of superconductors of the second group*, Soviet Physics JETP, 5 (1957), p. 1174.

[2] C. Adrados, T. C. H. Liew, A. Amo, M. D. Martin, D. Sanvitto, C. Anton, E. Giacobino, A. Kavokin, A. Bramati, and L. Vina, *Motion of spin polariton bullets in semiconductor microcavities*, Physical Review Letters, 107 (2011), p. 146402.

[3] V. V. Afanasyev, Y. S. Kivshar, V. V. Konotop, and V. V. Konotop, *Dynamics of coupled dark and bright optical solitons*, Optics Letters, 14 (1989), p. 805.

[4] G. P. Agrawal, *Nonlinear Fiber Optics*, Academic Press, 2001.

[5] N. Akhmediev and A. Ankiewicz, eds., *Dissipative Solitons: Lecture Notes in Physics, Volume 661*, Springer, 2005.

[6] A. Amo, J. Lefrere, S. Pigeon, C. Adrados, C. Ciuti, I. Carusotto, R. Houdre, E. Giacobino, and A. Bramati, *Superfluidity of polaritons in semiconductor microcavities*, Nature, 5 (2009), p. 805.

[7] A. Amo, T. C. H. Liew, C. Adrados, E. Giacobino, A. V. Kavokin, and A. Bramati, *Anisotropic optical spin hall effect in semiconductor microcavities*, arxiv:0906.0746, (2009).

[8] A. Amo, T. C. H. Liew, C. Adrados, R. Houdre, E. Giacobino, A. V. Kavokin, and A. Bramati, *Exciton-polariton spin switches*, Nature Photonics, 4 (2010), p. 361.

[9] A. Amo, S. Pigeon, D. Sanvitto, V. G. Sala, R. Hivet, I. Carusotto, F. Pisanello, G. Lemenager, R. Houdre, E. Giacobino, c Ciuti, and A. Bramati, *Polariton superfluids reveal quantum hydrodynamic solitons*, Science, 332 (2011), p. 1167.

[10] A. Amo, D. Sanvitto, F. P. Laussy, D. Ballarini, E. del Valle, M. D. Martin, A. Lemaitre, J. Bloch, D. N. Krizhanovskii, M. S. Skolnick, C. Tejedor, and L. Vina, *Collective fluid dynamics of a polariton condensate in a semiconductor microcavity*, Nature, 457 (2008), p. 291.

[11] L. C. Andreani, F. Tassone, and F. Bassani, *Radiative lifetime of free excitons in quantum wells*, Solid State Communications, 77 (1991), p. 641.

[12] A. Armitage, T. A. Fisher, M. S. Skolnick, D. M. Whittaker, P. Kinsler, and J. S. Roberts, *Exciton polaritons in semiconductor quantum microcavities in a high magnetic field*, Physical Review B, 55 (1996), p. 16395.

[13] N. W. Ashcroft and D. N. Mermin, *Solid State Physics*, New York, 1977.

[14] R. Balili, V. Hartwell, D. Snoke, L. Pfeiffer, and K. West, *Bose-einstein condensation of microcavity polaritons in a trap*, Science, 316 (2007), pp. 1007–1010.

[15] D. Baxter, M. S. Skolnick, A. Armitage, V. N. Astratov, D. M. Whittaker, T. A. Fisher, J. S. Roberts, D. J. Mowbray, and M. A. Kaliteevski, *Polarization-dependent phenomena in the reflectivity spectra of semiconductor quantum microcavities*, Physical Review B, 56 (1997), p. R10032.

[16] O. L. Berman, Y. E. Lozovik, and D. W. Snoke, *Theory of bose-einstein condensation and superfluidity of two-dimensional polaritons in an in-plane harmonic potential*, Physical Review B, 77 (2008), p. 155317.

[17] M. Berry, *Making waves in physics - three wave singularities from the miraculous 1830s*, Nature, 403 (2000), p. 21.

[18] M. O. Borgh, J. Keeling, and N. G. Berloff, *Spatial pattern formation and polarization dynamics of a nonequilibrium spinor polariton condensate*, Physical Review B, 81 (2010), p. 235302.

[19] M. Born and E. Wolf, *Principles of Optics*, Cambridge University Press, 1999.

[20] M. Brambilla, T. Maggipinto, I. M. Perrini, S. Barbay, and R. Kuszelewicz, *Modeling pattern formation and cavity solitons in quantum dot*

optical microresonators in absorbing and amplifying regimes, Chaos, 17 (2007), p. 037119.

[21] A. Brunetti, M. Vladimirov, D. Scalbert, R. Andre, D. Solnyshkov, G. Malpuech, I. A. Shelykh, and A. V. Kavokin, *Coherent spin dynamics of exciton-polaritons in diluted magnetic microcavities*, Physical Review B, 73 (2006), p. 205337.

[22] L. V. Butov and A. V. Kavokin, *The behaviour of exciton-polaritons*, Nature Photonics, 6 (2012), p. 2.

[23] H. B. Callen, *Thermodynamics and an introduction to thermostatistics*, John Wiley, 1985.

[24] R. Carretero-Gonzalez, D. J. Frantzeskakis, and P. G. Kevrekidis, *Nonlinear waves in bose-einstein condensates: Physical relevance and mathematical techniques*, Nonlinearity, 21 (2008), p. R139.

[25] I. Carusotto and C. Ciuti, *Spontaneous microcavity-polariton coherence across the parametric threshold: Quantum monte carlo studies*, Physical Review B, 72 (2006), p. 125335.

[26] I. Carusotto and C. Ciuti, *Probing microcavity polariton superfluidity through resonant rayleigh scattering*, Physical Review Letters, 93 (2004), p. 166401.

[27] Y. Chen, A. Tredicucci, and F. Bassani, *Bulk exciton polaritons in gaas microcavities*, Physical Review B, 52 (1995), p. 1800.

[28] D. N. Christodoulides and R. I. Joseph, *Vector solitons in birefringent nonllinear dispersive media*, Optics Letters, 13 (1988), p. 53.

[29] S. Christopoulos, G. B. H. von Hogersthal, A. J. D. Grundy, P. G. Lagoudakis, A. V. Kavokin, and J. J. Baumberg, *Room-temperature polariton lasing*, Physical Review Letters, 98 (2007), p. 126405.

[30] C. Ciuti and I. Carusotto, *Quantum fluid effects and parametric instabilities in microcavities*, Physica Status Solidi B-Basic Solid State Physics, 242 (2005), pp. 2224–2245.

[31] C. Ciuti, P. Schwendimann, B. Deveaud, and A. Quattropani, *Nonlinear optics of exciton-polaritons in semiconductor microcavities*, in Proc. Conference Digest Quantum Electronics Conference 2000 International, 2000, pp. 1 pp.–.

[32] C. Ciuti, P. Schwendimann, and A. Quattropani, *Theory of polariton parametric interactions in semiconductor microcavities*, Semiconductor Science And Technology, 18 (2003), pp. S279–S293.

[33] G. Cocoletzi and W. Mochan, *Excitons: from excitations at surfaces to confinement in nanostructures*, Surface Science Reports, 57 (2005), pp. 1–58.

[34] J. Dalibard and J. M. Raimond, *Fundamental Systems in Quantum Optics*, North-Holland, 1992.

[35] G. Dasbach, M. Schwab, M. Bayer, and A. Forchel, *Impact of optical confinement on parametric polariton scattering in microcavities*, in Technical Digest. Summaries of Papers Presented at the Quantum Electronics and Laser Science Conference QELS '02, 2002, pp. 57–58.

[36] H. Deng, H. Haug, and Y. Yamamoto, *Exciton-polariton bose-einstein condensation*, Reviews of Modern Physics, 82 (2010), p. 1489.

[37] H. Deng, G. S. Solomon, R. Hey, K. H. Ploog, and Y. Yamamoto, *Spatial coherence of a polariton condensate*, Physical Review Letters, 99 (2007), p. 126403.

[38] A. S. Desyatnikov, Y. S. Kivshar, and L. Torner, *Optical vortices and vortex solitons*, Progress in Optics, 47 (2005), p. 6.

[39] B. Deveaud, ed., *The Physics of Semiconductor Microcavities: From Fundamentals to Nanoscale Devices*, Wiley, 2007.

[40] A. Dreischuh, S. Chervenkov, D. Neshev, G. G. Paulus, and H. Walther, *Generation of lattice structures of optical vortices*, Journal of the Optical Society of America B, 19 (2002), p. 550.

[41] K. Dysthe, H. E. Krogstad, and P. Muller, *Oceanic rogue waves*, Annual Review of Fluid Mechanics, 40 (2008), p. 287.

[42] O. A. Egorov, A. V. Gorbach, F. Lederer, and D. V. Skryabin, *Two-dimensional localization of exciton-polaritons in microcavities*, Physical Review Letters, 105 (2010), p. 073903.

[43] O. A. Egorov, D. V. Skryabin, and F. Lederer, *Polariton solitons due to saturation of the exciton-photon coupling*, ..., ... (2010), p. ...

[44] O. A. Egorov, D. V. Skryabin, A. V. Yulin, and F. Lederer, *Bright cavity polariton solitons*, Physical Review Letters, 102 (2009), p. 153904.

[45] B. Eiermann, T. Anker, M. Albiez, M. Taglieber, P. Treutlein, K. P. Marzlin, and M. K. Oberthaler, *Bright bose-einstein gap solitons of atoms with repulsive interaction*, Physical Review Letter, 92 (2004), p. 230401.

[46] A. Fainstein, B. Jusserand, P. Senellart, J. Bloch, V. Thierry-Mieg, and R. Planel, *Center-of-mass quantized exciton polariton states in bulk-gaas microcavities*, Physical Review B, 62 (2000), p. 8199.

[47] A. L. Fetter and A. A. Svidzinsky, *Vortices in a trapped dilute bose-einstein condensate*, Journal of Physics: Condensed Matter, 13 (2001), p. R135.

[48] W. J. Firth and A. J. Scroggie, *Optical bullet holes: Robust controllable localized states of a nonlinear cavity*, Physical Review Letters, 76 (1996), p. 1623.

[49] W. J. Firth, A. J. Scroggie, and G. S. McDonald, *Hexagonal patterns in optical bistability*, Physical Review A, 46 (1992), p. R3609.

[50] T. A. Fisher, A. M. Afshar, D. M. Whittaker, M. S. Skolnic, J. S. Roberts, G. Hill, and M. A. Pate, *Electric-field and temperature tuning of exciton-photon coupling in quantum microcavity structures*, Physical Review B, 51 (1994), p. 2600.

[51] H. Flayac, I. A. Shelykh, D. D. Solnyshkov, and G. Malpuech, *Topological stability of the half-vortices in spinor exciton-polariton condensates*, Physical Review B, 81 (2010), p. 045318.

[52] M. Fox, *Optical properties of solids*, Oxford, New York, 2001.

[53] G. Gibson, J. Courtial, M. J. Padgett, M. Vasnetsov, V. Pas'ko, S. M. Barnett, and S. Franke-Arnold, *Free-space information transfer using light beams carrying orbital angular momentum*, Optics Express, 12 (2004), p. 5448.

[54] N. A. Gippius, I. A. Shelykh, D. D. Solnyshkov, S. S. Gavrilov, Y. G. Rubo, A. V. Kavokin, S. G. Tikhodeev, and G. Malpuech, *Polarization multistability of cavity polaritons*, Physical Review Letters, 98 (2007), p. 236401.

[55] M. Glazov, H. Ouerdane, L. Pilozzi, G. Malpuech, A. Kavokin, and A. D'Andrea, *Polariton-polariton scattering in microcavities: A microscopic theory*, arXiv:0902.1410v1, (2009).

[56] M. M. Glazov and L. E. Golub, *Quantum and classical multiple-scattering effects in the spin dynamics of cavity polaritons*, Physical Review B, 77 (2008), p. 165341.

[57] A. V. Gorbach, R. Hartley, and D. V. Skryabin, *Vortex lattices in coherently pumped polariton microcavities*, Physical Review Letters, 104 (2010), p. 213903.

[58] D. G. Grier, *A revolution in optical manipulation*, Nature, 424 (2003), p. 810.

[59] A. Griffin, D. W. Snoke, and S. Stringari, *Bose-Einstein Condensation*, Cambridge University Press, 1995.

[60] H. Haken, *Synergetics. Introduction and Advanced Topics*, Springer, 2004.

[61] P. Halevi, ed., *Spatial Dispersion in Solids and Plasmas (Electromagnetic Waves, Recent Developments in Research)*, North Holland, Amsterdam, 1992.

[62] G. K. Harkness, W. J. Firth, G.-L. Oppo, and J. M. McSloy, *Computationally determined existence and stability of transverse structures. i. periodic optical patterns*, Physical Review E, 66 (2002), p. 046605.

[63] G. R. Hayes, S. Haacke, M. Kauer, R. P. Stanley, R. Houdre, U. Oesterle, and B. Deveaud, *Resonant rayleigh scattering versus incoherent luminescence in semiconductor microcavities*, Physical Review B, 58 (1998), p. R10175.

[64] N. R. Heckenberg, R. McDuff, C. P. Smith, and A. G. White, *Generation of optical phase singularities by computer generated holograms*, Optics Letters, 17 (1992), p. 221.

[65] J. J. Hopfield, *Theory of the contribution of excitons to the complex dielectric constant of crystals*, Physical Review, 112 (1958), p. 1555.

[66] J. J. Hopfield and D. G. Thomas, *Theoretical and experimental effects of spatial dispersion on the optical properties of crystals*, Physical Review, 132 (1963), pp. 563–572.

[67] R. Houdre, J. L. Gibernon, P. Pellandini, R. P. Stanley, U. Oesterle, C. Weisbuch, J. O'Gorman, B. Roucroft, and M. Ilegems, *Saturation of the strong-coupling regime in a semiconductor microcavity: Free-carrier bleaching of cavity polaritons*, Physical Review B, 52 (1995), p. 7810.

[68] R. Houdre, C. Weisbuch, R. P. Stanley, U. Oesterle, and M. Ilegems, *Linear and non-linear behavior of cavity polaritons*, May 2000.

[69] R. Houdre, C. Weisbuch, R. P. Stanley, U. Oesterle, and M. Ilegems, *Nonlinear emission of semiconductor microcavities in the strong coupling regime*, Physical Review Letters, 85 (2000), pp. 2793–2796.

[70] R. Houdre, C. Weisbuch, R. P. Stanley, U. Oesterle, P. Pellandini, and M. Ilegems, *Measurement of cavity-polariton dispersion curve from angle-resolved photoluminescence experiments*, Physical Review Letters, 73 (1994), pp. 2043–2046.

[71] A. Imamoglu, R. J. Ram, S. Pau, and Y. Yamamoto, *Nonequilibrium condensates and lasers without inversion: Exciton-polariton lasers*, Physical Review A, 53 (1996), p. 4250.

[72] J. D. Jackson, *Classical Electrodynamics*, Wiley, 1999.

[73] J. Karr, A. Baas, and E. Giacobino, *Twin polaritons in semiconductor microcavities*, Physical Review A, 69 (2004), p. 063807.

[74] J. Kasprzak, M. Richard, S. Kundermann, A. Baas, P. Jeambrun, J. M. J. Keeling, F. M. Marchetti, M. H. Szymanska, R. Andre, J. L. Staehli, V. Savona, P. B. Littlewood, B. Deveaud, and L. S. Dang, *Bose-einstein condensation of exciton polaritons*, Nature, 443 (2006), pp. 409–414.

[75] A. Kavokin, *Exciton-polaritons in microcavities: present and future*, Applied Physics A, 89 (2007), p. 241.

[76] A. Kavokin, J. J. Baumberg, G. Malpuech, and F. P. Laussy, *Microcavities*, Oxford University Press, 2007.

[77] A. Kavokin and G. Malpuech, *Cavity Polaritons*, Elsevier, 2003.

[78] A. Kavokin, G. Malpuech, and M. Glazov, *Optical spin hall effect*, Physical Review Letters, 95 (2005), p. 136601.

[79] A. V. Kavokin, *Motional narrowing of inhomogeneously broadened excitons in a semiconductor microcavity: Semiclassical treatment*, Physical Review B, 57 (1998), p. 3757.

[80] K. V. Kavokin, P. Renucci, T. Amand, X. Marie, P. Senellart, J. Bloch, and B. Sermage, *Linear polarisation inversion: A signature of coulomb scattering of cavity polaritons with opposite spins*, Physica Status Solidi C, 2 (2005), p. 763.

[81] J. Keeling and N. G. Berloff, *Spontaneous rotating vortex lattices in a pumped decaying condensate*, Physical Review Letters, 100 (2008), p. 250401.

[82] J. Keeling and N. G. Berloff, *Condensed-matter physics: Going with the flow*, Nature, 457 (2009), p. 273.

[83] J. Keeling and N. G. Berloff, *Controllable half-vortex lattices in an incoherently pumped polariton condensate*, arXiv:1102.5302v1 [cond-mat.quant-gas], (2011).

[84] S. Kena-Cohen and S. R. Forrest, *Room-temperature polariton lasing in an organic single-crystal microcavity*, Nature Photonics, 4 (2010), p. 371.

[85] L. Khaykovich, F. Schreck, G. Ferrari, T. Bourdel, J. Cubizolles, L. D. Carr, Y. Castin, and C. Salomon, *Formation of a matter-wave bright soliton*, Science, 296 (2002), p. 1290.

[86] Y. Kivshar and G. Agrawal, *Optical Solitons: From Fibers to Photonic Crystals*, Academic Press, 2001.

[87] Y. S. Kivshar, *Stable vector solitons composed of bright and dark pulses*, Optics Letters, 17 (1992), p. 1322.

[88] R. S. Knox, *Theory of Excitons*, Academic Press, 1963.

[89] D. J. Korteweg and G. de Vries, *On the change of form of long waves advancing in a rectangular canal and on a new type of long stationary waves*, Philosophical Magazine, 39 (1895), p. 422.

[90] N. Koumura, R. W. J. Zijlstra, R. A. van Delden, N. Harada, and B. L. Feringa, *Light-driven monodirectional molecular rotor*, Nature, 401 (1999), p. 152.

[91] D. N. Krizhanovskii, S. S. Gavrilov, A. P. D. Love, D. Sanvitto, N. A. Gippius, S. G. Tikhodeev, V. D. Kulakovskii, D. M. Whittaker, M. S. Skolnick, and J. S. Roberts, *Self-organization of multiple polariton-polariton scattering in semiconductor microcavities*, Physical Review B, 77 (2008), p. 115336.

[92] R. Kuszelewicz, I. Ganne, I. Sagnes, G. Sleks, and M. Brambilla, *Optical self-organization in bulk and multiquantum well gaalas microresonators*, Physical Review Letters, 84 (2000), p. 6006.

[93] K. G. Lagoudakis, M. Wouters, M. Richard, A. Baas, I. Carusotto, R. A. R, L. S. Dang, and B. Deveaud-Pledran, *Quantised vortices in an exciton-polariton condensate*, Nature, 4 (2008), pp. 706–711.

[94] P. G. Lagoudakis, P. G. Savvidis, J. J. Baumberg, D. M. Whittaker, P. R. Eastham, M. S. Skolnick, and J. S. Roberts, *Stimulated spin dynamics of polaritons in semiconductor microcavities*, Physical Review B, 65 (2002), p. 161310.

[95] O. Lahav, A. Itah, A. Blumkin, C. Gordon, S. Rinott, A. Zayats, and J. Steinhauer, *Realization of a sonic black hole analog in a bose-einstein condensate*, Physical Review Letters, 105 (2010), p. 240401.

[96] L. D. Landau and E. M. Lifshift, *Course in theoretical Physics : Volume 3 : Quantum Mechanics Non-relativistic Theory*, Pergamon Press, 1980.

[97] ——, *Course in theoretical Physics : Volume 9 : Statistical Physics part 2*, Pergamon Press, 1980.

[98] A. Laucht, N. Hauke, J. M. Villas-Boas, F. Hofbauer, M. Kaniber, G. Bohm, and J. J. Finley, *Dephasing of quantum dot exciton polaritons in electrically tunable nanocavities*, Physical Review Letters, 103 (2009), p. 087405.

[99] F. P. Laussy, G. Malpuech, A. V. Kavokin, and P. Bigenwald, *Coherence dynamics in microcavities and polariton lasers*, Journal of Physics: Condensed Matter, 16 (2004), p. S3665.

[100] K. J. H. Law, P. G. Kevrekidis, V. Koukouloyannis, I. Kourakis, D. J. Frantzeskakis, and A. R. Bishop, *Discrete solitons and vortices in hexagonal and honeycomb lattices: Existence, stability, and dynamics*, Physical Review E, 78 (2008), p. 066610.

[101] C. Leyder, T. C. H. Liew, A. V. Kavokin, I. A. Shelykh, M. Romaneli, J. P. Karr, E. Giacobino, and A. Bramati, *Interference of coherent polariton beams in microcavities: Polarization-controlled optical gates*, Physical Review Letters, 99 (2007), p. 196402.

[102] C. Leyder, M. Romaneli, J. P. Karr, E. Giacobino, T. C. Liew, M. M. Glazov, A. V. Kavokin, G. Malpuech, and A. Bramati, *Observation of the optical spin hall effect*, Nature, 3 (2007), p. 628.

[103] D. G. Lidzey, D. D. C. Bradley, M. S. Skolnick, T. Virgili, S. Walker, and D. M. Whittaker, *Strong exciton-photon coupling in an organic semiconductor microcavity*, Nature, 395 (1998), pp. 53–55.

[104] T. C. H. Liew, A. V. Kavokin, and I. A. Shelykh, *Excitation of vortices in semiconductor microcavities*, Physical Review B, 75 (2007), p. 241301.

[105] T. C. H. Liew, Y. G. Rubo, and A. V. Kavokin, *Generation and dynamics of vortex lattices in coherent exciton-polariton fields*, Physical Review Letters, 101 (2008), p. 187401.

[106] Y. E. Lozovik and A. G. Semenov, *Theory of superfluidity in a polariton system*, Theoretical and Mathematical Physics, 154 (2008), p. 319.

[107] L.Pitaevskii and S.Stringari, *Bose-Einstein Condensation*, Oxford University Press, 2003.

[108] L. A. Lugiato and R. Lefever, *Spatial dissipative structures in passive optical systems*, Physical Review Letters, 58 (1987), p. 2209.

[109] K. W. Madison, F. Chevy, W. Wohlleben, and J. Dalibard, *Vortex formation in a stirred bose-einstein condensate*, Physical Review Letters, 84 (2000), p. 806.

[110] G. Malpuech, J. J. Baumberg, A. Kavokin, and A. Di Carlo, *Ultralow threshold polariton lasing by electron cooling in doped microcavities*, in Technical Digest. Summaries of Papers Presented at the Quantum Electronics and Laser Science Conference QELS '02, 2002, pp. 58–.

[111] F. Manni, K. G. Lagoudakis, T. C. H. Liew, R. Andre, and B. Deveaud-Pledran, *Spontaneous pattern formation in a polariton condensate*, Physical Review Letters, 107 (2011), p. 106401.

[112] F. M. Marchetti and M. H. Szymanska, *Vortices in polariton opo superfluids*, arXiv:1107.4487v1 [cond-mat.mes-hall], (2011).

[113] F. M. Marchetti, M. H. Szymanska, C. Tejedor, and D. M. Whittaker, *Spontaneous and triggered vortices in polariton opo superfluids*, arxiv 1003.5111v1, (2010).

[114] M. D. Martin, L. Vina, J. K. Son, and E. E. Mendez, *Spin dynamics of cavity polaritons*, Solid State Communications, 117 (2001), pp. 267–271.

[115] F. Meier and B. P. Zakharchenya, *Optical Orientation*, New York: North Holland, 1984.

[116] D. Mermin, *The topological theory of defects in ordered media*, Reviews of Modern Physics, 51 (1979), p. 591.

[117] A. Messiah, *Quantum Mechanics, volume I*, North Holland, 1961.

[118] M. Muller, J. Bleuse, R. Andre, and H. Ulmer-Tuffigo, *Observation of bottleneck effects on the photoluminescence from polaritons in ii-vi microcavities*, Dec. 1999.

[119] S. D. Nagel L, ed., *1991 Lectures in Complex Systems*, Addison-Wesley, 1992.

[120] T. Ostatnicky, D. Read, and A. V. Kavokin, *Polarization and depolarization in scattering of cavity polaritons*, Physical Review B, 80 (2009), p. 115328.

[121] T. Ostatnicky, I. A. Shelykh, and A. V. Kavokin, *Theory of polarisation-controlled polariton logic gates*, Physical Review B, 81 (2010), p. 125319.

[122] G. Panzarini, L. C. Andreani, A. Armitage, D. Baxter, M. S. Skolnick, V. N. Astratov, J. S. Roberts, A. V. Kavokin, M. R. Vladimirov, and M. A. Kaliteevski, *Exciton-light coupling in single and coupled semiconductor microcavities: Polariton dispersion and polarization splitting*, Physical Review B, 59 (1999), p. 5082.

[123] G. Panzarini, L. C. Andreani, A. Armitage, D. Baxter, M. S. Skolnick, V. N. Astratov, J. S. Roberts, A. V. Kavokin, M. R. Vladimirov, and M. A. Kaliteevski, *Cavity-polariton dispersion and polarization splitting in single and coupled semiconductor microcavities*, Physics of the Solid State, 41 (2006), p. 1223.

[124] S. Pau, H. Cao, G. Bjork, Y. Yamamoto, and A. Imamoglu, *Observation of a laserlike transition in a microcavity exciton polariton system*, Physical Review A, 54 (1996), p. R1789.

[125] O. Penrose and L. Onsager, *Bose-einstein condensation and liquid helium*, Physical Review, 104 (1956), p. 576.

[126] S. Pigeon, I. Carsusotto, and C. Ciuti, *Hydrodynamic nucleation of vortices and solitons in a resonantly excited polariton superfluid*, Physical Review B, 83 (2011), p. 144513.

[127] D. Pines and P. Nozieres, *The Theory of Quantum Liquids*, Addison-Wesley, 1966.

[128] L. Pismen, *Vortices in Nonlinear Fields*, Oxford University Press, 1999.

[129] W. H. Press, S. A. Teukolsky, W. T. Vetterling, and B. P. Flannery, *Numerical Recipes in Fortran 77*, Cambridge, 1992.

[130] E. M. Purcell, H. C. Torrey, and R. V. Pound, *Resonance absorption by nuclear magnetic moments in a solid*, Physical Review, 69 (1946), p. 37.

[131] C. Raman, J. R. Abo-Shaeer, J. M. Vogels, K. Xu, and W. Ketterle, *Vortex nucleation in a stirred bose-einstein condensate*, Physical Review Letters, 87 (2001), p. 210402.

[132] D. Read, T. C. H. Liew, Y. G. Rubo, and A. V. Kavokin, *Stochastic polarization formation in exciton-polariton bose-einstein condensates*, Physical Review B, 80 (2009), p. 195309.

[133] J. P. Reithmaier, G. Sek, A. Loffler, C. Hofmann, S. Kuhn, S. Reitzenstein, L. V. Keldysh, V. D. Kulakovskii, T. L. Reinecke, and A. Forchel, *Strong coupling in a single quantum dot-semiconductor microcavity system*, Nature, 432 (2004), pp. 197–200.

[134] P. Renucci, T. Amand, and X. Marie, *Coherent spin dynamics of polaritons in semiconductor microcavities*, Semiconductor Science And Technology, 18 (2003), p. S361.

[135] P. Renucci, T. Amand, X. Marie, P. Senellart, J. Bloch, B. Sermage, and K. V. Kavokin, *Microcavity polariton spin quantum beats without a magnetic field: A manifestation of coulomb exchange in dense and polarized polariton systems*, Physical Review B, 72 (2005), p. 075317.

[136] M. Richard, J. Kasprzak, A. Baas, K. Lagoudakis, M. Wouters, I. Carusotto, R. Andre, B. Deveaud-Pledran, and L. S. Dang, *Exciton-polariton bose-einstein condensation: Advances and issues*, International Journal of Nanotechnology, 7 (2010), p. 668.

[137] G. Rochat, C. Ciuti, V. Savona, C. Piermarocchi, A. Quattropani, and P. Schwendimann, *Excitonic bloch equations for a two-dimensional system of interacting excitons*, PHYSICAL REVIEW B, 61 (1999), p. 13856.

[138] S. L. Rolston and W. D. Phillips, *Nonlinear and quantum atom optics*, Nature, 416 (2002), p. 219.

[139] M. Romanelli, C. Leyder, J. P. Karr, E. Giacobino, and A. Bramati, *Four wave mixing oscillation in a semiconductor microcavity: Generation of two correlated polariton populations*, Physical Review Letters, 98 (2007), p. 106401.

[140] N. N. Rosanov, *Dissipative polariton solitons: Proof of existence*, Nature Photonics, 6 (2012), p. 6.

[141] G. Roumpos, M. D. Fraser, A. Loffler, S. Hofling, A. Forchel, and Y. Yamamoto, *Single vortex-antivortex pair in an exciton-polariton condensate*, Nature Physics, 1841 (2010).

[142] G. Ruben, M. J. Morgan, and D. M. Paganin, *Texture control in a pseudospin bose-einstein condensate*, Physical Review Letters, 105 (2010), p. 220402.

[143] G. Ruben, D. M. Paganin, and M. J. Morgan, *Vortex-lattice formation and melting in a nonrotating bose-einstein condensate*, Physical Review A, 78 (2008), p. 013631.

[144] Y. G. Rubo, *Half vortices in exciton polariton condensates*, Physical Review Letters, 99 (2007), p. 106401.

[145] J. S. Russell, *Report on waves*, in Fourteenth meeting of the British Association for the Advancement of Science, 1844.

[146] M. Saba, C. Ciuti, J. Bloch, V. Thierry-Mieg, R. Andre, L. S. Dang, S. Kundermann, A. Mura, G. Bongiovanni, J. L. Staehli, and B. Deveaud, *High-temperature ultrafast polariton parametric amplification in semiconductor microcavities*, Nature, 414 (2001), pp. 731–735.

[147] D. Sanvitto, F. M. Marchetti, M. H. Szymanska, G. Tosi, M. Baudisch, F. Laussy, D. N. Krizhanovskii, M. S. Skolnick, L. Marrucci, A. Lemaître, J. Bloch, C. Tejedor, and L. Vina, *Persistent currents and quantized vortices in a polariton superfluid*, Nature Physics, 6 (2010), p. 527.

[148] D. Sanvitto, S. Pigeon, A. Amo, D. Ballarini, M. D. Giorgi, I. Carusotto, R. Hivet, F. Pisanello, V. G. Sala, P. S. S. Guimaraes, E. Giacobino, C. Ciuti, A. Bramati, and G. Gigli, *All-optical control of the quantum flow of a polariton condensate*, Nature Photonics, 5 (2011), p. 610.

[149] V. Savona, C. Piermarocchi, A. Quattropani, P. Schwendimann, and F. Tassone, *Optical properties of microcavity polaritons*, Phase Transitions, 68 (1999), pp. 169–279.

[150] V. Savona and D. Sarchi, *Bose-einstein condensation of microcavity polaritons*, Physica Status Solidi B, 242 (2005), p. 2290.

[151] P. G. Savvidis, J. J. Baumberg, R. M. Stevenson, M. S. Skolnick, D. M. Whittaker, and J. S. Roberts, *Angle-resonant stimulated polariton amplifier*, Physical Review Letters, 84 (2000), pp. 1547–1550.

[152] D. Scalbert, M. Vladimirov, A. Brunetti, S. Cronenberger, M. Nawrocki, J. Bloch, A. V. Kavokin, I. A. Shelykh, R. Andre, D. Solnyshkov, and G. Malpuech, *Polariton spin beats in semiconductor quantum well microcavities*, Superlattices and Microstructures, 43 (2008), pp. 417–426.

[153] J. Scheuder and M. Orenstein, *Optical vortices in crystals: Spontaneous generation in nonlinear semiconductor microcavities*, Science, 285 (1999), p. 230.

[154] P. Schwendimann and A. Quattropani, *Stationary and time dependent correlations in polariton condensates*, arxiv 1002.2874, (2010).

[155] A. Scott, ed., *Encyclopedia of Nonlinear Science*, Routledge, Taylor & Francis Group, New York, 2005.

[156] I. Shelykh, A.V.Kavokin, and G.Malpuech, *Spin dynamics of exciton polaritons in microcavities*, Physica Status Solidi B-Basic Solid State Physics, 242 (2005), p. 2271.

[157] I. Shelykh, G. Malpuech, K. V. Kavokin, A. V. Kavokin, and P. Bigenwald, *Spin dynamics of interacting exciton polaritons in microcavities*, Physical Review B, 70 (2004), p. 115301.

[158] I. A. Shelykh, A. V. Kavokin, Y. G. Rubo, T. C. H. Liew, and G. Malpuech, *Polariton polarization-sensitive phenomena in planar semiconductor microcavities*, Semiconductor Science And Technology, 25 (2010), p. 013001.

[159] I. A. Shelykh, Y. G. Rubo, G. Malpuech, D. D. Solnyshkov, and A. Kavokin, *Polarization and propagation of polariton condensates polarization and propagation of polariton condensates*, Physical Review Letters, 97 (2006), p. 066402.

[160] I. A. Shelykh, D. D. Solnyshkov, G. Pavlovic, and G. Malpuech, *Josephson effects in condensates of excitons and exciton polaritons*, Physical Review B, 78 (2008), p. 041302(R).

[161] M. Sich, D. N. Krizhanovskii, M. S. Skolnick, A. V. Gorbach, R. Hartley, D. V. Skryabin, E. A. Cerda-Mendez, K. Biermann, R. Hey, and P. V. Santos, *Observation of bright polariton solitons in a semiconductor microcavity*, Nature Photonics, 6 (2012), pp. 50–55.

[162] N. B. Simpson, L. Allen, and M. J. Padgett, *Optical tweezers and optical spanners with laguerre-gaussian modes*, Journal of Modern Optics, 43 (1996), p. 2485.

[163] J. Sinova, D. Culcer, Q. Niu, N. A. Sinitsyn, T. Jungwirth, and A. H. MacDonald, *Universal intrinsic spin hall effect*, Physical Review Letters, 92 (2004), p. 126603.

[164] M. S. Skolnick, T. A. Fisher, and D. M. Whittaker, *Strong coupling phenomena in quantum microcavity structures*, Semiconductor Science And Technology, 13 (1998), pp. 645–669.

[165] D. V. Skryabin, A. R. Champneys, and W. J. Firth, *Frequency selection by soliton excitation in nondegenerate intracavity down-conversion*, Physical Review Letters, 84 (2000), pp. 463–466.

[166] D. V. Skryabin, O. Egorov, F. Lederer, and A. Gorbach, *One dimensional polariton solitons and soliton waveguiding in microcavities*, in Proceedings of PLMCN9, 2009.

[167] D. V. Skryabin and W. J. Firth, *Dynamics of self-trapped beams with phase dislocation in saturateable kerr and quadratic nonlinear media*, Physical Review E, 58 (1998), pp. 3916–3930.

[168] D. V. Skryabin, Vladimirov, and A. G., *Vortex induced rotation of clusters of localized states in the complex ginzburg-landau equation*, Physical Review Letters, 89 (2002), p. 044101.

[169] D. Snoke and P. Littlewood, *Polariton condensates*, Physics Today, 63(8) (2010), p. 42.

[170] M. T. Solano and Y. G. Rubo, *Vortices in exciton-polariton condensates with polarization splitting*, arxiv 0910.2727, (2009).

[171] H. R. Soleimani, S. Cronenberger, O. Cregut, J. P. Likforman, M. Gallart, T. Ostatnicky, P. Gilliot, and B. Honerlage, *Study of exciton-polariton spin dynamics*, Applied Physics Letters, 85 (2004), p. 5263.

[172] D. D. Solnyshkov, H. Flayac, and G. Malpuech, *Black holes and wormholes in spinor polariton condensates*, Phsical Review B, 84 (2011), p. 233405.

[173] D. D. Solnyshkov, I. A. Shelykh, M. M. Glazov, G. Malpuech, T. Amand, P. Renucci, X. Marie, and A. V. Kavokin, *Nonlinear effects in spin relaxation of cavity polaritons*, Semiconductors, 41 (2007), p. 1080.

[174] K. Staliunas and V. J. Sanchez-Morcillo, *Transverse Patterns in Nonlinear Optical Resonators*, Springer, 2002.

[175] R. Stanley, R. Houdre, U. Oesterle, M. Gailhanou, and M. Ilegems, *Ultrahigh finesse microcavity with distributed bragg reflectors*, Applied Physics Letters, 65 (1994), pp. 1883–1885.

[176] R. P. Stanley, R. Houdre, C. Weisbuch, U. Oesterle, and M. Ilegems, *Cavity-polariton photoluminescence in semiconductor microcavities: Experimental evidence*, Physical Review B, 53 (1996), pp. 10995–11007.

[177] K. Stasiewicz, P. K. Shukla, G. Gustafsson, S. Buchert, B. Lavraud, B. Thide, and Z. Klos, *Slow magnetosonic solitons detected by the cluster spacecraft*, Physical Review Letters, 90 (2003), p. 085002.

[178] K. E. Strecker, G. B. Partridge, A. G. Truscott, and R. G. Hulet, *Formation and propagation of matter-wave soliton trains*, Nature, 417 (2002), p. 150.

[179] Suryadi, *Static electric field-induced modification of coherent nonlinear response of exciton-polariton in the semiconductor microcavities*, in Proc. Telecommunication Technologies 2008 and 2008 2nd Malaysia Conference on Photonics. NCTT-MCP 2008. 6th National Conference on, 2008, pp. 91–93.

[180] M. H. Szymanska, F. M. Marchetti, and D. Sanvitto, *Propagating wave-packets and quantised currents in coherently driven polariton superfluids*, arXiv:1005.4625v1, (2010).

[181] T. Tanaka, Z. Zhang, M. Nishioka, and Y. Arakawa, *Magnetic field dependence of exciton oscillator strength by measurements of magnetoexciton?polariton mode splitting in quantum wells with a microcavity*, Applied Physics Letters, 69 (1996), p. 887.

[182] A. I. Tartakovskii, M. Emam-Ismail, R. M. Stevenson, M. S. Skolnick, V. N. Astratov, D. M. Whittaker, J. J. Baumberg, and J. S. Roberts, *Relaxation bottleneck and its suppression in semiconductor microcavities*, Physical Review B, 62(4) (2000), p. R2283.

[183] F. Tassone, F. Bassani, and L. C. Andreani, *Quantum-well reflectivity and exciton-polariton dispersion*, Physical Review B, 45 (1992), p. 6023.

[184] F. Tassone, C. Piermarocchi, V. Savona, A. Quattropani, and P. Schwendimann, *Bottleneck effects in the relaxation and photoluminescence of microcavity polaritons*, Physical Review B, 56 (1997), pp. 7554–7563.

[185] B. Terhalle, T. Richter, A. S. Desyatnikov, D. N. Neshev, W. Krolikowski, F. Kaiser, C. Denz, and Y. S. Kivshar, *Observation of multivortex solitons in photonic lattices*, Physical Review Letters, 101 (2008), p. 013903.

[186] J. Tignon, P. Voisih, C. Delalande, M. Voos, R. Houdre, U. Oesterle, and R. P. Stanley, *From fermi's golden rule to the vacuum rabi splitting: Magnetopolaritons in a semiconductor optical microcavity*, Physical Review Letters, 74 (1995), p. 3967.

[187] M. Tlidi, P. Mandel, and R. Lefever, *Localized structures and localized patterns in optical bistability*, Physical Review Letters, 73 (1994), p. 640.

[188] G. Tosi, F. M. Marchetti, D. Sanvitto, C. Anton, M. H. Szymanska, A. Berceanu, C. Tejedor, L. Marrucci, A. Lemaitre, J. Bloch, and L. Vina, *Onset and dynamics of vortex-antivortex pairs in polariton optical parametric oscillator superfluids*, Physical Review Letters, 107 (2011), p. 036401.

[189] A. G. Truscott, M. E. J. Friese, N. R. Heckenberg, and H. Rubenstein-Dunlop, *Optically written waveguide in an atomic vapour*, Physical Review Letters, 82 (1999), p. 1438.

[190] K. J. Vahala, *Optical microcavities*, Nature, (2003), p. 839.

[191] L. K. van Vugt, B. Piccione, C.-H. Cho, P. Nukala, and R. Agarwal, *One-dimensional polaritons with size-tunable and enhanced coupling strengths in semiconductor nanowires*, Proceedings of the National Academy of Sciences of the United States of America, 108 (2011), p. 10050.

[192] P. Walker, T. C. H. Liew, D. Sarkar, M. Durska, A. P. D. Love, M. S. Skolnick, J. S. Roberts, I. A. Shelykh, A. V. Kavokin, and D. N. Krizhanovskii, *Suppression of zeeman splitting of the energy levels of exciton-polariton condensates in semiconductor microcavities in an external magnetic field*, Physicla Review Letters, 106 (2011), p. 257401.

[193] A. Wallraff, D. I. Schuster, A. Blais, L. Frunzio, R. S. Huang, J. Majer, S. Kumar, S. M. Girvin, and R. J. Schoelkopf, *Strong coupling of a single photon to a superconducting qubit using circuit quantum electrodynamics*, Nature, 431 (2004), pp. 162–167.

[194] C. Weisbuch, M. Nishioka, A. Ishikawa, and Y. Arakawa, *Observation of the coupled exciton-photon mode splitting in a semiconductor quantum microcavity*, Physical Review Letters, 69 (1992), pp. 3314–3317.

[195] C. O. Weiss, *Spatio-temporal structures. part ii. vortices and defects in lasers*, Physics Reports, 219 (1992), p. 311.

[196] C. O. Weiss, H. R. Telle, and K. Staliunas, *Restless optical vortex*, Physical Review A, 47 (1992), p. R1616.

[197] E. Wertz, L. Ferrier, D. D. Solnyshkov, R. Johne, D. Sanvitto, A. Lemaitre, I. Sagnes, R. Grousson, A. V. Kavokin, P. Senellart, G. Malpuech, and J. Bloch, *Spontaneous formation and optical manipulation of extended polariton condensates*, Nature physics Letters, (2010).

[198] D. M. Whittaker, *What determines inhomogeneous linewidths in semiconductor microcavities?*, Physical Review Letters, 80 (1988), p. 4791.

[199] ——, *Resonant rayleigh scattering from a disordered microcavity*, Physical Review B, 61 (2000), p. R2433.

[200] D. M. Whittaker and P. R. Eastham, *Coherence properties of the microcavity polariton condensate*, arXiv:0811.4333v1, (2008).

[201] D. M. Whittaker, P. Kinsler, T. A. Fisher, M. S. Skolnick, A. Armitage, A. M. Afshar, M. D. Sturge, and J. S. Roberts, *Motional narrowing in semiconductor microcavities*, Physical Review Letters, 77 (1996), p. 4792.

[202] J. E. Williams and M. J. Holland, *Preparing topological states of a bose-einstein condensate*, Nature, 401 (1999), p. 568.

[203] M. Wouters and I. Carusotto, *Goldstone mode of optical parametric oscillators in planar semiconductor microcavities in the strong-coupling regime*, Physical Review A, 76 (2007), p. 043807.

[204] A. I. Yakimenko, Y. A. Zaliznyak, and V. M. Lashkin, *Two-dimensional nonlinear vector states in bose-einstein condensates*, arXiv:0901.1041v1, (2009).

[205] A. V. Yulin, O. A. Egorov, F. Lederer, and D. V. Skryabin, *Dark polariton solitons in semiconductor microcavities*, Physical Review A, 78 (2008), p. 061801.

[206] R. Zimmermann, E. Runge, and V. Savona, *Quantum coherence, correlation, and decoherence in semiconductor nanostructures*, Academic Press, Boston, 2003.

[207] H. Zoubi and G. C. L. Rocca, *Microscopic theory of nonlinear polariton interactions in strongly coupled hybrid organic-inorganic microcavities*, Physical Review B, 76 (2007), p. 035325.